Colloidal Quantum Dots and Integration with Silicon for Near-Infrared Light Detection

by

Qiwei Xu

A thesis submitted in partial fulfillment of the requirements for the degree of

Doctor of Philosophy

in

Microsystems and Nanodevices

Department of Electrical and Computer Engineering

University of Alberta

Abstract

Near-infrared (NIR) light detection underpins various applications such as night vision, healthcare imaging and optical communications. While commercial silicon-based photodetector is transparent to wavelengths that are longer than about 1100 nm due to the absorption cut-off of silicon (Si), lead sulphide (PbS) colloidal quantum dots (CQDs) have received attention as the materials for NIR photodetection given their strong and tunable absorption in NIR region and room-temperature solution processability. This thesis presents our progress in realizing fast and efficient NIR photodetection based on PbS CQD. The particular focus considers the integration of PbS CQDs with Si for on-Si light detection.

The CQDs exhibit low carrier mobility ($\sim 10^{-5}$-10^{-2} $cm^2V^{-1}s^{-1}$) compared to their crystalline counterparts, which has severely hindered the realization of high-speed PbS CQD photodetection. We demonstrate a fast PbS CQD photodiode fabricated from low-mobility CQDs ($\sim 10^{-3}$ $cm^2V^{-1}s^{-1}$) with rise/fall times as short as 0.33 μs at zero voltage bias. The device achieves a fast response by engineering RC time delay and charge transport.

Integrating PbS CQDs onto Si opens a plethora of applications in NIR light sensing for the CQDs. An integration strategy is proposed based upon an on-chip CQD photodetector structure, photodiode-oxide-semiconductor field-effect transistor (POSFET). This device architecture utilizes Si as a channel for carrier transport and PbS CQD as the light-absorbing material controlling the channel conductivity. Simulations showed that the photodiode could provide photovoltage to the semiconductor, forming an inversion layer at the oxide-semiconductor interface, and the electron density at the interface is significantly enhanced. For a proof-of-concept

demonstration, we experimentally connected a CQD photodiode with a commercial Si transistor and proved that the current from the transistor could be increased by photovoltage provided by the photodiode under NIR light illumination. The device shows a responsivity of 5.9A/W at the wavelength of 1250 nm.

Another on-Si integration strategy based upon a structure of PbS CQD/Si heterojunction has recently received attention. We conducted a simulation work, in which we leverage and incorporate the heterojunction structure in a Si photonics platform. The study comprehensively compares the CQDs with the other two candidates for NIR light detection, germanium (Ge) and indium gallium arsenide (InGaAs), for a photodetector integrated with a Si waveguide. Results find that the CQD photodetector is slow but has the lowest dark current, which is suitable for medium-speed but ultralow noise applications.

CQD/Si heterojunction photodetectors that have been previously reported suffer from low EQE at the NIR region. We demonstrate that Si surface passivation is crucial for building a high-performance CQD/Si heterojunction photodetector. We have studied one-step methyl iodine (CH_3I) and two-step chlorination/methylation processes for Si surface passivation. Transient photocurrent (TPC) and transient photovoltage (TPV) decay measurements reveal the two-step passivated CQD/Si interface exhibits fewer trap states and decreased recombination rates. These passivated substrates were incorporated into prototype CQD/Si infrared photodiodes, and the best performance photodiode based upon the two-step passivation shows an EQE of 31% at 1280 nm which represents a nearly two-fold increase over the standard device based upon the one-step CH_3I passivated Si.

Further, we demonstrate the successful integration of PbS CQD Inks with Si. Thanks to the well-passivated Si surface by the two-step method and high-quality CQD Inks, the heterojunction

photodiode yields a low density of trap states. With an insertion layer of *p*-type CQDs capped with1,2-ethanedithiol (EDT) ligands, the built-in electric field is much enhanced, leading to improved charge extractions. As a result, we obtained an EQE of 44% at the excitonic wavelength of 1280 nm. The EQE values are maintained without detectable degradation throughout more than 600 h, achieving superior device stability.

The aforementioned studies reveal the potential of large-area and room-temperature integration of PbS CQDs on Si read-out integrated circuits (Si-ROCIs) for building a NIR CMOS image sensor (CIS). Finally, we conduct a simulation study, in which we incorporate CQD/Si heterojunction into a NIR CMOS CIS. Results clearly show that each pixel on the CIS sensitively responds to NIR light, and signals are read out through the bottom circuits as validated by the readout timing sequence simulation.

The findings in this thesis are invaluable to the research of developing low-cost and large areas, especially on-Si NIR light detection.

Preface

This thesis is an original work by Qiwei Xu under the supervision of Dr. Xihua Wang in the Department of Electrical and Computer Engineering at the University of Alberta.

Chapter 2 of this thesis has been published as:

Q. Xu, L. Meng, K. Sinha, F. I. Chowdhury, J. Hu and X. Wang, “Ultrafast colloidal quantum dot infrared photodiode”, *ACS Photonics* 7(5), 1297-1303 (2020).

I was responsible for the design of the study, device fabrication, performing simulation, data analysis and manuscript drafting. X. Wang was the supervisory author and was involved in the design of the study and manuscript editing. All authors were involved in discussions and manuscript editing.

Chapter 3 of this thesis has been published as:

Q. Xu, L. Meng, T. Zeng, K. Sinha, C. Dick, and X. Wang, “On-chip colloidal quantum dot devices with a CMOS compatible architecture for near-infrared light sensing”, *Optics Letters*, 44, 463-466 (2019).

I was responsible for the design of the study, device fabrication, performing simulation, data analysis and manuscript drafting. X. Wang was the supervisory author and was involved in the design of the study and manuscript editing. All authors were involved in discussions and manuscript editing.

Chapter 4 of this thesis has been published as:

Q. Xu, J. Hu and X. Wang, “On-chip Ge, InGaAs and CQD photodetectors: comparisons for application in silicon photonics”, *Journal of the Optical Society of America B*, 38, 194-200 (2021).

I was responsible for the design of the study, performing simulation, data analysis and manuscript drafting. X. Wang was the supervisory author and was involved in the design of the study and manuscript editing. All authors are involved in discussions and manuscript editing.

Chapter 5 of this thesis has been published as:

1. Q. Xu, I.T. Cheong, L. Meng, J.G. Veinot and X. Wang. “Silicon Surface Passivation for Silicon-Colloidal Quantum Dot Heterojunction Photodetectors”, *ACS Nano*, *15*(11), 18429-18436 (2021).

This was a collaborative work with Professor J.G. Veinot in the Department of Chemistry, with Professor X. Wang being the lead collaborator in the Department of Electrical and Computer Engineering. I. T. Cheong and Professor J. G. Veinot provided technical support on the experimental apparatus. I was responsible for the design of the study, device fabrication and characterization, data analysis and manuscript drafting. X. Wang was the supervisory author and was involved in the design of the study and manuscript editing. All authors were involved in discussions and manuscript editing.

Chapter 6 of this thesis has been published as:

1. Q. Xu, I. T. Cheong, H. Song, V. Van, J. G. Veinot, & X. Wang. “Heterogeneous Integration of Colloidal Quantum Dot Inks on Silicon Enables Highly Efficient and Stable Infrared Photodetectors”, *ACS Photonics*, *9*(8), 2792-2801 (2022).

This work was a collaboration between Professor V. Van in the Department of Electrical and Computer Engineering and Pro Professor J.G. Veinot in the Department of Chemistry, with Professor X. Wang being the lead collaborator in the Department of Electrical and Computer Engineering. I. T. Cheong, H. Song, Professor V. Van and Professor J. G. Veinot provided technical support on the experimental apparatus. I was responsible for the design of the study, performing simulation, device fabrication and characterization, data analysis and manuscript drafting. X. Wang was the supervisory author and was involved in the design of the study and manuscript editing. All authors were involved in discussions and manuscript editing.

Acknowledgement

I would like to thank my supervisor, Professor Xihua Wang, for all he has done for me for the past six years of my doctorate life. Without a doubt, I cannot achieve what I have without his guidance. I was careless and even somewhat reckless during the early years of my doctorate. Yet, he has always been so patient, kind and also professional to me. Since then, I have gradually learned to build plans, take notes, settle down and keep calm. To me, Professor Wang is not just an academic supervisor but more of a life mentor. Thank you for shaping me into the person I am now.

I would also like to thank Professor Vien Van and Professor Masum Hossain. I had so many valuable discussions with them which had huge contributions to my research. They have always been so generous to me, providing facilities, tools and resources that I needed for my research.

I am grateful to my colleagues, Dr. Lingju Meng, Dr. Seyed Milad Mahperkar, Dr. Farsad Imtiaz Chowdhury, and Kaustubh Sinha. I enjoyed it and I am still missing the old times we spent together. I felt sad watching each of you leave the lab and move on, but I am also happy about what you have achieved. Keep in touch friends.

Special thanks to all the staff in NanoFAB at the University of Alberta, Dr. Arron Hryciw, Dr. Nancy Zhang, Dr. Shihong Xu, Melissa Hawrelechko, Timothy Harrison and Glenn Elaschuk. They have provided valuable advice and help with my experiments. NanoFAB also provided me with state-of-the-art research facilities and tools.

I feel so blessed and grateful that I met I Teng Cheong. She is so caring and kind-hearted towards everyone. She tolerated my temper and taught me what is patience and responsibility. She is super supportive and encourages me whenever I need it. Through her, I also met friends with some of

the most interesting souls in this world, Terence, Natasha, Hyerin, Jierui, and Ifte. Thank you all for making my life more interesting.

I am exceptionally grateful for the support and never-ending love from my family, my mom, my dad, and my twin brother. Without their encouragement, I would never pursue a doctorate in my life. Studying abroad is not easy but all the support I received from them made it happen. The separation for all these years never fades away my feeling towards my family but only deepened my love for them. Finally, I would like to give my sincere love to my grandma, who passed away when I am writing this thesis. She was a kind and cute person who enjoyed tasting KFC burgers and bubble teas. Her memory deteriorated but she can always remember my nickname, Nini. May you rest in peace in heaven.

Table of Contents

List of Tables

List of Figures

List of Abbreviations

Ag	Silver
Al	Aluminum
CCD	Charge-coupled device
CMOS	Complementary-metal-oxide semiconductor
CQD	Colloidal quantum dots
CT	Computed tomography
D_λ^*	Specific detectivity
EQE	External quantum efficiency
ETL	Electron transport layer
Gain	G
Ge	Germanium
HTL	Hole transport layer
InGaAs	Indium Gallium Arsenide
IR	Infrared
ITO	Indium Tin Oxide
MRI	Magnetic resonance imaging
NEP_λ	Noise-equivalent power
NiO	Nickel oxide
NIR	Near-infrared
P3HT	Poly(3-hexylthiophene)
PCBM	[6,6]-phenyl C71 butyric acid methyl ester

PDTP-DFBT	poly[2,7-(5,5-bis-(3,7-dimethyloctyl)-5H-dithieno[3,2-b:2′,3′-d]pyran)-alt-4,7-(5,6-difluoro-2,1,3-benzothia diazole)]
POSFET	Photodiode-oxide-semiconductor field-effect transistor
Responsivity	R_λ
Si	Silicon
Si-ROIC	Si read-out integrated circuit
TiO_2	Titanium oxide
TMD	Transition metal dichalcogenides
TPC	Transient photocurrent
TPV	Transient photovoltage
UV	Ultraviolet
ZnO	Zinc oxide

1. Introduction

1.1 Photodetectors and Applications

Photodetectors are sensors made for light or photon detections, which mainly utilize photon-excited electric charges and generate electric currents. Their light detection mechanism is based on the internal photoelectric effect (or simply the photoelectric effect). To be more specific, when light hits semiconductor surfaces with sufficiently high photon energy that is larger than the material's bandgap, an electron gains enough energy to break its bond to the parent atom and is excited from the valence band to higher levels at conduction band, where it is free to move. This results in an increase in free carrier density and thus conductivity in the semiconductor material. In a photodetector, the excess carriers directionally transport under an internal or externally applied electric field, leading to photocurrent generation in the device. Photodetectors based upon other working mechanisms, such as photochemical and thermal effects are not considered in this thesis. Nowadays, photodetectors are among the most ubiquitous technology used in our daily lives, ranging from optical detectors in television remote controls to detectors in automatic doors in public spaces. Photodetector applications cover almost all of the electromagnetic spectrum, with some important applications listed in the following (Figure 1). Note that, the definition of NIR wavelength range varies. For example, some categorize NIR from 780 nm to 1400 nm and shortwave infrared (SWIR), instead, from 1400 nm to 3000 nm; others generally refer to this entire range as NIR or SWIR. For simplicity, we refer to the entire range as NIR.

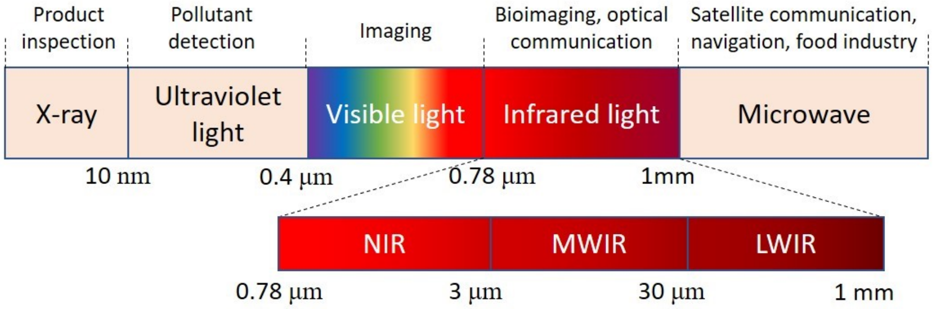

Figure 1.1. Electromagnetic spectrum. NIR, MWIR and LWIR stand for, near-infrared, mid-wavelength infrared and long-wavelength infrared.

Photodetectors are cornerstone components for process monitoring in food and manufacturing industries. For example, X-ray photodetectors are implemented in the food industry for the detection of contaminants to ensure food safety, such as glass, stone, stainless steel, plastic, etc. In manufacturing industries, photodetectors are commonly used as position sensors to ensure the proper place of a product.

In the ultraviolet (UV) range, applications such as flame detection and ozone monitoring heavily rely on accurate UV photodetection. UV detection also is widely implemented for optical communications in outer space for intra- and inter-satellite secured communications.

The largest volume application for photodetectors might come from imaging video cameras in the visible regime, which ranges from small-size cameras such as dash cams for cars, cellphone cameras and palm-sized action cameras to large cameras used by TV broadcasting. CCD (known as charge-coupled device) technology has dominated video cameras for decades since its invention in the late 1960s, mainly due to its high sensitivity and large dynamic range. Powered by the advances in photolithography technology and the booming of mobile phones, CMOS (complementary-metal-oxide semiconductor) technology has taken over CCD as the more popular one. The latter merits its lower power consumption and smaller footprint. CMOS technology also delivers much faster speed and easier camera-on-chip integration.

Another special interest lies in infrared (IR). Night vision detection is crucial for security surveillance and military purposes, which require high-performance IR image sensors. As fibre-optic communications operate in near-IR (NIR) regions, fast NIR light detection is needed to transfer fast optical signals to electrical signals. NIR imaging has also emerged to be a promising tool for medical applications. NIR fluorescence imaging system serves as one typical example. The system is capable of human tissue imaging and thus enables cancer detection and many other important clinical applications, including real-time metabolic monitoring, non-invasive imaging of the lymphatic system and microvasculature blood flow mapping. Compared with conventional imaging techniques such as computed tomography (CT) and magnetic resonance imaging (MRI), the technology generally features a real-time display, high spatial and temporal resolution, high portability of the system, etc.

In collision avoidance systems for automotive, photodetectors also play an indispensable role. The system which can prevent or reduce collision severity is usually sophisticated, involving multiple sensors, e.g., photodetectors for radar or Lidar and image sensors. On the other hand, Lidar systems have been widely utilized for 3D-object representations, useful for facial recognition in mobile devices and automated driving systems in autonomous vehicles; therefore, photodetectors can also find applications there.

1.2 Figure of Merits for Photodetectors

Commonly exploited structures of photodetectors can be categorized into main four types: photodiode, including p-n and p-i-n junction photodiode and avalanche photodiode, in which generated carriers are collected by electrodes through diffusion and/or drift under intrinsic or externally applied electric field; photoconductor, in which semiconductor materials reduce their electrical resistance as a result of non-equilibrium generation of electric carriers upon absorption of the incident photons; phototransistor, which employs internal photocurrent amplification and thus possesses larger gain than photodiode; and metal-semiconductor-metal photodetector, which exploits two Schottky junctions to collect generated electric charges, instead of one as in the case of Schottky photodiode.

A few of the most important figures of merits used for characterizing photodetector performance are discussed in the following. A basic metric that quantifies the photodetector efficiency is responsivity, which takes the form of

$$R_{\lambda}=\frac{I_{\mathrm{p}}(\lambda)}{P(\lambda)} \tag{1.1}$$

where R_{λ} is the responsivity in A/W, I_{p} is the generated photocurrent (in the unit of A) and P is the illuminated light power (in the unit of W). In some references, photovoltage (V_{p} in the unit of V) instead of photocurrent is employed. Thus, wavelength-dependent responsivity value relates the generated photocurrent (or photovoltage) to a given illuminated light power. A similar quantity that relates output with input is EQE, which is the ratio between output electron numbers and input photon numbers. EQE can be related to responsivity as follow,

$$\mathrm{EQE}(\lambda)=R_{\lambda}\frac{h\mathrm{c}}{q\lambda}\approx R_{\lambda}\frac{1240}{\lambda} \tag{1.2}$$

where $h = 6.63\times10^{34}$ J-s, is Planck constant, $c = 3\times10^{8}$ m/s, is the speed of light, $q = 1.6\times10^{19}$ C, is the electron charge and λ is the wavelength in nm. In some cases, gain (G) is introduced instead of EQE when the number of extracted electrons per input photon exceeds unity.

Photodetector sensitivity is another significant aspect, which can be determined by the noise-equivalent power (NEP_{λ}), defined as

$$\mathrm{NEP}_{\lambda} = \frac{i_{\mathrm{n}}}{R_{\lambda}} \tag{1.3}$$

where i_{n} is noise current and R_{λ} is spectral responsivity. NEP_{λ} determines the minimum incident light power that a photodetector can measure at a certain wavelength. Noise sources including thermal, shot, and flicker noises can all contribute to noise current. Thermal noise for a photodetector originates from resistance (both series and shunt resistance), but more dominantly from the amplifier that is connected to the photodetector. Shot noise is a quantum noise effect as a result of the discrete nature of photodetection and the resulting randomness in the optical field leads to the fluctuations or shot noise in the photocurrent. Unlike the shot noise, flicker noise is spectral dependent and proportional to $1/f$, more predominant low-frequency regimes.

To cross-compare sensitivity for photodetectors with different areas, specific detectivity is proposed and defined as

$$D_{\lambda}^{*} = \frac{\sqrt{\mathrm{A_D}}}{\mathrm{NEP}} \tag{1.4}$$

where D_{λ}^{*} is the specific detectivity in the unit of jones and $\mathrm{A_D}$ is the device area.

The temporal response is used to determine the speed of a photodetector. It is normally determined by rise/fall ($t_{\mathrm{rise}}/t_{\mathrm{fall}}$) time and 3dB bandwidth or cut-off frequency ($f_{3\mathrm{dB}}$). Rise time t_{rise} (fall time t_{fall}) is defined as the time for a signal generated by a photodetector under a square-wave light illumination to rise (fall) from 10% (90%) to 90% (10%) of its final value. Cut-off frequency $f_{3\mathrm{dB}}$ is defined as the frequency at which the output signal drops by half or 3dB.

1.3 NIR Light Detection

In recent years, the photodetectors designed for the NIR region (780 - 3000 nm) have raised tremendous attention, due to their immense potential for applications in optical telecommunication, facial and gesture recognition, terrestrial mapping, night vision and security surveillance. For applications requiring longer wavelengths in the NIR region (> 1100 nm), the most widely utilized material in modern semiconductor electronics - Si - is no longer suitable. This is attributed to the steep roll-off in its light absorption in the longer NIR range. For instance, Si has an absorption coefficient of ~ 61.6 cm^{-1} at 1000 nm, and a Si layer with a thickness of 100 μm absorbs 75% of the incoming light. However, for most Si-based CMOS imagers, the epitaxial Si layer normally has a thickness only from 5 to 10 μm. Increasing the Si epi layer requires a higher bias voltage or lower doping level, which adversely influences device operation.

To this end, previously developed commercial NIR photodetectors are normally based on high-temperature hetero-epitaxial growth of Germanium (Ge) and III-V materials [1]–[3]. For Ge photodetector, the Ge layer is normally epitaxially grown on Si. Its biggest challenge is the large lattice mismatch (4.2%) between Si and Ge, leading to large threading dislocations which ultimately increase dark current [4]. This can be much improved by a post-growth annealing process [5]. Another disadvantage is that crystalline Ge is an indirect-bandgap semiconductor, rendering much lower light absorption efficiency than III-V counterparts. Meanwhile, the Ge photodetector also exhibits large thermally induced noise, making it less sensitive. III-V compound devices, on the other hand, are generally costly. Taking InGaAs as an example, it is normally epitaxially grown on indium phosphide (InP). InGaAs photodetector merits much lower thermal noise compared to Ge photodetector, and thus much more sensitive. The disadvantage is that sophisticated techniques are employed to transfer the InGaAs layer onto Si-based microelectronic circuits, such as transfer printing [6], [7] and wafer/die bonding [8], [9]. Although direct epitaxy of InGaAs on Si is possible, the device needs a seeding layer (epitaxial buffer layer) with several micrometer thick [10], [11], compared to only tens of nm for mature Ge epitaxy technology [12]; and device efficiency is far from optimized. Nevertheless, photodetectors fabricated based on high-temperature hetero-epitaxy suffer from added manufacturing complexity and energy costs.

1.4 Colloidal quantum dots

In light of the challenge mentioned in the previous section, CQDs have gained tremendous attention in recent years. CQDs are nanoparticles with their sizes much smaller than the exciton Bohr radii of their bulk materials. This brings the physical confinement of electronics into a quantum dot which alters the energy levels of the CQDs and tunes the electronic bandgap. In particular, PbS CQD is a promising material for NIR light detection due to its strong and size-dependable light absorption which can be further extended into the mid-IR range [13], [14]. CQDs could be synthesized using the hot injection method in large quantities, and synthesizing temperature normally is much lower than the epitaxial temperature used for Ge and InGaAs fabrication; this promises low economical and thermal budgets. While electrical properties for crystalline semiconductors could be tuned through a doping process under elevated temperatures, the properties of CQDs could be altered by a much simpler room-temperature ligand exchange process in chemical solutions. Adding to the appeals, because of the solution processability, CQDs can be easily deposited *via* spin-coating, spraying and ink printing under room temperature [14]–[18]. This enables significantly reduced fabrication complexity and lowered processing costs for CQDs' integration with other platforms, especially Si-based microelectronic circuits.

1.5 NIR PbS CQD Photodetectors

NIR PbS photodetectors with unprecedented gain and sensitivity have been developed. Structures of previously proposed PbS CQD-based NIR photodetectors can be mainly categorized into photoconductor, photodiode, and photo field-effect transistor (photoFET) as shown in Figure 1.2.

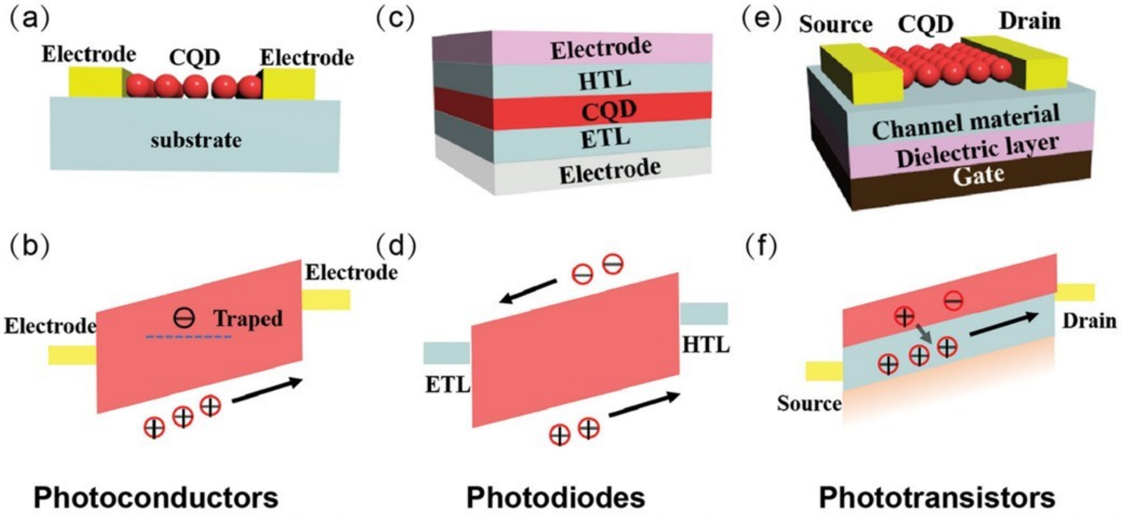

Figure 1.2. Architecture of previously proposed PbS CQD-based NIR photodetectors with energy band diagrams for (a),(b) photoconductor, (c),(d) photodiode, and (e),(f) phototransistor. Reproduced with permission [19]. Copyright 2020, Wiley-VCH GmbH.

1.5.1 Photoconductor

Photoconductor was one of the most common types being investigated in the early stages of research for PbS CQD photodetectors. In a basic configuration, a photoconductor consists of a planar channel made with photo-sensitive material (PbS CQDs) and two electrodes (source S and drain D) at two ends (Figure 1.2a). As mentioned earlier, photo-induced carriers increase carrier density and thus the conductivity in the channel. Generated carriers will circulate in the channel before recombination under biased-voltage conditions, which produces photoconductive gain. In a PbS CQD photoconductor, the photoconductive gain is assisted by trap states (sensitizing centers) situated within the material bandgap. Photo-generated holes (electrons) are swept by the applied voltage V_{DS} and transverses the channel multiple times before recombination with electrons (holes) which are captured and localized by the trap states. This gain aided by trap states is also termed trap-assisted gain, which is determined by

$$G=\frac{\tau_{\text{lifetime}}}{\tau_{\text{transit}}}=\frac{\tau_{\text{lifetime}}\mu V_{\text{DS}}}{L^2} \tag{1.5}$$

where τ_{lifetime} is carrier lifetime, τ_{transit} is carrier transit time in the channel, μ is carrier mobility, L is channel length, and V_{DS} is bias voltage. PbS CQD photoconductors generally possess large gains due to the long carrier lifetime due to the sensitizing centers [20].

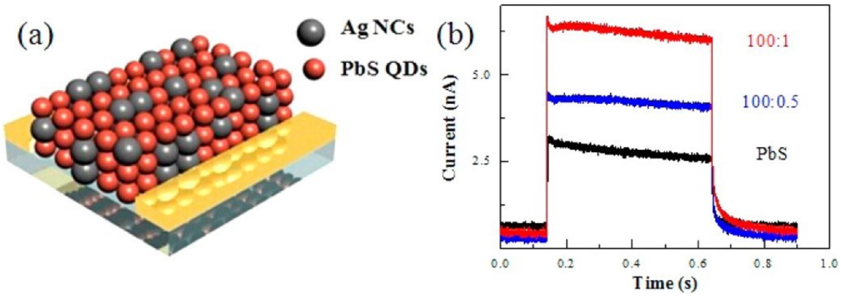

Figure 1.3. (a) Schematics of photoconductor based on PbS CQDs and Ag nanocrystal composites. (b) Photocurrent of devices with Ag nanocrystal incorporation. Reproduced with permission. Copy right 2014, American Chemical Society.

The carrier lifetime can be further prolonged by incorporating PbS CQD with other materials. In Figure 1.3, for example, silver (Ag) nanocrystals incorporated into PbS CQD photoconductor could capture photogenerated electrons from nearby CQDs, further increasing carrier lifetime, and thus gain and responsivity [21]. The long carrier lifetime, however, significantly slows the device speed, resulting in a 'long tail' in the photocurrent signal when the light is off (see Figure 1.3b). This is because trapped photocarriers will be slowly "released" when illumination is off, thus creating a long-tail current. Depending on the device geometry size, the 3dB bandwidth could be as low as only ~10 Hz. Thus, a trade-off exists between gain and temporal response in a photoconductor. The large dark current is another limiting factor. Nevertheless, the detectivity is still high thanks to the ultrahigh gain.

1.5.2 Photodiode

PbS CQD photodiode forms a built-in electric field and depletion region (space charge region), generated by p-n homo/heterojunction between two oppositely doped PbS CQDs or between the CQD and heavily doped electron/hole transport layer (ETL/HTL), or by Schottky junction between the semiconductor and metal electrodes. The photodiode normally works under reverse-bias conditions. Because of the existence of depletion region, it merits from ultralow dark current, leading to low noise and high detectivity. Under the light, photo-excited carriers undergo a charge-separation process and are collected by electrodes *via* drift (in the depletion region) and diffusion (in the neutral region). The gain mechanism in PbS CQD photodiode is thus based on charge separation and quantum efficiency is normally smaller than unity with some exceptions (gain > 1) which will be discussed later in this section. The time response of the device is determined by carrier transit time to reach the electrical contacts instead of carrier lifetime as in the case of PbS CQD photoconductor, rendering a much higher bandwidth.

In 2008, Clifford et al. demonstrated a Schottky photodiode (see Figure 1.4a) [22]. The Schottky junction is between *p*-type PbS CQD and aluminum (Al) contact. Two components determine the temporal response of a photodiode which are minority-carrier (electrons) drift and diffusion. The former is a fast process driven by the electric field, while the latter is a much slower process induced by carrier density gradient. By excluding the diffusion component in the device operation, the authors successfully built an ultrafast Schottky photodiode with a 3dB bandwidth close to 3 MHz (see Figure 1.4b), much higher than PbS CQD photoconductors. However, one typical drawback of the Schottky photodiode is its large dark current, causing high noise levels and limiting device detectivity.

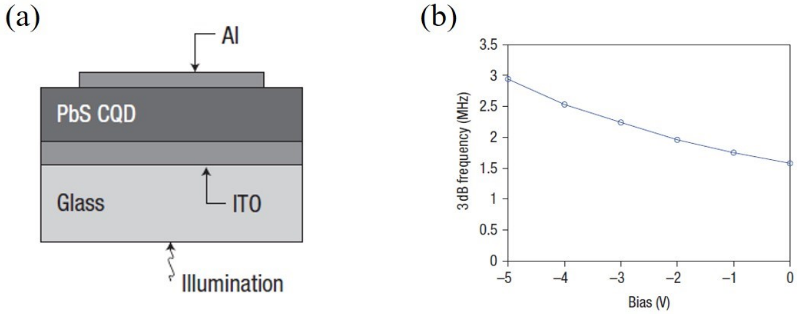

Figure 1.4. (a) Schematics of PbS CQD Schottky photodiode (b) Dependence of device speed on the bias voltage. Reproduced with permission [22]. Copy right 2008, Springer Nature.

In 2012, Klimov group presented a p-n photodiode using *p*-type PbS CQD and *n*-type ZnO/TiO_2 (zinc oxide/titanium oxide) as shown in Figure 1.5a [23]. In the device, the wide-gap oxide semiconductor serves as ETL that also blocks hole injection from the contact. The configuration of the device also features a wider depletion region compared to the case of the Schottky photodiode. Both ETL and wider depletion region effectively suppress dark current (70-80 nA/cm^2, see Figure 1.5b). Taking a step further, So group in 2014 added a NiO (nickel oxide) HTL in the structure (Figure 1.6a) [24]. This prevents electron injection from ITO (indium tin oxide) contact, further reducing dark current (20 nA/cm^2, see Figure 1.6b).

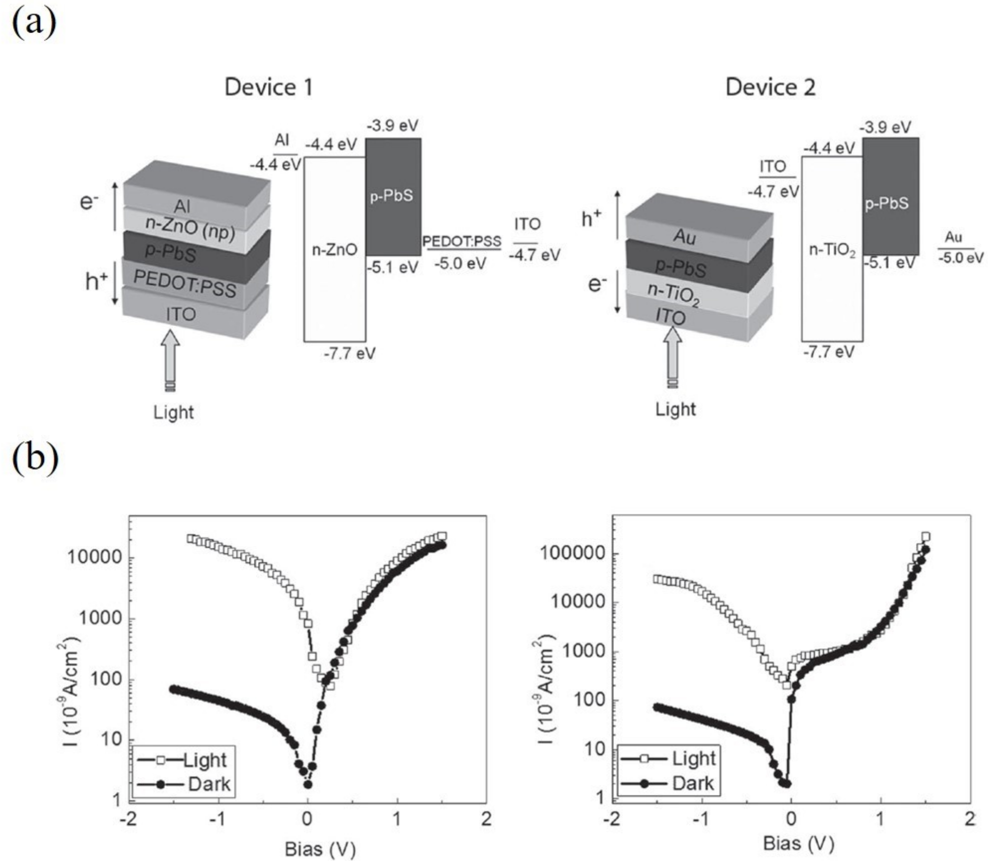

Figure 1.5. (a) Schematics of PbS CQD p-n photodiode with ETL. (b) Dependence of light and dark current characteristics on voltage bias. Reproduced with permission [23]. Copy right 2012, WILEY-VCH Verlag GmbH & Co. KGaA, Weinheim.

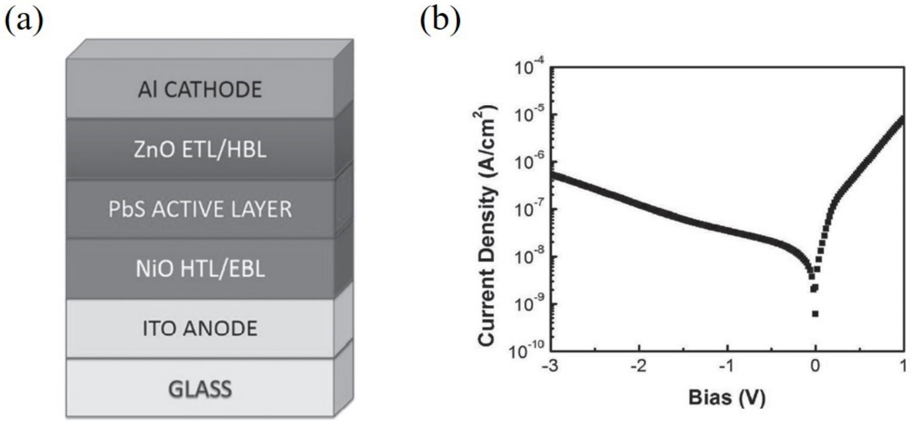

Figure 1.6. (a) Schematics of PbS CQD p-n photodiode with both ETL and HTL. (b) Dependence of dark current characteristics on voltage bias. Reproduced with permission [24]. Copy right 2014, WILEY-VCH Verlag GmbH & Co. KGaA, Weinheim.

However, one obvious deficiency of photodiodes compared to photoconductors is their low quantum efficiency, which normally cannot be larger than unity. Yet, PbS CQD photodiodes with gain have been demonstrated by introducing traps into the device and therefore switch the gain mechanism from charge separation to trap-assisted photoconductive gain as elaborated in the last section.

PbS CQD photodetectors implemented with inorganic-organic ternary blends in the early stage have attracted enormous attention, in which inorganic PbS CQD and two organic polymers are mixed [25]. The two polymers serve as electron and hole transporting matrixes, while PbS CQD act as sensitizing centers that induce trap-assisted photoconductive gain. For example, as illustrated in Figure 1.7a Shen et al. demonstrated a ternary blend made of PbS CQD:PDTP-DFBT:PCBM, where PDTP-DFBT stands for poly[2,7-(5,5-bis-(3,7-dimethyloctyl)-5H-dithieno[3,2-b:2′,3′-d]pyran)-alt-4,7-(5,6-difluoro-2,1,3-benzothia diazole)], PCBM stands for

[6,6]-phenyl C71 butyric acid methyl ester. A gain close to 2 was obtained, which is induced by PbS CQD's hole-trapping effect (see Figure 1.7b,c) [26]. To achieve higher photoconductive gain, Dong et al. introduced ZnO CQDs into the ternary blend (Figure 1.8a), PbS CQD: poly(3-hexylthiophene) (P3HT):PCBM:ZnO CQD, in which the extra ZnO CQD features a large density of electron traps, triggering hole injections from the metal contacts and thus photoconductive gain [27]. Finally, a gain exceeding 10 is achieved in the visible region (see Figure 1.8b,c). Instead of introducing traps in the photoactive layer, in 2015 So group introduced hole traps in the HTL, TAPC (1,1-bis[(di-4-tolylamino)phenyl]cyclohexane) as shown in Figure 1.9a. The traps are generated by Ag atom penetration into the TAPC layer during thermal evaporation of Ag contact. A gain that is higher than 180 is obtained [28].

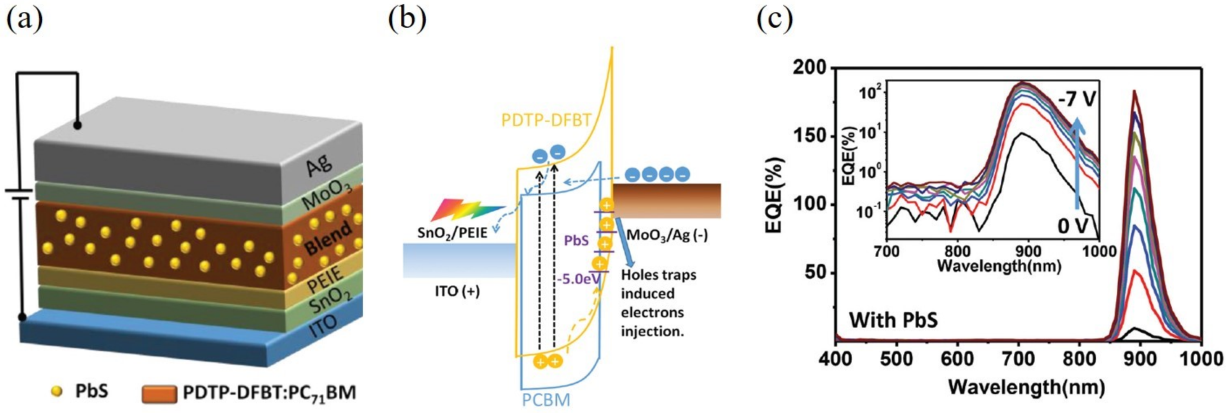

Figure 1.7. (a) Device structure of ternary bled photodiode. (b) Band structure of the device, generated holes are trapped in PbS CQDs, which induces trap-assisted photoconductive gain. (c) Dependence of EQE on different bias voltage. Reproduced with permission [26]. Copy right 2016, The Royal Society of Chemistry.

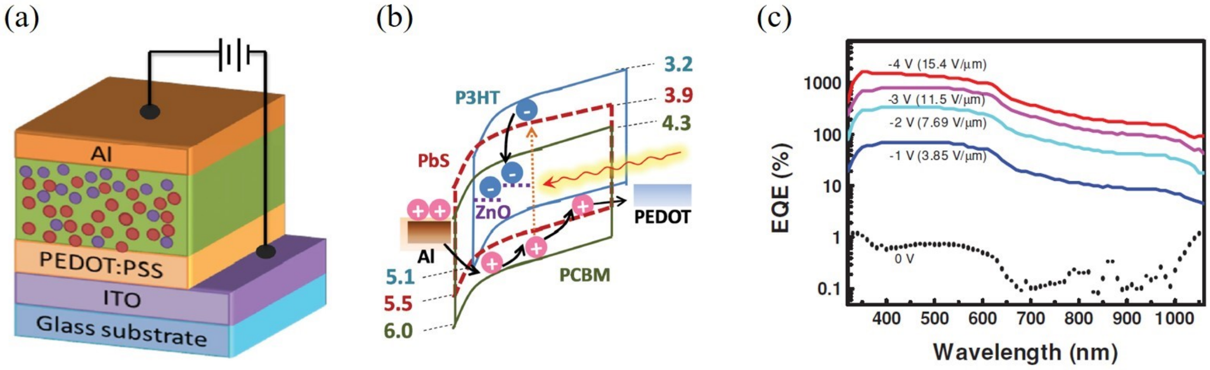

Figure 1.8. (a) Device structure of ternary bled photodiode doped with ZnO CQDs. (b) Band structure of the device, generated electrons are trapped in ZnO CQD which induces trap-assisted photoconductive gain. (c) Dependence of EQE on different bias voltage. Reproduced with permission [27]. Copy right 2014, WILEY-VCH Verlag GmbH & Co. KGaA, Weinheim.

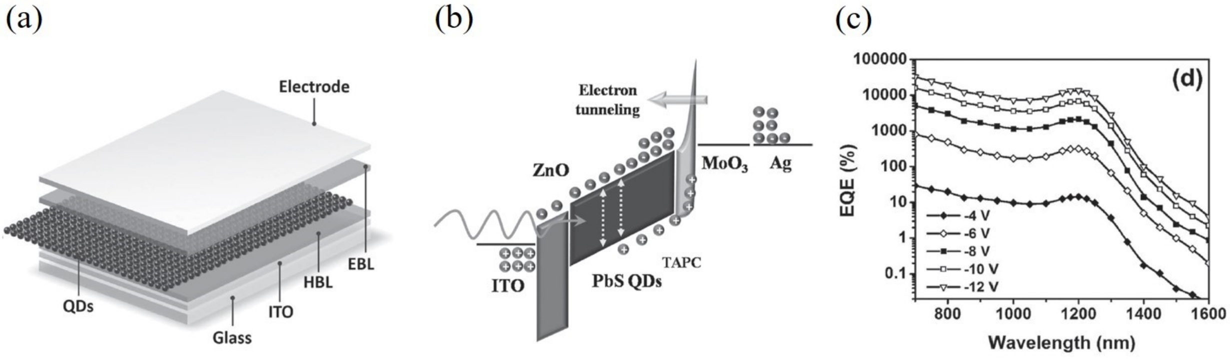

Figure 1.9. (a) Schematic view of PbS CQD photodiode with high gain. (b) Band structure of the device, the generated holes are trapped in TAPC which induces trap-assisted photoconductive gain. (c) Dependence of EQE on different bias voltage. Reproduced with permission [28]. Copy right 2015, WILEY-VCH Verlag GmbH & Co. KGaA, Weinheim.

1.5.3 PhotoFET

As discussed in the previous sections, PbS CQD photoconductors merit high gain but suffer from large dark currents, while photodiodes have a low gain but feature ultralow dark currents. PhotoFET (photo field-effect transistors or phototransistors) is a promising architecture that can simultaneously achieve low dark current and high gain. The configuration for a conventional PhotoFET is similar to a photoconductor but with an additional gate terminal. The gate voltage can effectively control channel conductivity and thus control dark current. From equation 1.5, one can observe that the trap-assisted gain is linearly proportional to the mobility of the channel material. Therefore, efforts have sought to integrate high-mobility materials in a PbS CQD photoFET, such as transition metal dichalcogenides (TMD) and graphene with PbS CQD as shown in Figure 1.2e. In this architecture, PbS CQD serves as sensitizing centers for NIR illumination, whereas the channel material features high mobility, leading to high gain. Apart from the gate terminal controlling the channel conductivity, the junction and depletion region formed between the channel material and PbS CQD can also suppress dark current.

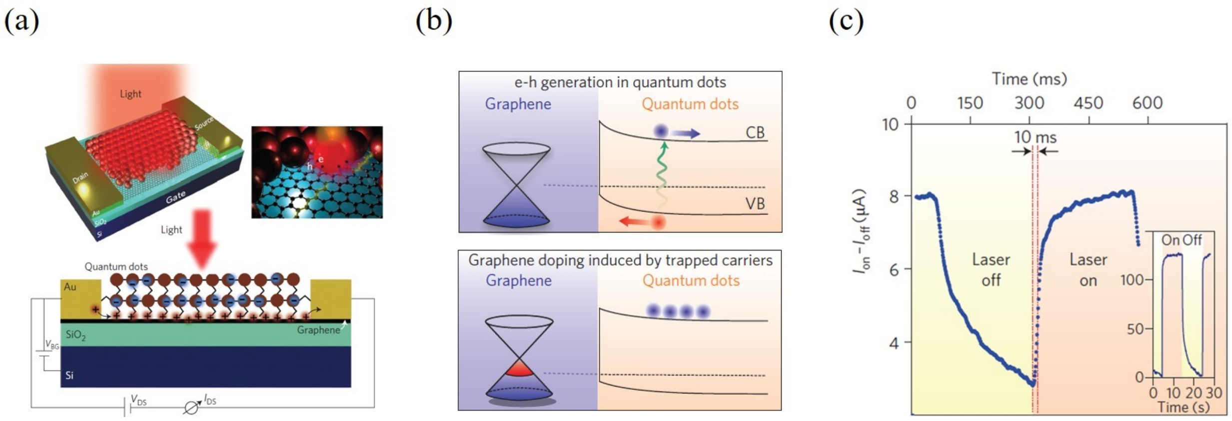

Figure 1.10. (a) Schematic view of hybrid PbS CQD/graphene photoFET with ultrahigh gain. (b) Band structure of the device, the generated electrons are trapped in CQD while holes inject into

graphene and circulate in the channel, which induces trap-assisted photoconductive gain. (c) temporal response of the device. Reproduced with permission [29]. Copy right 2012, Macmillan Publishers Limited.

In 2012, Konstantatos et al. first presented a hybrid PbS CQD/graphene photoFET (see Figure 1.10a) [29]. Under dark, the junction formed between PbS CQD and graphene fully depletes the graphene channel due to the atomic-thick nature of graphene. Under NIR light illumination, the photo-induced holes generated in the PbS sensitizing layer diffuse into the graphene layer while electrons are trapped inside CQDs, which leads to trap-assisted photoconductive gain (see Figure 1.10b). With the high carrier mobility of graphene, the device features an ultrahigh gain (10^8) with a detectivity 7×10^{13} jones.

Despite the ultrahigh gain achieved, the response time is rather slow (~ 10 ms) as shown in Figure 1.10c. This is due to that the charge separation in the CQD layer relies on the diffusion process. To address this, Konstantatos group proposed to integrate the PbS CQD photodiode composed of ITO/CQD atop graphene (see Figure 1.11a). The bias on the ITO electrode enlarges the depletion region in the CQD layer, significantly enhancing charge separation and collection efficiency in the photodiode (see Figure 1.11b). The device features a high gain of 10^5 and a temporal response of sub-milliseconds (see Figure 1.11c) [30].

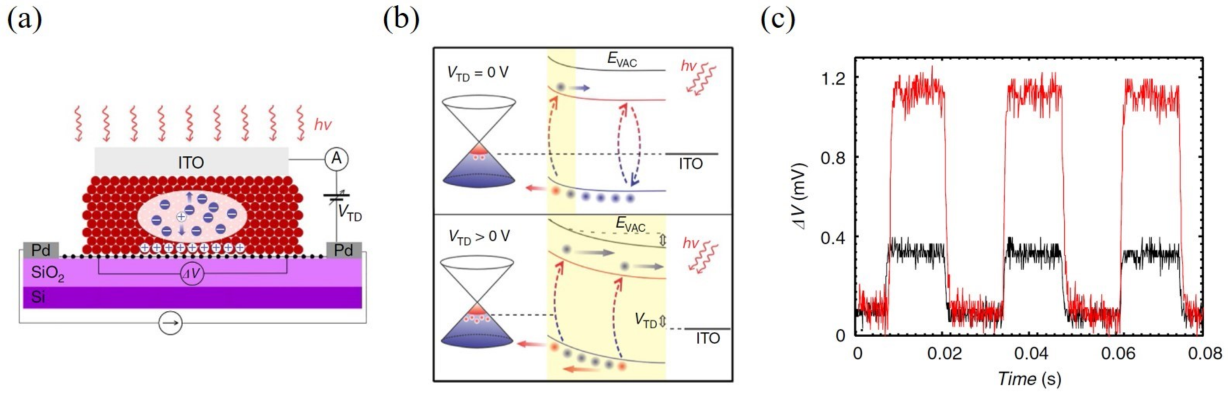

Figure 1.11. (a) Schematic view of CQD photodiode /graphene photoFET. (b) Band structure of the device, the generated photocarriers are swiftly separated with the aid of enhanced electric field by ITO electrode bias. (c) temporal response of the device showing sub-millisecond response. Reproduced from Ref. [30]. Copyright © 2016, The Author(s).

1.5.4 Si integration

It is challenging to utilize a standalone PbS CQD photodetector for imaging applications. One solution is combining the photodetector with a separate mechanical scanning apparatus; the drawbacks are the speed is slow as it is limited by the mechanical movement and the setup is bulky. Instead, the other option is to integrate PbS CQD photodetector with commercial Si-ROICs. Thanks to the solution processability PbS CQDs can be integrated into a large area on Si-ROICs *via* simple spin coating, spray, ink printing, etc.

In 2009, Hayden group presented a NIR image sensor in which a ternary blend (CQD:P3HT:PCBM) photodiode is integrated into ROICs (see Figure 1.12a) [31]. The device is capable of NIR light detection up to 1.8 μm, featuring a high rectification ratio of ~6000 (current ratio for forward and reverse voltage bias) and EQE up to 51%. However, a moderate normalized detectivity of only 2.3×10^9 jones was obtained.

In 2017, Konstantatos and Koppens groups proposed to integrate PbS CQD/graphene hybrid photoFET on CMOS ROICs and demonstrated a broadband (300-2000 nm) image sensor (see Figure 1.12b). The use of the hybrid photoFETs (discussed in Section 1.4.3) with a detectivity of up to 10^{12} jones can significantly enhance the sensitivity of the image sensor [32].

In 2022, Tang's group proposed to integrate an entire PbS CQD photodiode onto bottom ROICs. The working mechanism is by reading out the photocurrent to the bottom ROIC circuit through a gold bottom electrode (see Figure 1.13). The photodiode design supported fast temporal response and greatly suppressed the noise current; thus, the device rendered a high detectivity value of 2.1×10^{12} Jones and large 3dB bandwidth of 140 kHz [33].

Direct integration of CQD on Si-based upon the formation of CQD/Si heterojunction provides another possible route for the combination of CQD with ROIC without intermediate materials (e.g., bottom electrodes in Figure 1.12), possibly saving material usage and simplifying the fabrication process. Yet, one main challenge is the treatment of the CQD/Si interface, at which traps can capture photocarriers and significantly degrade device performance. The other challenge is constructing a favourable band alignment between Si and PbS CQD, for photocarrier transport and collection.

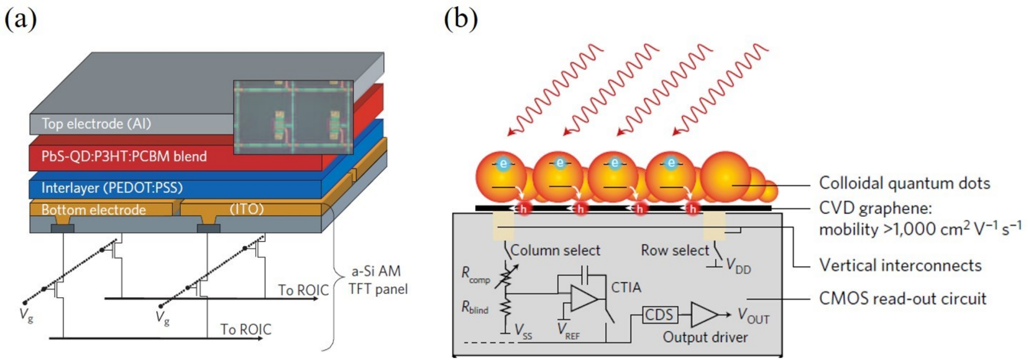

Figure 1.12. (a) Schematics of PbS CQD-based ternary photodiode integrated with commercial ROICs. Reproduced with permission [31]. Copy right 2009, Macmillan Publishers Limited. (b) PbS CQD/graphene hybrid photoFET integrated with ROICs. Reproduced with permission [32]. Copy right 2017, Macmillan Publishers Limited, part of Springer Nature.

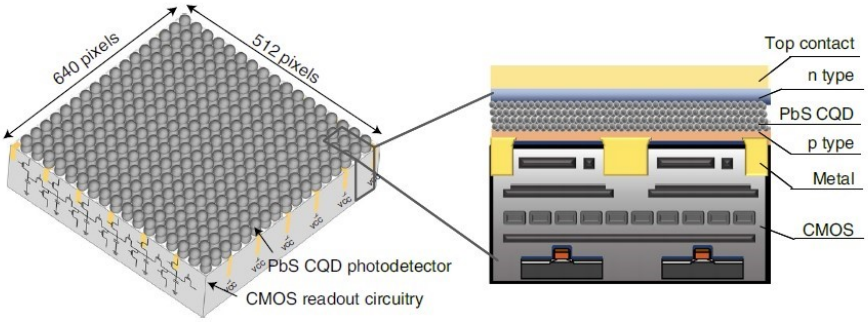

Figure 1.13. Schematics showing the integration of a PbS photodiode on Si ROICs through the bottom gold contact. Reproduced with permission [33]. Copyright © 2022, The Author(s), under exclusive licence to Springer Nature Limited.

In 2015, Sargent group demonstrated a PbS CQD (*n*-type)/Si (*p*-type) heterojunction photodiode (see Figure 1.14a) [34]. CH_3I was applied to passivate the Si surface, rendering an interface with favourable band alignment and much-reduced traps. The photodiode exhibited a 30% EQE and a detectivity of 1.5×10^{11} jones at 7V reverse bias (see Figures 1.14b,c). Ning's group designed and constructed an inverted structure photodiode consisting of a *p*-type PbS CQD/n-Si heterojunction (see Figure 1.15) [35]. The inverted structure afforded a better band alignment than the non-inverted structure. Finally, EQE of 22% and detectivity of 1.47×10^{11} jones were obtained without voltage bias (see Figure 1.15b, c).

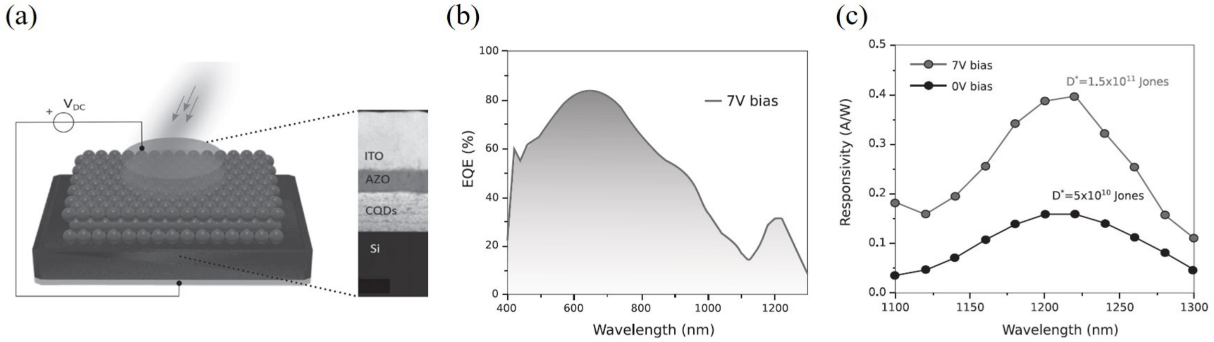

Figure 1.14. (a) Structure of CQD/Si heterojunction photodiode. (b) Dependence of EQE on wavelength at 7 V reverse bias. (c) Dependence of responsivity on wavelength at 0 and 7 V reverse bias. Detectivity was calculated at 1230 nm. Reproduced with permission [34]. Copy right 2015 WILEY-VCH Verlag GmbH & Co. KGaA, Weinheim.

Incorporating CQD/Si heterojunction and effective surface treatment by CH_3I, Adinolfi et al. designed a phototransistor in which *p*-type Si is applied as a high-mobility channel and *n*-type CQD as a sensitizing layer (see Figure 1.16a). The channel conductivity is controlled by the photovoltage generated by rectifying CQD/Si junction and by the gate voltage (n+ Si gate at the back; see device structure in Figure 1.16a). Thus the device is also termed as photovoltage field-effect transistor (PVFET) [36]. By careful tuning of Si thickness and doping, the Si channel is depleted under dark, leading to a lower dark current and reduced device noise. Thanks to the device transconductance, gain > 10^4 and detectivity of 1.8×10^{12} jones were achieved (see Figure 1.16b), much higher than CQD/Si heterojunction photodiode. Due to the reduced interface traps, the temporal response of the device is as short as 10 μs, one of the shortest among proposed PbS CQD phototransistors (see Figure 1.16c).

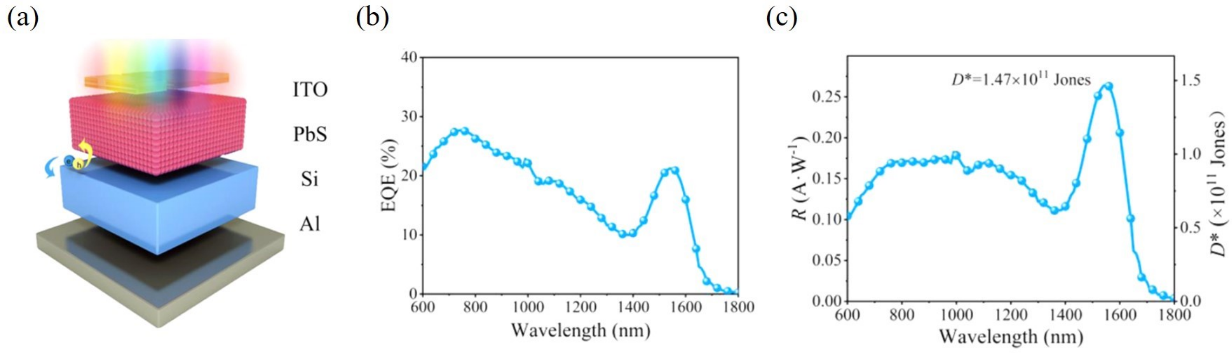

Figure 1.15. (a) Structure of inverted CQD/Si heterojunction photodiode. (b) EQE vs. wavelength at 0 V bias. (c) Dependence of responsivity and detectivity on wavelength at 0 V bias. Reproduced with permission [35]. Copy right 2020 American Chemical Society.

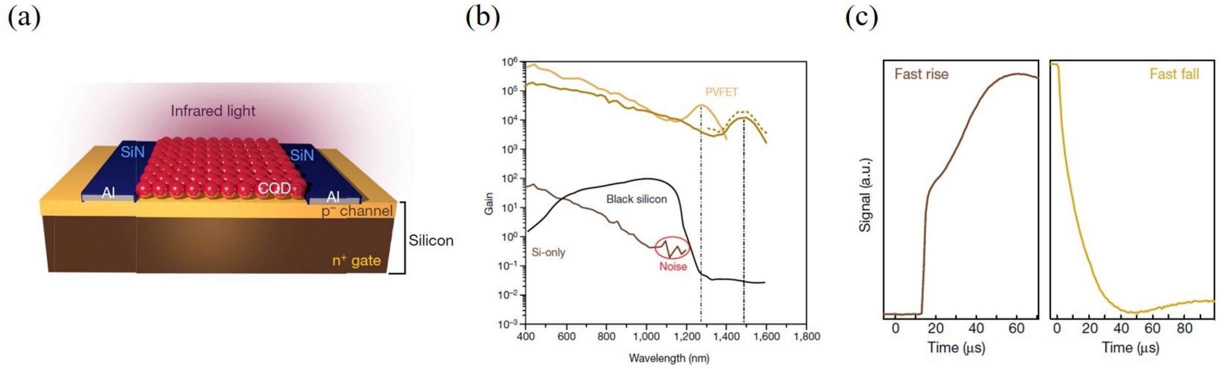

Figure 1.16. (a) Device structure of PVFET. (b) Dependence on wavelength showing a gain of PVFET and bare silicon at V_{DS} = 2 V (solid line) and V_{DS} = 3 V (dashed line). (c) Fast temporal response of the PVFET. Reproduced with permission [36]. Copy right 2017 Macmillan Publishers Limited, part of Springer Nature.

1.6 Thesis objectives

The objectives of this thesis are to develop fast and efficient devices for NIR photodetection. The core material of the study is PbS CQDs, based upon which we aim to develop a fast NIR CQD photodetector through device engineering. More importantly, the main goal is to develop on-Si CQD NIR photodetection as this introduces a plethora of new applications. It could be CQDs integrated with Si waveguide with miniaturized on-chip device size for Lidar application, or large area and monolithic integration with ROIC circuit for building low-cost NIR CMOS image sensors (CISs). To do this, we aim to propose and develop possible on-Si integration strategies that are straightforward and enable fast and efficient photodetection. Further, the proposed methods should be compatible with the mature CMOS technology to lower the cost of on-Si CQD photodetectors.

1.7 Thesis outline

Chapter 2 is dedicated to providing an alternative route for achieving a NIR PbS photodiode with the fastest response possible from PbS CQDs even with limited carrier mobility. By using an analytical model which is originally utilized for studying silicon photodiode, we demonstrate and explain the physical mechanism governing the operating speed of NIR PbS photodiode.

In chapter 3, we present a new architecture for PbS CQD on Si integration, POSFET, of which device fabrication is fully compatible with the current COMS manufacturing process. With the help of simulation, we provide a detailed description of the working mechanism of the POSFET under NIR illumination. An experimental proof-of-concept is also presented to prove the feasibility of such a novel structure.

Chapter 4 investigates PbS photodetector on Si using an alternative integration strategy, which is based on PbS CQD/Si heterojunction. The chapter focuses more on comprehensive comparisons of PbS CQDs with other two materials commonly used for NIR light detection, Ge and InGaAs, in a Si photonics platform. We take photodetectors that are integrated with waveguides as an example, examining their performance in C-band wavelengths. Figure-of-merits including responsivity, dark current and 3dB bandwidth are investigated.

Chapter 5 is dedicated to the investigation of the CQD/Si heterojunction interface. We explore surface treatment for Si substrate, which is found to be crucial for lowering interface traps and thus building a high-performance CQD/Si heterojunction photodetector. A two-step treatment method is proposed and compared with the standard one-step method through various techniques including TPC and TPV measurement. Performances of fabricated photodiode devices using the two methods are also compared.

In chapter 6, with the proposed surface treatment method in chapter 5, CQD inks are then integrated onto Si. The necessary and benefits of an extra insertion layer of EDT-caped CQD are discussed. The high-quality and stable CQD inks lead to highly efficient CQD ink/Si heterojunction photodiodes with superior stability.

Chapter 7 contains a simulation study, which investigates a NIR CQD-based CIS. The integration strategy is based on CQD/Si heterojunction. The feasibility of such a strategy is proven by simulation.

Finally, a summary of key accomplishments and contributions in this thesis will be discussed in Chapter 8. Some of the possible future directions and works will also be elaborated.

2. Ultrafast PbS colloidal quantum dot photodiodes

2.1 Background

NIR PbS photodetectors with unprecedented gain and sensitivity have been developed. By integrating novel high-mobility 2D materials and other TMD materials (e.g. graphene [29], [30], molybdenum disulphide [37]–[39], tungsten disulphide [40], black phosphorus [41], [42]), PbS CQD photodetectors were achieved with a responsivity up to 10^8 A/W, but at an expense of high voltage bias [43]. In addition, their operating speed is far slower compared to commercial NIR photodetectors, with a response time ranging from several milliseconds to sub-seconds. The slow response time prevents its use from a plethora of important applications such as fast time-of-flight cameras for autonomous vehicles, real-time vision for manufacture monitoring, and optical telecommunications. Thus, a new strategy that produces a highly responsive PbS CQD photodetector is required.

2.2 Methods

Preparation of so-gel ZnO: Zn(Ac)2·2H2O (1.5 g) and ethanolamine (420 μL) were mixed in ethanol (30 mL). The mixture of ZnO solution was filtered through a filter (0.45 μm) and stored in the refrigerator for future use.

Synthesis of PbS CQDs: All reagents were purchased from Sigma-Aldrich and used as received. Lead oxide (0.9 g; 4 mmoles), oleic acid (16.9 g; 60 mmoles), and octadecene (25 mL; 79 mmoles; ODE) were combined in a three-neck flask charged with a magnetic stir bar. The mixture was stirred under vacuum at 110 ˚C for 2 hours to form a visually transparent system. The flask was backfilled filled with nitrogen and heated using a standard heating mantle. Upon reaching 120 ˚C, an octadecene (ODE) solution of hexamethyldisilathiane (420 μL; 2 mmoles in 10 mL OED) was added rapidly in a single aliquot and the heating mantle was removed from the flask and stirring was off. After the reaction cooled to room temperature acetone (40 mL, Fisher Scientific, Certified ACS Reagent) was added and the solid was recovered upon centrifugation at 4000 rpm. The precipitate was re-suspended in toluene (Fisher Scientific, Certified ACS Reagent) and purified by acetone followed by centrifugation. This process was repeated three times. Finally, PbS CQDs were dried under vacuumed at room temperature for 15 mins and then dispersed in octane with a concentration of 50 mg/mL.

Fabrication of PbS CQD photodiode: Before fabrication, the ITO glass was ultrasonically cleaned with Triton™ X-100 in deionized water, and then cleaned with isopropyl alcohol (IPA), after which the ZnO solution was spun cast on ITO glass at 4000 rpm for 30 s and then heated at 280 ˚C for 20 mins to convert the precursor solution to ZnO film *via* hydrolysis. The oleate-capped PbS CQDs were synthesized following a hot injection method reported before [44]. The PbS CQDs were then dissolved in octane with a concentration of 50 mg mL^{-1}. The PbS CQD solution was then deposited on the ITO glass *via* the layer-by-layer method: for each layer, 50 µL of the CQD solution was dropped and spun at 2500 rpm for 30 s. Oleate-capped CQDs are electrically insulating, and the ligands have to be replaced by shorter ligands. For the PbS-TBAI layer, TBAI solution (10 mg mL-1 in methanol) was applied to the substrate for 30 s, and spun at 2500 rpm for 10 s, followed by a two-time acetonitrile rinse. Whereas for the EDT-PbS layer, EDT solution (0.01 vol% in acetonitrile) was applied. Finally, Au (120 nm) was thermally evaporated on the PbS film.

Device characterizations: Characterizations including current-voltage, capacitance-voltage, TPC, dark and photo-CELIV measurements were performed with Paios all-in-one system (Fluxim). The system equips with a 60-mW white LED which has a rise time of 100 ns and a sampling rate of 60

MS/s. Spectral EQE was measured with a quantum efficiency measurement system (Sciencetech Inc).

2.3 Results and discussions

The configuration for the PbS photodiode studied in this work is depicted in Figure 2.1a, which consists of ITO/ZnO nanoparticles/tetrabutylammonium iodide (TBAI)-treated PbS (termed PbS-TBAI)/1,2-ethanedithiol (EDT)-treated PbS (termed PbS-EDT)/Au. Using the energy level values published in the literature [45], the schematic band diagram is depicted in Figure 2.1b. Photo-carriers generated in the space charge region will drift to electrodes while carriers generated in the neutral region have to diffuse to the space charge region before being collected. As will be discussed following, the neutral region should be eliminated to achieve an ultrafast photodiode. Both ZnO and PbS layers were uniformly spun casting onto ITO glass (see Figure 2.2). To have easier control of PbS thickness, the PbS active layer was prepared *via* layer-by-layer fashion [46], through which various thicknesses were obtained by simply changing the number of PbS layers.

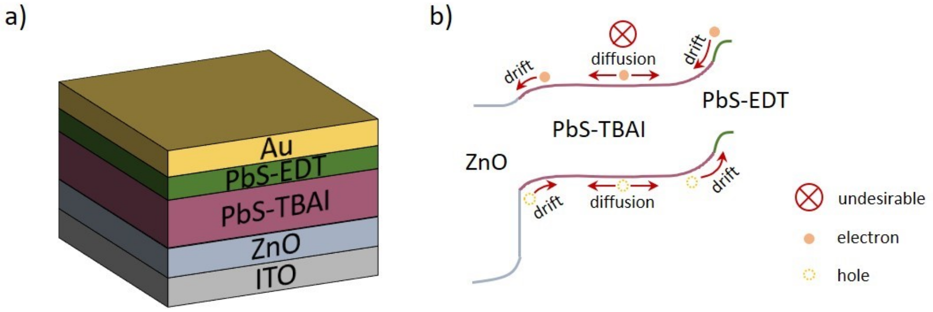

Figure 2.1. (a) Schematic of photodiode structure. (b) Schematic illustration of band diagram at short-circuit condition showing two junctions formed at ZnO/ PbS-TBAI and PbS-TBAI/-EDT interfaces. For achieving a fast photodiode at zero bias, neutral region and carrier diffusion are undesirable. Reprinted with permission from [47]. Copyright © 2020, American Chemical Society.

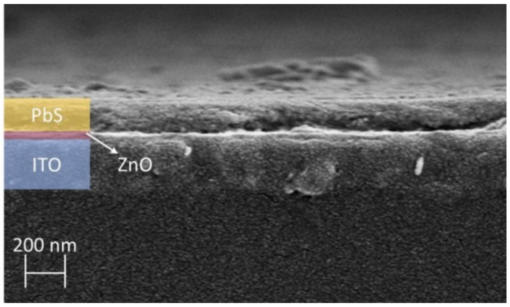

Figure 2.2. Cross-sectional SEM image of a PbS-based photodiode consisting of ITO/ZnO/PbS. Reprinted with permission from [47]. Copyright © 2020, American Chemical Society.

For a semiconductor photodiode upon light illumination, the rise time (τ_{rise}) is dominated by the RC time constant (τ_{RC}) and the time for the collection of photo-generated carriers, which comprises drift and diffusion components. The drift process describes a fast movement of generated photocarriers driven by the electric field in the space-charge region, whereas the diffusion component is determined by a slower movement of the minority carriers induced by carriers' concentration gradient in the neutral region. The charge collection times for drift (τ_{drift}) and diffusion (τ_{diff}) processes are defined as times required for the carriers to reach the edges of the space-charge and neutral regions, respectively. Finally, the rise time takes the form of the square root of the three components combined and is given in the literature as follows [48]:

$$\tau_{\text{rise}}=\sqrt{\tau_{\text{diff}}^{2}+\tau_{\text{drift}}^{2}+(2.2\tau_{\text{RC}})^{2}} \tag{2.1}$$

For τ_{diff}, it is usually undesirable when designing a fast photodiode, mainly due to two main aspects. First, the diffusion process, as mentioned above, is normally much slower than drift. Second, the resistance of the neutral region also contributes to RC time and slows down the photodiode's response. Therefore, to build an ultrafast PbS-based photodiode, the diode should be fully depleted at zero applied bias (Figure 2.1 b).

For τ_{drift}, we have

$$\tau_{\mathrm{drift}}=\frac{d}{\mu E}=\frac{d^2}{\mu V}=\frac{d^2}{\mu(V_0\text{-}V_{\mathrm{r}})}$$

(2.2)

where d is the thickness of the space-charge region, μ is carrier mobility, E is electric field strength in this region, V_0 is junction built-in potential and V_{r} is applied voltage. For a fully depleted photodiode, junction built-in potential V_0 can be simplified as the difference between the Fermi energy of ZnO (E_{FZnO}) and the work function of metal contact (W_{Au}) divided by the electric charge.

Finally, τ_{RC} is given by

$$\tau_{\mathrm{RC}}=R_{\mathrm{S}}C$$

(2.3)

where R_{S} is diode series resistance, arising from contact resistance and resistance of neutral region which is zero in a fully depleted diode; and C is junction capacitance, given by

$$C=\frac{\varepsilon_0\varepsilon_{\mathrm{r}}A}{d}$$

(2.4)

where ε_0 is the permittivity of free space, ε_{r} is the dielectric constant of PbS QD film and A is the photodiode active area [49]. Note that the photodiode under a light pulse resembles a capacitor being discharged. In this case, τ_{RC} is the time required to discharge the photodiode to $1/e$ (36.8%) of its initial stored charge, and a factor of 2.2 must be multiplied in Equation 1 to compensate it for 10% to 90% rise time. From Equation (2.1)-(2.4), rise time τ_{rise} as a function of d can be calculated, given that necessary parameters are known, which are R_S, μ, ε_r, E_{FZnO}, W_{Au} and A.

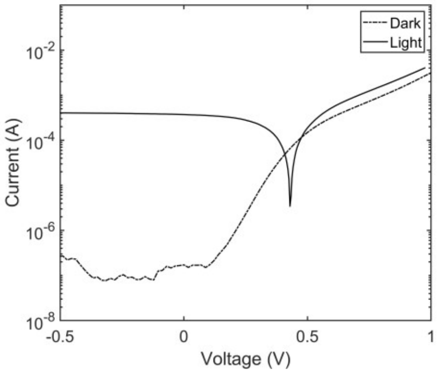

Figure 2.3. I-V characteristic under light and dark conditions. Reprinted with permission from [47]. Copyright © 2020, American Chemical Society.

Series resistance R_S of the photodiode was extracted from the I-V characteristic as shown in Figure 2.3 as explained here. According to equivalent circuit for the photodiode model, as shown in Figure 2.4 below, we have:

$$I=-I_{\mathrm{ph}}+I_0 \exp\left(\frac{q(V\text{-}IR_{\mathrm{S}})}{nkT}\right)+\frac{V\text{-}IR_{\mathrm{S}}}{R_{\mathrm{SH}}} \tag{2.5}$$

where I is the output current, Iph is the generated photo current, I_0 is reverse saturation dark current, n is ideality factor, k is Boltzmann constant and T is the temperature. According to this equation, two methods can be used to determine series resistance of a photodiode.

Method1: At the point around open circuit voltage ($I \approx 0$), and considering $R_{\mathrm{SH}} \gg R_S$, the equation simplifies into

$$V = IR_S + \frac{nkT}{q}\ln\frac{I_{ph}}{I_0} \tag{2.6}$$

Thus, R_S is easily obtained as $R_S = |1/(dI/dV)|_{I=0}$, which is the invert value of the slope of the I-V curve at the open circuit voltage.

Method 2: according to Equation 2.5, under dark $\ln(I)$ will be linearly proportional to terminal voltage V at low currents $[nkT/q \times \ln(I/I_0) = V - IR_S]$. At high current, however, it will deviate from the straight line and the voltage deviation is due to the voltage drop on the series resistance, which gives $R_S = dV/I$.

Similarly, shunt resistance is obtained as $R_{SH} = |1/(dI/dV)|_{V=0}$, which is the inverse slope value of I-V characteristics at short circuit conditions under the light.

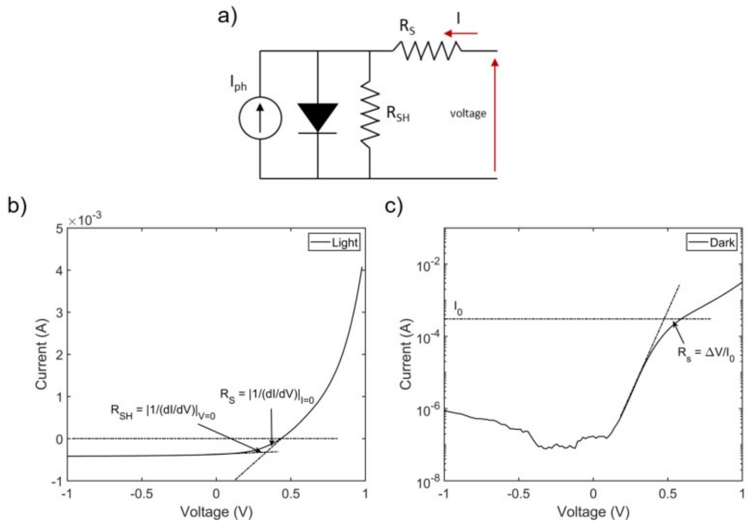

Figure 2.4. (a) Equivalent circuit model for a photodiode. I-V characteristic under (b) dark and (c) light conditions. Reprinted with permission from [47]. Copyright © 2020, American Chemical Society.

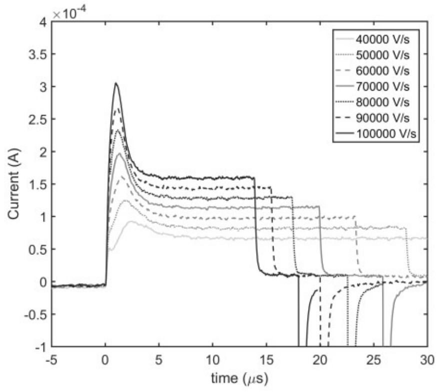

Figure 2.5. Photo-CELIV method for calculating carrier charge mobility. Reprinted with permission from [47]. Copyright © 2020, American Chemical Society.

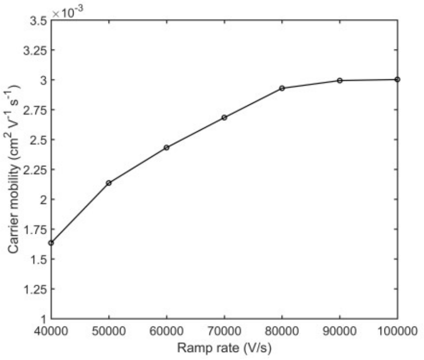

Figure 2.6. Obtained mobilities for each ramp rate. Reprinted with permission from [47]. Copyright © 2020, American Chemical Society.

Carrier mobility was analyzed by photo-CELIV (charge extraction by linearly increasing voltage) measurement at different voltage ramps [50], [51], and obtained characteristic is shown in Figure 2.5. The mobility was calculated using following equation [51],

$$\mu = \frac{2d^2}{3\frac{\mathrm{d}V}{\mathrm{d}t}t_{\mathrm{m}}^2(1+0.36\frac{\Delta j}{j_0})}$$

(2.7)

where d is the thickness of the active layer, $\mathrm{d}V/\mathrm{d}t$ is the voltage ramp rate, t_m is time when maximum current occurs, Δj is the maximum extracted current and j_0 is the displacement current plateau. The resulting mobilities are dependant on ramp rate but show an upper limit at 3×10^{-3} $\mathrm{cm^2V^{-1}s^{-1}}$, as displayed in Figure 2.6.

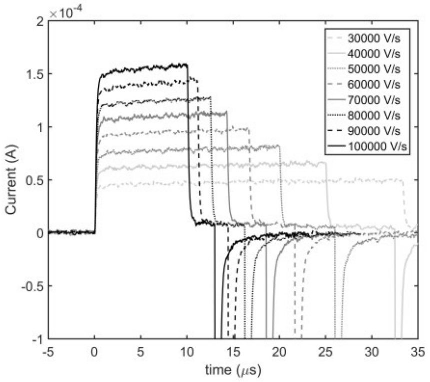

Figure 2.7. Dark-CELIV method for calculating dielectric constant of the PbS film. Reprinted with permission from [47]. Copyright © 2020, American Chemical Society.

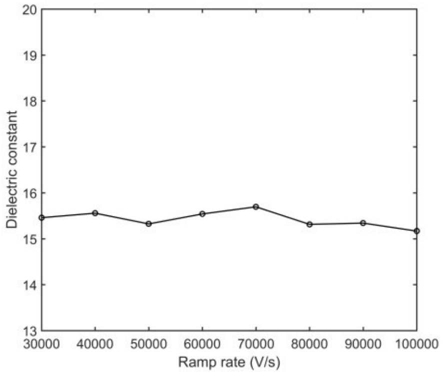

Figure 2.8. Obtained dielectric constant for each ramp rate. Reprinted with permission from [47]. Copyright © 2020, American Chemical Society.

Dark-CELIV measurement was used to determine the dielectric constant of CQD film [52], which is explained here. The dielectric constant of the PbS film was determined from dark-CELIV method. A fully depleted photodiode was fabricated which resembles a capacitor. According to parallel plate capacitor equation

$$Q=CV \tag{2.8}$$

we have

$$i=\frac{\mathrm{d}Q}{\mathrm{d}t}=C\frac{\mathrm{d}V}{\mathrm{d}t} \tag{2.9}$$

Insert Equation 2.4 into Equation 2.9, we have

$$\varepsilon_\mathrm{r}=\frac{id}{\varepsilon_0 A}\frac{1}{\frac{\mathrm{d}V}{\mathrm{d}t}} \tag{2.10}$$

where i is the measured displacement current, $\mathrm{d}V/\mathrm{d}t$ is the voltage ramp rate in dark-CELIV measurement. In the experiment, the voltage was ramped at a constant ramp rate to 1V in the course of tens of microsecond. According to Equation 2.9, the displacement current is a constant value when voltage is linearly ramped. The obtained displacement current with different voltage ramp from dark-CELIV measurement is shown in Figure 2.7. Based on Equation 2.10, dielectric constant was determined to be 15.5, as displayed in Figure 2.8. These parameters and other necessary ones are listed in Table 2.1.

Table 2.1. Parameters for rise time calculation.

Parameter	E_{FZnO}	W_{Au}	R_{S}	R_{SH}	μ (cm^{2}V^{-1}s^{-1})	ε_{r}	A (mm^2)
Value	4.2 eV	5.4 eV	320 ohms	360 kohms	3×10^{-3}	15.5	0. 785

With the provided parameters, τ_{RC}, τ_{drift} and overall τ_{rise} were determined as a function of PbS thickness, as displayed in Figure 2.9. The depletion width of junction formed between PbS-TBAI (*n*-type) and PbS-EDT (*p*-type) at zero bias is calculated by Equation 2.11, which is derived from the electrostatic analysis of a p-n junction shown below,

$$x_{\mathrm{d}}=\sqrt{\frac{2\varepsilon_0\varepsilon_{\mathrm{r}}}{q}\left(\frac{1}{N_{\mathrm{a}}}+\frac{1}{N_{\mathrm{d}}}\right)\phi_{\mathrm{i}}} \tag{2.11}$$

where $N_{\mathrm{d}}=10^{15}$ cm^{-3} and $N_{\mathrm{a}}=10^{17}$ cm^{-3} are doping concentrations for *n*-type TBAI- and *p*-type EDT-PbS, ϕ_{i}=0.19eV is built in the junction built-in potential [45]. Finally, we have x_{d}=580 nm, which is much larger than the thickness of fabricated devices in this work. In this case, the PbS thickness considered in Figure 2.9 is smaller than d_0, and thus τ_{diff} was neglected when calculating τ_{rise} in Equation 2.1. It was observed in Figure 2.9 that transit time increases while RC constant decreases as PbS thickness increases. With the synergic effect of transit time and RC delay, the overall τ_{rise} reaches a minimum value of ~0.38 μs at a thickness $d_{\mathrm{m}} \approx 245$ nm. This means that with same material and architecture, one can still achieve a faster PbS photodiode by balancing RC time delay and charge transport effect.

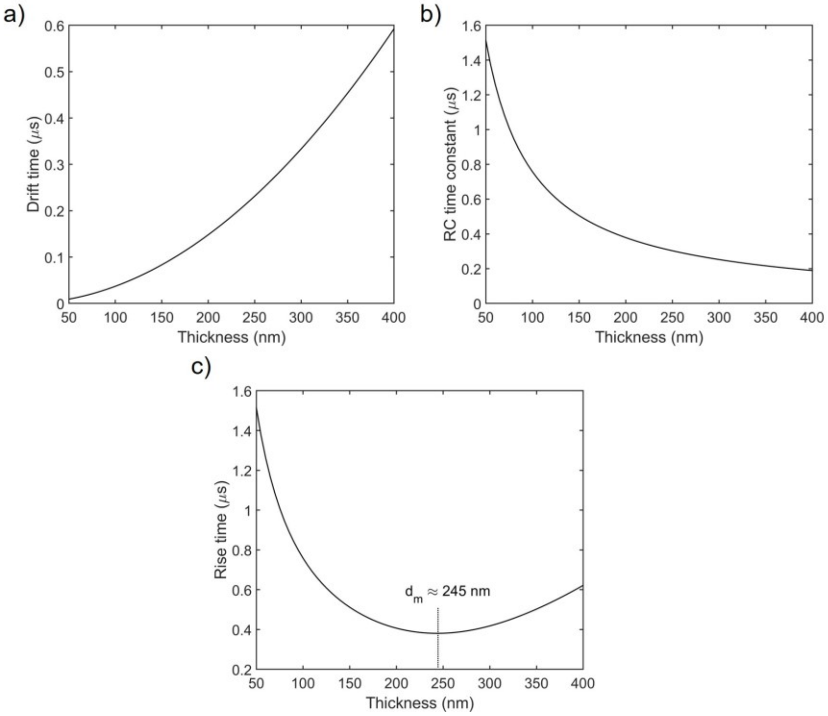

Figure 2.9. Simulated (a) τ_{RC}, (b) τ_{drift} and (c) overall τ_{rise} as a function of thickness of PbS active layer. Reprinted with permission from [47]. Copyright © 2020, American Chemical Society.

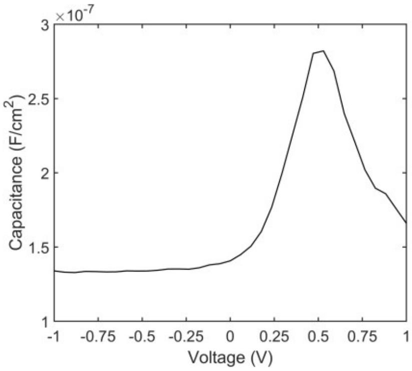

Figure 2.10. Capacitance-voltage measurement for device with 16-layer of PbS. Reprinted with permission from [47]. Copyright © 2020, American Chemical Society.

To prove the theory, devices with seven different thicknesses were fabricated. The thickness for ZnO was unchanged while PbS with an even number of layers raging from 4-16 were selected. The thickness for each device was measured by a surface topography profiler. For the thickest device with 16 layers of PbS, a capacitance-voltage profile was measured as illustrated in Figure 2.10. The measured capacitance remains constant (~ 135 nF/cm^2) under reverse bias. This proves that this device and others with smaller PbS thickness are fully depleted.

To experimentally determine the rise time for PbS photodiode, a short light pulse with a duration of 20 μs was shine on the photodiode, and the transient photocurrent (TPC) was measured. A typical TPC response was shown in Figure 2.11, which shows ultrafast rise and fall edges of signal that are under 1 μs. Figure 2.12 shows measured rise times for all fabricated devices. For 12-layer PbS photodiode we have achieved a fastest rise time and fall time of both 0.33 μs at zero bias voltage. The ultra fast signal rise and fall render our device to be one of the fastest NIR PbS photodiodes ever reported, making it suitable for applications such as time-of-flight sensing. Meanwhile, at short circuit condition, the obtained experimental results show good accordance with the proposed model, but large deviation was observed at 0.5 V reverse bias, especially for thinner photodiode. This could be attributed to the reason that for an extremely thin diode at reverse bias the depletion region reaches into ZnO lyaer by a larger extend and even into ITO layer. In this case, the active layer thickness d is larger than that considered in our model. Based on Equation 2.1, this brings overestimation of capacitance in our predicted model and therefore rise time predicted by the model is larger than measured values in the experiment.

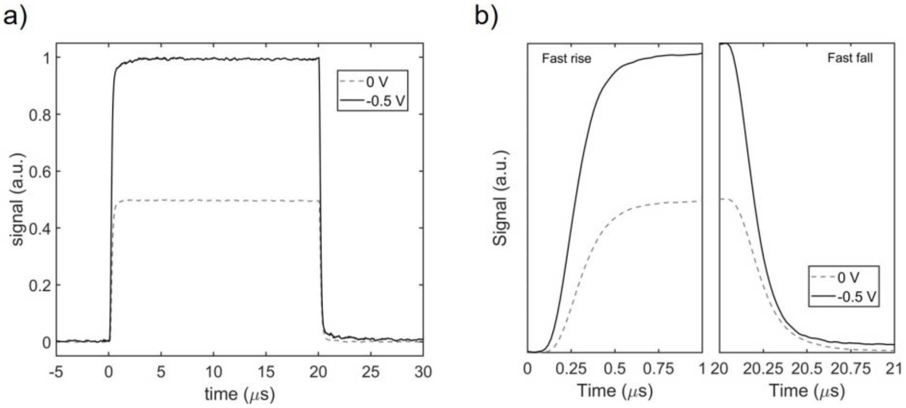

Figure 2.11. (a) TPC response of a 12-layer PbS photodiode for 0 and -0.5 V biases. (b) Zoom-in figure showing components of fast rise and fall edges. Reprinted with permission from [47]. Copyright © 2020, American Chemical Society.

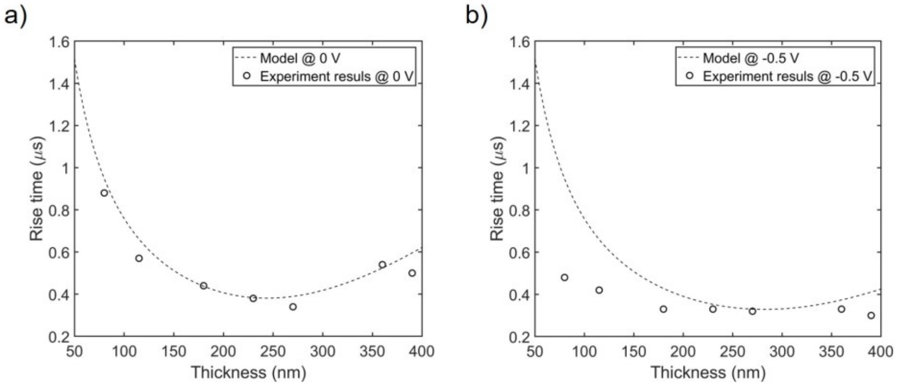

Figure 2.12. Experimentally measured rise time for devices with different thicknesses at (a) 0 V and (b) -0.5 V bias. Reprinted with permission from [47]. Copyright © 2020, American Chemical Society.

Spectral EQE of the PbS photodiode was measured in Figure 2.13a at short circuit condition and photoconductive mode (reverse biased). When the photodiode was reversely biased with 0.3 and 0.5 V, EQE value exceeds 100%. We posit that this higher than unity gain is due to photoconductive gain induced by HTL electron-trapping effect, which also has been reported in other literatures [26]–[28], [53].

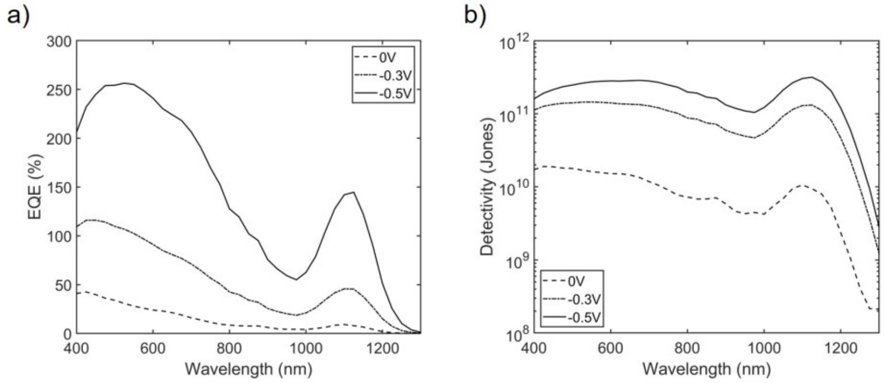

Figure 2.13. (a) Spectral EQE and (b) detectivity of the fastest device (12-layer PbS) at 0 and -0.5 V bias. Reprinted with permission from [47]. Copyright © 2020, American Chemical Society.

Another figure of merit for a photodetector is the specific detectivity. At photoconductive mode, noise current is dominated by shot noise,

$$i_{\mathrm{n}}=\sqrt{2qI_{\mathrm{d}}\Delta f} \tag{2.12}$$

where q is electric charge, I_{d} is the dark current and Δf is the detection bandwidth. Whereas in short circuit mode with zero voltage bias, noise is dominated by Johnson–Nyquist noise (thermal noise), which is expressed as

$$i_{\mathrm{n}}=\sqrt{\frac{4k_{\mathrm{B}}T\Delta f}{R_{\mathrm{SH}}}} \tag{2.13}$$

where k_B is the Boltzmann constant, T is temperature and R_{SH} is shunt resistance of the photodiode (see equivalent circuit in Figure 2.4). Based on Equations 1.3, 1.4, 2.12, and 2.13, the spectral D^* was determined as illustrated in Figure 2.13b. At 0.5 V reverse bias, the PbS photodiode can achieve a highest detectivity value of 3.2×10^{11} Jones at 1125 nm. Finally, we compared the main figure of merits of our developed and other previously reported NIR photodetectors in Table 2. Our NIR PbS photodiode shows exceptional speed and high sensitivity at a very low voltage bias. Especially, the photodiode outperforms the commercially available Ge photodiode (Ge-FDG03) in terms of both speed and sensitivity.

Table 2.2. Comparison of figure-of-merits between different reported NIR photodetectors

Material	Structure[a)]	Rise/fall time	Detectivity [jones]	Voltage bias [V]	Area	Ref.
PbS QD/ZnO	PD	0.3/0.3 [μs]	3.2×10^{11} @ 1125 nm	V_r = -0.5	0.8 [mm^2]	[47] This work
Ge-FDG03	PD	0.6/0.6 [μs]	1×10^{11} @ 1550 nm	V_r = -3	7.1 [mm^2]	Commercial
ITO/PbS QD/graphene	PT	230 [μs][b)]/-	1.0×10^{12} @ 900 nm	V_{GS} = 75	100 [μm^2]	[30]
PbS QD/a-ZnO	PC	640/50 [ms]	3.4×10^{11} @ 1310 nm	V_{DS} = 20	4500 [μm^2]	[54]
PbS QD/Perovskite	PC	42/42 [ms]	3.0×10^{11} @ 940 nm	V_{DS} = 10	0.05 [mm^2]	[55]
Spiro/PbS QD/ZnO	PD	4.4/8.2 [μs]	2.0×10^{12} @ 1000 nm	V_r = -1	11.5 [mm^2]	[18]
PbS QD	PC	350 [μs] [b)]/-	1×10^{9} @ 1550 nm	V_{DS} = 1	1.6 [mm^2]	[56]

MoS_2/TiO_2/PbS QD	PT	-/12 [ms]	2.2×10^{12} @ 980 nm	$V_{DS} = 1$ $V_{GS} = 15$	50 [μm^2]	[39]
TiO2/PbS QD/PolyTPD	PD	57/86 [µs]	1.2×10^{12} @ 940 nm	$V_r = -3$	-	[49]
PbS QD/WS_2	PT	-/0.2 [s]	9×10^{11} @ 1800 nm	$V_{DS} = 1$ $V_{GS} = 20$	50 [μm^2]	[40]
MoS_2/PbS QD	PT	950/1000 [µs]	3.7×10^{10} @ 850 nm	$V_{DS} = 1$ $V_{GS} = 0$	200 [μm^2]	[38]
PbS QD/ITO	PD	0.11/0.23 [ms]	1.96×10^{10} @ 1550 nm	$V_r = -1$	2500 [μm^2]	[53]
PbS QD/Si	PT	35/10 [µs]	1.8×10^{12} @ 1300 nm	$V_{DS} = 2$ $V_{GS} = 0$	5000 [μm^2]	[36]
MoS_2	PT	-/10 [ms]	2×10^{10} @ 1000 nm	$V_{DS} = 10$ $V_{GS} = 35$	400 [μm^2]	[57]
PbS QD	PC	3.6/29.5 [ms]	7.5×10^{11} @ 990 nm	$V_{DS} = 10$	0.7 [mm^2]	[58]
MoO_3/PDTP-DFBT:$PC_{71}BM$/PbS QD/PEIE/SnO_2	PD	320 [µs] b)/-	7.9×10^{11} @ 900 nm	$V_r = -7$	7 [mm^2]	[26]
MoS_2/BP	PT	15/70 [µs]	2.1×10^{9} @ 1550 nm	$V_{DS} = 3$ $V_{GS} = 35$	-	[42]
PbS QD/MoO_3	PT	10/12 [µs]	2.1×10^{10} @ 1000 nm	$V_{DS} = 5$ $V_{GS} = 1$	7500 [μm^2]	[59]
PbS QD:Ag NP	PC	35 [ms] b)/-	7.1×10^{10} @ 850 nm	$V_{DS} = 40$	1.5 [mm^2]	[21]
P3HT:PCBM:PbS QD:ZnO QD/PEDOT:PSS	PD	160 [µs]	2.3×10^{11} @ 930 nm	$V_r = -3$	6 [mm^2]	[27]
ZnO/PbS/NiO	PD	8.5 [µs]/-	1.1×10^{12} @ 1135 nm	$V_r = -1$	4.6 [mm^2]	[24]

Si/perovskite	PD	0.52/2.44 [µs]	2.2×10^{10} @ 1064 nm	V_r = -1	40 [mm^2]	[60]

[a] PD, PC and PT stand for photodiode, photoconductor, and phototransistor, respectively.

[b] rise time is estimated by $\tau_{\text{rise}} = 0.35/f_{3\text{dB}}$ [4], where $f_{3\text{dB}}$ is the 3dB bandwidth.

2.4 Summary

To summarize, we have developed a NIR PbS QD photodiode with an ultrafast photo-response at low voltage bias. By optimizing synergistic effect of the inherent RC time delay and carrier charge transport process, we have achieved fastest rise/fall times of both 0.33 µs at reverse 0.5 V, making it one of the fastest NIR PbS photodiode ever reported. The photodiode has high gain with an EQE value approaching 150% at 1125 nm, induced by photoconductive gain effect. It is also highly sensitive with a specific detectivity of 3.2×10^{11} jones at 1125 nm.

Future works includes utilizing higher-mobility QDs and apply the design process developed in this work to fabricate faster PbS QD NIR photodiode. Considering the rapid development in PbS QD chemistry in recent years, orders of improvement in the carrier mobility can be expected in the future. In this case, with the proper design, one can achieve an NIR PbS photodiode with a rise time of only tens of picosecond, which corresponds to several to tens of GHz bandwidth. This holds great promises for low-cost high-frequency NIR detection in applications such as LiDAR systems for self-driving cars.

3. Photodiode-oxide-semiconductor field-effect transistor

3.1 Background

As discussed in Section 1.4, tremendous attentions have been received for CQD integration on Si to extend the spectral range of Si-based microelectronics. In 2017, Adinolfi et al. made the breakthrough proposing a novel device strcuture termed as PVFET [36] and device structure is shown in Figure 1.16. In the presented work, authors used Si as the conducting channel and appropriately adjusted channel doping to achieve a depleted CQD/Si in the dark to minimize the dark current. This photodetector, combines photovoltaic effect and transconductive gain, shows merits of high gain ($\sim 10^4$), fast speed (~10 μs), and low dark current (10^{-1}-10^1 $A \cdot cm^{-2}$). Nonetheless, the device performance can be further improved. The rectifying CQD/Si junction facilitating photocarrier transports between CQD and Si channel would, conversely, create significant gate current at high frequency. This can pose great challenges to junction reliabilities and heat dissipations. Meanwhile, chemicals for CQD/Si interface treatment have to be judiciously selected to achieve an energy-band-aligned trap-free interface (rectifying heterojunction) for photocarriers transfers. We propose to separate CQD layer with Si channel and utilize photovoltage generated by a CQD photodiode to modulate channel conductivity.

3.2 Methods

Device simulations: POSFET were simulated using commercial software, Lumerical FDTD Solutions and DEVICE suite. FDTD Solutions was used to calculate the NIR light absorption and carrier generation in CQD photodiode, and DEVICE was utilized to calculate the electrical performance of the POSFET.

Synthesis of PbS CQDs: PbS CQD synthesis is described in method in section 2.2.

CQD photodiode fabrication: Photodiode fabrication is similar as described in section 2.2.

Device characterizations: The dark and light currents were measured using Keithley 2400 source meters. For light power dependant study, a diode laser source (Newport LQA) with wavelength of 635 nm is utilized as light source, and its output beam power, measured by Newport S120C power meter, can be adjusted by changing the supply voltage. Its spectral responsivity studies were carried out with the help of an EQE characterization system (Sciencetech Inc).

3.3 Results and discussions

The proposed structure is shown in Figure 3.1. The *p*-type (doping concentration, 5×10^{15} cm^{-3}) silicon is implemented as the channel (channel length of 2 μm). Source and drain electrodes made of aluminum are on the front side of the device, with two heavily doped n^{+} wells (2×10^{18} cm^{-3}) creating ohmic contacts. The CQD photodiode acting as a gate is separated from the channel by a thin layer of oxide with a thickness of 10 nm. In the diode, the thickness and doping level for n- and p-doped layer are 0.34 μm, 1×10^{16} cm^{-3} and 0.1 μm, 1×10^{16} cm^{-3}, respectively. Comparing with the commercial metal-oxide-semiconductor field-effect-transistor (MOSFET) which employs metal/polysilicon as the gate, the CQD photodiode is instead applied in the POSFET to produce photovoltage governing the channel conductivity. Note that a thin layer of metal (i.e., Al) is deposited on the n-CQD side of the photodiode and grounded to prevent electron accumulation at the n side under illumination. The thickness of the metal is set to be 20 nm, rendering it almost transparent to the incoming light.

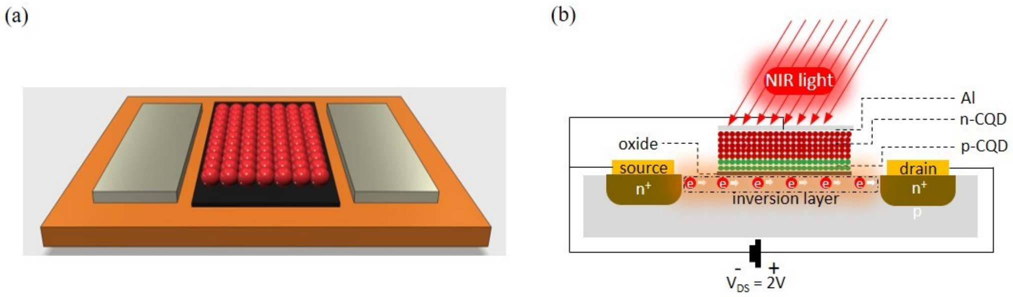

Figure 3.1. Structures of the POSFET. (a) 3D structure of the CQD POSFET. (b) Electrical circuits of the device. Reprinted with permission from [61]. Copyright © 2019 Optical Society of America.

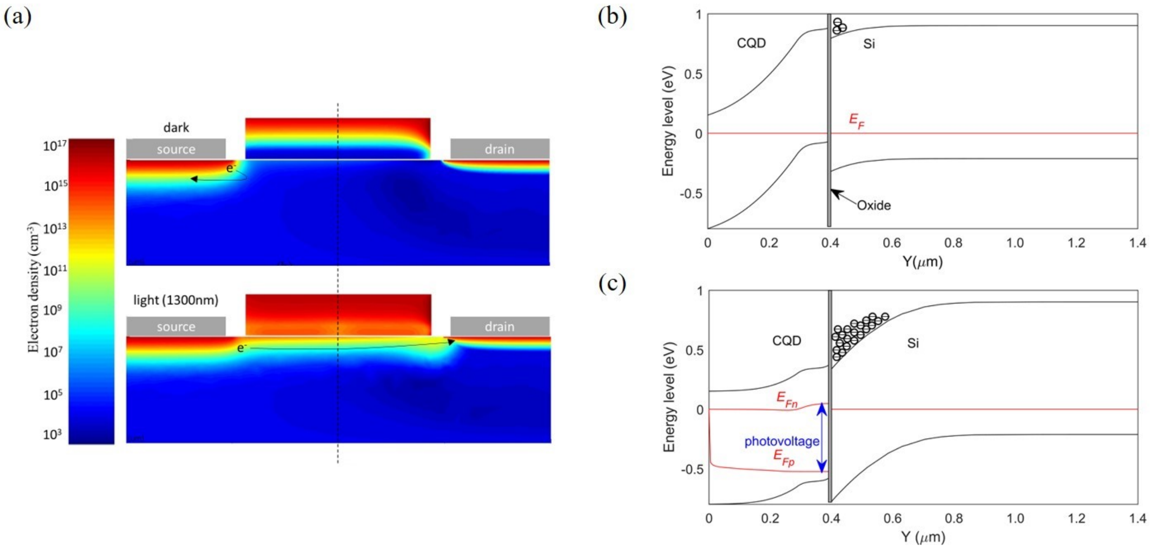

Figure 3.2. Working principles of the POSFET: (a) simulations of electron concentration profiles of the device in the dark and under infrared-light illumination; band diagrams of the POSFET in the (b)dark and (c)illumination. The diagrams were calculated along the central axis shown as dashed lines in (a). Reprinted with permission from [61]. Copyright © 2019 Optical Society of America.

Simulations were carried out using commercial software (Lumerical FDTD Solution and DEVICE) to demonstrate the physical principles of the POSFET. Figure 3.2a shows electron density profiles of the device in the dark (top) and under optical illumination (bottom). While without light electron transports are hindered as the silicon channel is depleted, an inversion layer appears at the oxide/semiconductor interface under optical irradiation (1300 nm), aiding electron transfers from source to drain side. In Figures 3.2b,c, band diagrams along the central axis, displayed as black dashed line in Figure 3.2a, were obtained from the simulations. In the dark (Figure 3.2b), only a few numbers of electrons exist at the interface. Under illumination (Figure 3.2c), a large number of electrons ($\sim 10^{13}$cm^{-3}) can accumulate due to downward bending of conduction band, thereby creating the inversion layer and an increased conductivity in the channel. To clarify the concept, we calculated electron density along the axis in Figure 3.3a. It was found that under optical illumination the charge density can be drastically enhanced by around five orders of magnitude at the interface. This photoresponse can be attributed to the photovoltage (defined as the separation between electron and hole quasi-Fermi levels) generated from the CQD photodiode. Finally, the potential barriers for electrons from source n^+ well to the oxide-semiconductor interface are much lowered by the photovoltage, rendering easier charge transports in the Si channel (see Figures 3.3 b,c).

Unlike the commercial germanium-on-silicon photodetector, the fabrication of the POSFET can be achieved under room temperature, making it fully compatible with today's CMOS technology. In addition, comparing with the PVFET structure, the POSFET architecture exhibits much lower gate leakage current, lower heat generation, and thus more stable device performance. The PVFET structure also requires a combination of process conditions and judicious choice of interface treatment chemicals in order to achieve a highly rectifying heterojunction between the CQD and silicon channel, that is an energy band alignment as well as a trap-free CQD/Si interface, whereas in the POSFET the aligned energy band is no longer required, giving more selections on the chemicals for CQD/oixde interface treatment.

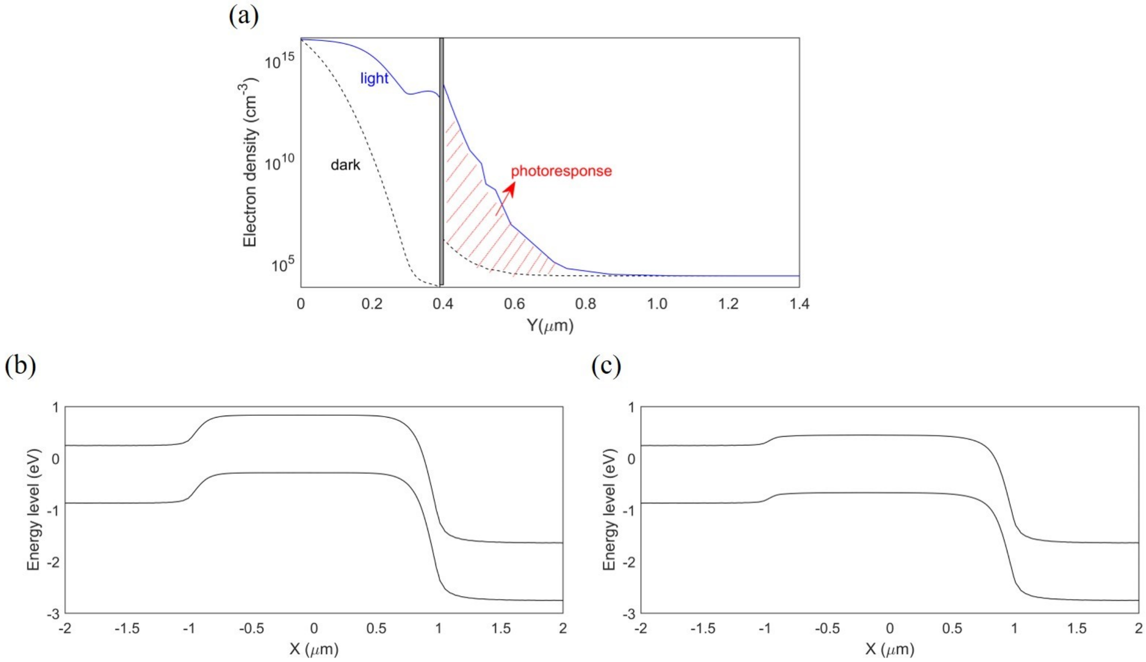

Figure 3.3. (a) Electron density in the dark and under illumination, determined along the central axis. Transverse potential distribution in the (b)dark and (c)illumination. Reprinted with permission from [61]. Copyright © 2019 Optical Society of America.

In order to prove the practical feasibility of the POSFET, we experimentally connected a CQD photodiode to a commercially available MOSFET (DN3525, MICROCHIP) as shown in Figure 3.4a. The CQDs were synthesized by solution-processed method and the photodiode was fabricated *via* simple spin coating as shown in the SEM image in Figure 3.4a. The photodiode was illuminated by NIR incident light through transparent ITO substrate. The MOSFET was biased with a Keithley 2400 Sourcemeter, with which the output current was measured. As intuitively expected, when light is biased on the CQD, an increase in source-drain current, photocurrent, was be observed.

We first determined the device performance by characterizing the responsivity as a function of light incident power. The results are shown in Figure 3.4b, demonstrating a downward trend in responsivity for increasing incident power. We then investigated the spectral responsivity of the device, along with the EQE of the utilized CQD photodiode, as displayed in Figure 3.4c. Comparing with a silicon-based photodetector, which barely produces photoresponse beyond silicon bandgap at 1100 nm, the device shows a highest responsivity of 5.9A/W at the exciton at wavelength of 1250 nm.

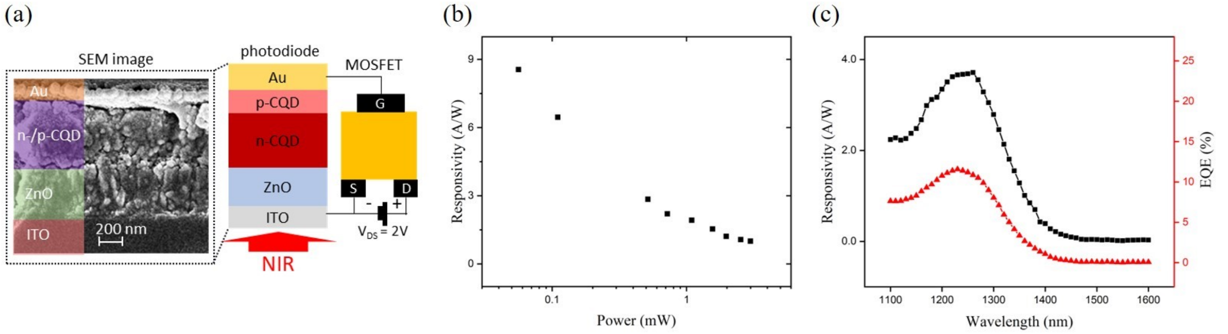

Figure 3.4. (a) Device configuration for proof of concept. (b) Spectral responsivity, along with EQE of the photodiode as a comparison. (c) Responsivity as a function of incident power. Reprinted with permission from [61]. Copyright © 2019 Optical Society of America.

3.4 Summary

In summary, the POSFET structure demonstrated in this chapter leverages the photovoltage effect provided by CQD photodiode and transconductance amplification produced by field-effect transistor located beneath. This design can benefit from minimized gate leakage current and lower requirement on interface treatment. As a result, the POSFET can have a high sensitivity, as it is reverse proportional to the noise current. Proof-of-principle has been demonstrated that the POSFET shows a highest responsivity of 5.9A/W at the wavelength of 1250 nm. Future development for the monolithic fabrication of CQD-NIR photodetector using CMOS technology will enable this class of devices for low cost NIR photodetectors in a wide range of applications.

4. Comparisons of on-chip Ge, InGaAs and colloidal quantum dot photodetectors in silicon photonics

4.1 Background

On-chip detection of light in silicon photonics enables a plethora of applications, mainly as receivers for optical communications [62]–[64], but also plays an important role as photodetectors for automotive LiDAR [65], [66] and chemical-/bio-sensing [67], [68]. The heteroepitaxy of Ge on silicon (Si) offers an easy and cost-effective solution that is CMOS-compatible and is by far the most mature device for this purpose. However, the greatest challenge for the integration of Ge on Si is large lattice mismatch (4.2%) between the two materials, which can cause significant issues, such as high density of threading dislocations that adversely affects device performance [4]. The previous two decades have witnessed tremendous efforts and rapid progresses in improving Ge photodetectors integrated on Si. It includes introducing graded SiGe buffer layer between Ge and Si [69], and a post-growth thermal annealing treatment [2]. Nowadays, the state-of-the-art Ge photodetectors with a bandwidth exceeding 40 GHz and a responsivity close to 1 A/W have been demonstrated [70], [71].

However, Ge photodetectors normally suffer from high dark current comparing with their conventional III/V counterparts. This poses great challenges for reducing detector noise and the whole power consumption of Si photonic integrated circuits. Method based on III/V-Si platform, therefore, comes in as an alternative. Taking InGaAs as a typical example, it is direct-bandgap semiconductor and has much larger absorption coefficient in the C-band than Ge. It leads to high-efficiency and fast InGaAs photodetector on Si with low dark current. Current technology realizing InGaAs-on-Si photodetector mainly involves wafer/die bonding [8], [9], transfer printing [6], [7] and heteroepitaxial growth [10], [11]. The first has stringent bonding requirement (wafer surface conditions, etc.) with low throughput while the second requires accurate alignment of discrete components. In contrast, heteroepitaxial growth provides a monolithic wafer-level integration solution. Efforts have been made to optimize buffer layers to achieve high-quality InGaAs epi-layers with a low defect density. Although the buffer layer for the InGaAs epi-layer has not reach same quality level as the mature Ge photodetectors [72]–[74], in this work, we intend to predict the performance of InGaAs-on-Si photodetectors fabricated *via* epitaxy technique when the buffer layer with the same quality as Ge photodetectors is developed in the future. On the other hand, near-infrared (NIR) photodetectors based on CQD/Si heterojunction have been recently demonstrated [34], [35], [75]. Unlike abovementioned methods, the on-Si CQD photodetector only requires room-temperature chemical surface treatment and an easy spin-coating process. This paves the way for low-cost CQD photodetectors integrated on Si for silicon photonics.

Nevertheless, no previous works have been reported comparing the effects of material properties on photodetector performance for the three materials. For example, InGaAs has much stronger absorption than Ge, and thus InGaAs photodetector with smaller area can have the same efficiency as Ge detector but with lower dark current and higher RF bandwidth (3dB cut-off frequency) due to area-related RC effect. Here we seek to utilize silicon photonics as a platform and comprehensively compare their performance of on-chip light detection. In this chapter, we take photodetectors that are integrated with waveguides as an example, examining their performance in C-band wavelengths. Figure-of-merits including responsivity, dark current and 3dB bandwidth are investigated.

4.2 Simulation method

Simulations were conducted using Lumerical FDTD and DEVICE suite. In the suite, FDTD is an electromagnetic simulator used to calculate the electric field coupled from Si to active layer and carrier generation induced by the light. The generation profile was then imported into CHARGE which is a charge transport simulator used to calculate photodetectors' electrical characteristics such as dark current and responsivity. The structure of on-Si photodetector is shown in Figure 4.1. The width (*w*) and thickness (*t*) of the layer are 8 μm and 500 nm for all the simulations, whereas the length (*l*) varies. The width and thickness values are referenced from published works [12], [76]–[78]. It also has been shown that the width of the active layer has little impact on photodetector efficiencies [12]. We chose 8-μm width and 500-nm thickness and vary the detector length to investigate photodetector performances. Note that for InGaAs photodetector, a thin buffer layer (130nm) was inserted between Si and InGaAs. This buffer layer with such thin thickness has not been realized but research efforts are being made to improve buffer layer quality including reducing its thickness. Here, we intend to predict its performance once the quality of InGaAs epi-layer has been optimized and compare it with that of mature Ge-on-Si technology. The material electrical properties for Ge and InGaAs are given by the software database. The properties for PbS CQDs are user-defined. All the necessary property parameters are listed in Table 4.1.

Three figure-of-merits are investigated for the devices, i.e., dark current, responsivity and 3dB bandwidth. The generated carriers under illumination will create current induced by voltage bias and the current was simulated by CHARGE simulator. Thus, responsivity values were obtained by Equation 1.1 (both generated current and input light power were already recorded by FDTD simulator). A wavelength dependent study (C-band wavelength) on responsivity was conducted, while for the rest of the study 1.55 μm was set as the targeting wavelength. 3dB bandwidth was calculated by considering transit bandwidth and RC bandwidth, as will be explained in detail in the later content.

Table 4.1. Material parameters used for the simulation of CQD photodetector.

Material electrical properties	Ge	InGaAs	CQD
Bandgap (eV)	0.66	0.74	0.80
Carrier mobility ($cm^2V^{-1}s^{-1}$)	3900(e)/1800(h)	4000(e)/490(h)	3.7 [79]
Carrier lifetime (s)	1.5×10^{-9}	1.0×10^{-10}	1×10^{-7} [80]
Dielectric constant	16	13.7	15.5 [47]
Electron effective mass	0.56	0.039	0.2 [81]
Hole effective mass	0.29	0.45	0.27 [81]
Refractive index	4.3	3.6	2.8

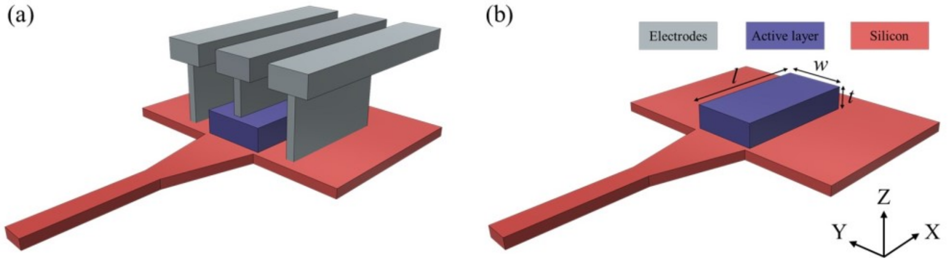

Figure 4.1. Schematic diagram of on-Si photodetectors: perspective views (a) with metal electrodes and (b) without electrodes presented. Reprinted with permission from [82]. Copyright © 2021 Optical Society of America.

4.3 Simulation results and discussions

As displayed in Figure 4.2, the simulated electric fields under illumination from FDTD simulator clearly show the light coupling from Si to active layers and the intensity attenuation caused by active layer absorption. Interestingly, due to Ge's low absorption, the light cannot be fully absorbed at the end for a 10 µm long photodetector. This is in drastic contrast to both InGaAs and CQD photodetectors, in which most of the light is absorbed within 5 µm distance. This means for both photodetectors the detector length can be shortened while maintain same efficiency levels; shorter lengths lead to low dark current and higher speed bandwidth.

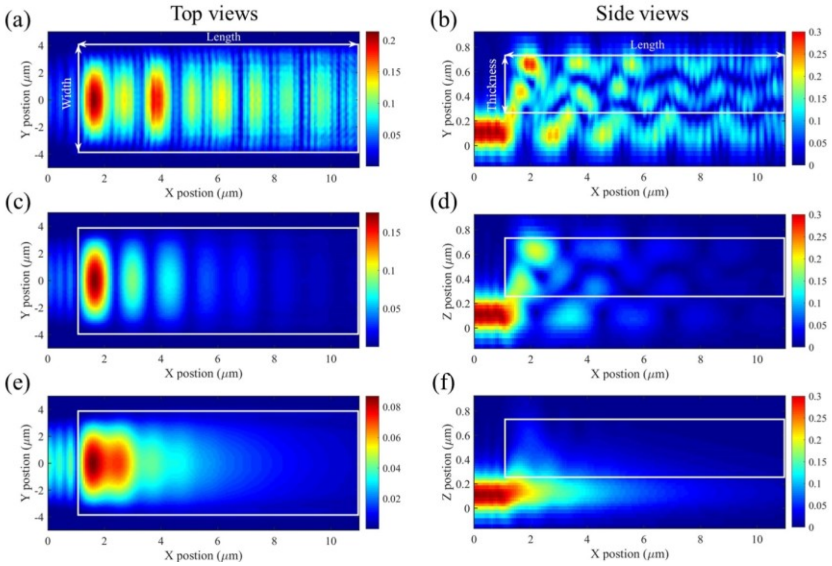

Figure 4.2. Electric field simulated by FDTD simulator demonstrating light coupling from Si to active layers for (a)(b) Ge photodetector, (c)(d) InGaAs photodetector and (e)(f) CQD photodetector. Active layers are indicated by the white box. The left column shows top views, and the right column shows side views. Reprinted with permission from [82]. Copyright © 2021 Optical Society of America.

Comparing with Ge, InGaAs and CQD have much lower intrinsic carrier concentrations (~10^{11} cm^{-3} as opposed to ~10^{13} cm^{-3}). According to Shockley diode equation, reverse saturation current is proportional to the square of the intrinsic concentration. Thus, we sought to first investigate the effect on their device dark current. Figure 4.3a shows the dark current for the photodetectors with different lengths of active layer at 2 V reverse bias at 300K. As expected, both InGaAs and CQD photodetectors have much lower dark current than Ge detector for all lengths. As shown in the inset plot in linear scale, the dark current varies linearly with device length as it is dominated by bulk current (only the dark current for Ge photodetector is displayed). The simulated dark current for Ge photodetector in this work matches well with both the published simulation and experimental results [12]. For example, experimental dark current reported in Ref. 12 were 4.4-9.3 μA for the lengths of 15-25 μm (the width for the experimental devices is 8 μm, the same in this study). It is also noticed that the CQD photodetector exhibits even lower dark current than InGaAs photodetector at an order of nanoampere. This is due to CQD's low carrier mobility compared with crystalline semiconductors, leading to lower carrier diffusivity and thus smaller reverse saturation current, according to Shockley diode equation. A temperature dependent study on dark current was conducted and is shown in Figure 4.3b. Dark currents for all three devices increase as temperature increases. More importantly, in our simulation results for Ge photodetector, the dark current increases by a factor of 1.6-2.0 every 10K, which match well with reported experimental results [83], [84].

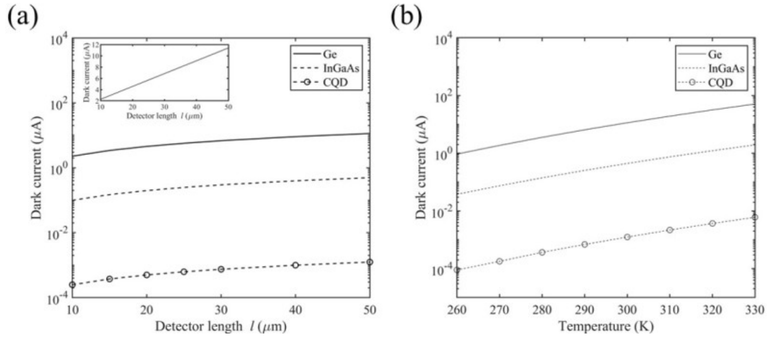

Figure 4.3. Dark current of photodetectors for different (a) lengths at 300K and (b) temperatures at 50 μm. Reprinted with permission from [82]. Copyright © 2021 Optical Society of America.

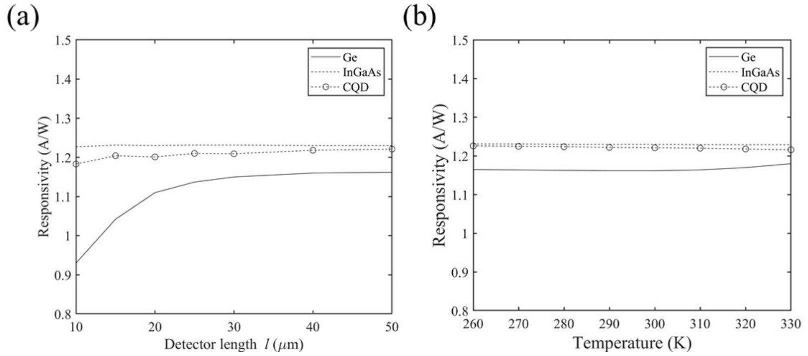

Figure 4.4. Responsivity of photodetectors for different (a) lengths at 300K and (b) temperatures at 50 μm. Reprinted with permission from [82]. Copyright © 2021 Optical Society of America.

Considering the superior absorption capability of InGaAs and CQD with absorption coefficients at 1.55 μm of 9600 cm^{-1} [85] and 2×10^4 cm^{-1} [86], as opposed to 1800 cm^{-1} for Ge [12], it is worth comparing photodetector responsivity for the three materials, which can be observed in Figure 4.4. Note that the absorption coefficient utilized in this study is for Ge thin film epitaxially grown on Si at low temperature. However, the coefficient highly depends on the process conditions. For example, a coefficient of 3000 cm^{-1} at 1550 nm has been reported for 0.25% tensile strained Ge

[87]. Here, by utilizing 1800 cm^{-1}, a direct comparison is demonstrated here to compare our simulation results and that in the reference work. Figure 4.4a shows a gradual increase in responsivity for Ge detector as detector length increases, due to its insufficient absorption at shorter detector length. The trend as well as the responsivity values are similar to the published simulation results [12]. However, the simulated responsivity values are higher than most published experimental results (<1 A/W for experimental devices). This is because the simulation neglects contact resistance which will be discussed in RF bandwidth calculation. In comparison, InGaAs and CQD photodetectors exhibit a ‘saturation’ in responsivity values at all lengths in Figure 4.4a. This is because almost all the light can be absorbed within 10 μm detector length (see the electric field simulation in Figure 4.2). Note that for InGaAs photodetector, achieving a thin buffer layer is crucial for constructing a highly efficient device. It is estimated that for a 10-μm-long InGaAs photodetector the buffer layer must be thinner than 250 nm to exceed Ge photodetector’s responsivity at the same length. This is because thicker buffer layer dramatically reduces light coupling into InGaAs active layer. From Figure 4.4a, a conclusion can be drawn that both InGaAs and CQD photodetectors are able to maintain a high responsivity with a small detector size, leading to a smaller RC time constant and thus a faster speed. To this end, we will investigate RF bandwidth in the following. In Figure 4.4b, it can be concluded that unlike dark current which increases with higher temperature responsivity values are, however, stable with temperature.

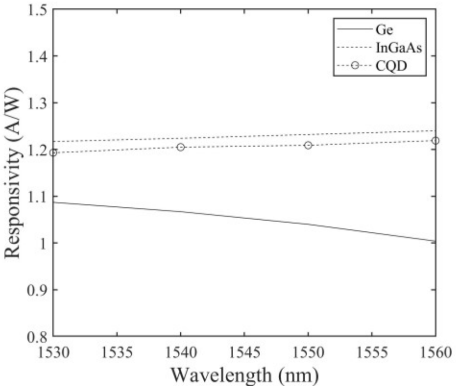

Figure 4.5. Responsivity of 15-μm-long photodetectors for different C-band wavelengths. Reprinted with permission from [82]. Copyright © 2021 Optical Society of America.

A wavelength dependent study on responsivity was then conducted, and results are illustrated in Figure 4.5. The wavelength range is chosen in C-band wavelength (1530-1560 nm). Ge photodetector shows a decreasing trend in responsivity value while InGaAs and CQD photodetectors maintain the values due to their strong absorption across C-band wavelengths.

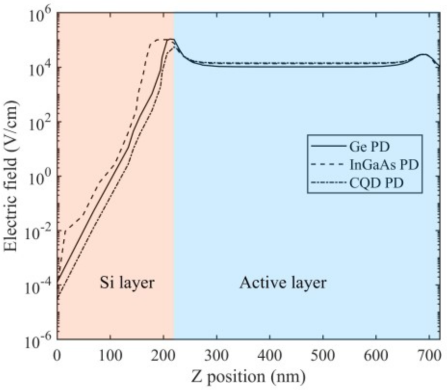

Figure 4.6. Electric field distributions for three devices under 2 V reverse bias along Z-direction. Reprinted with permission from [82]. Copyright © 2021 Optical Society of America.

At reverse bias, diffusion can be neglected, and one only needs to consider transit time and RC delay for the RF bandwidth. This can be seen in Figure 4.6, in which electric field distributions are illustrated, which proves all the devices are operated without diffusion under reverse bias condition. Transit time is the time it takes the carriers to move across the active region. This leads to carrier transit frequency, which follows [88]

$$f_{\mathrm{tr}}=\frac{\sqrt{2}}{\pi}\frac{1}{t_{\mathrm{tr}}} \tag{4.1}$$

where t_{tr} is the transit time. With the CHARGE simulator, we conducted a transient simulation to extract carrier transit time. The principle is shown in Figure 4.7, which shows the front view of a photodetector. Within the simulation region, a carrier generation profile imported from FDTD is positioned at top edge of active layer. A global shutter is kept closed until $t_0 = 0.5$ ps, after which it opens to light and photocarriers are induced. Three current flux monitors are positioned as shown which observe the dynamic movement of generated photocarrier under electric field. Results are shown in Figure 4.8. The figure illustrates the propagation of current pulse through the three monitors consecutively. At the time current pulse reaches monitor 3 (t_{m3}), the pulse has traveled the entire active layer, and thus carrier transit time is obtained as $t_{\mathrm{tr}} = t_{\mathrm{m3}} - t_0$. The electric field in active layer is calculated to be $> 1\times10^4$ V/cm (see Figure 4.6). At such high field, drift velocity reaches saturation velocity for both Ge and InGaAs photodetectors. Ge's saturation velocity (5.4×10^6 cm/s) is slightly lower than InGaAs's (7.7×10^6 cm/s), leading to larger transit time (see Figures 4.8a,b). In contrast, CQD photodetector in Figure 8c has a drastic larger transit time due to its small carrier mobility.

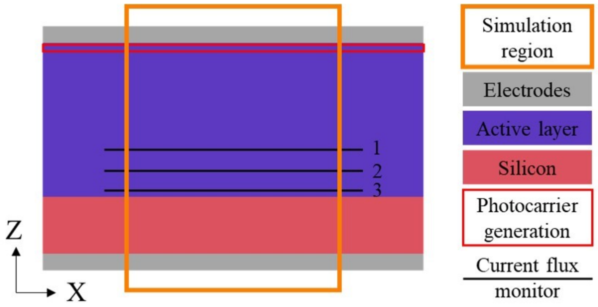

Figure 4.7. Schematic showing the principle of transient simulation. Reprinted with permission from [82]. Copyright © 2021 Optical Society of America.

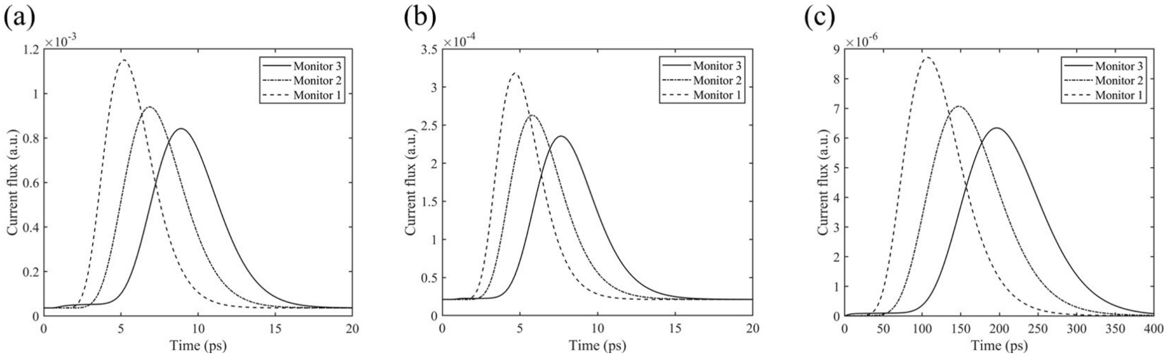

Figure 4.8. Pulses depicting current flux propagation in (a) Ge, (b) InGaAs and (c) CQD photodetectors. Reprinted with permission from [82]. Copyright © 2021 Optical Society of America.

Other than transit time frequency, RC bandwidth f_{RC} is another limitation of RF bandwidth, and follows [88]

$$f_{\mathrm{RC}}=\frac{1}{2\pi RC} \tag{4.2}$$

In the equation, the overall capacitance C is dominated by the depletion region. *Via* the CHARGE simulator, we performed a small-signal ac (SSAC) simulation to calculate the overall capacitance of the photodetectors. In this simulation, a dc voltage is applied to set the photodetector at reverse bias condition. Meantime, a small ac signal of 0.001V is applied and the resulting ac current is collected. According to the diode model, the admittance function can be written and simplified as

$$Y(\omega)=\frac{i}{v}=(R_{\mathrm{S}}+\frac{1}{j\omega C})^{-1}\approx j\omega C \tag{4.3}$$

under the condition of $R_{\mathrm{S}} \approx 0$. R_{S} is series resistance and is negelected due to that in the SSAC simulation the ac current is extracted without considering contact resistance. With this equation and the extracted ac current, one can calculate the capacitance as a function of frequency, as illustrated in Figure 4.9. Different capacitance values are observed mainly due to materials' different dielectric constants. Other than the depletion region capacitance, one capacitance neglected in the SSAC simulation is the parasitic capacitance between doped silicon and conductive substrate. Taking the thickness of buried oxide as 2 μm, it can contribute a parallel plate capacitance estimated of 0.017 fF/μm^2.

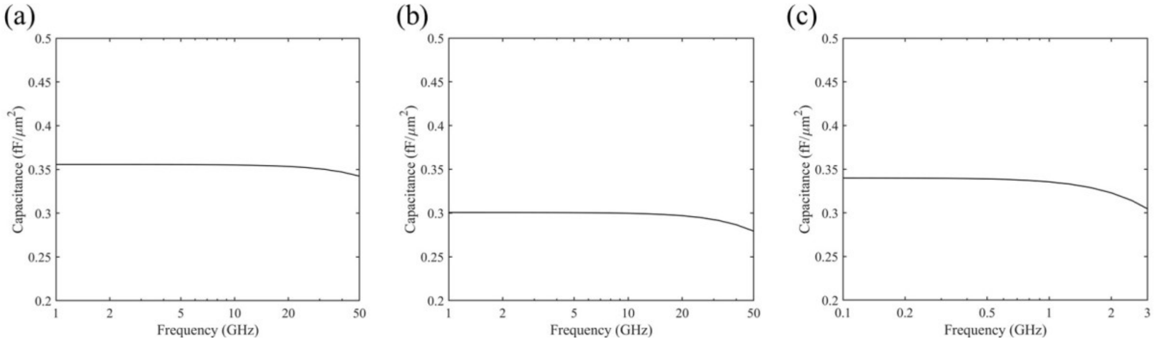

Figure 4.9. Capacitance extracted by SSAC simulation for (a) Ge, (b) InGaAs and (c) CQD photodetectors. Reprinted with permission from [82]. Copyright © 2021 Optical Society of America.

The resistance R in Equation. 4.2 is the sum of series resistance R_S and load resistance R_L. R_S comprises contact resistance and resistance from diffusion region which equals to zero under fully depletion condition at reverse bias. In this case, resistance R follows

$$R=R_L+R_S=R_L+\frac{\rho}{A} \tag{4.4}$$

where ρ is the resistivity of contact surface and A is the surface area.

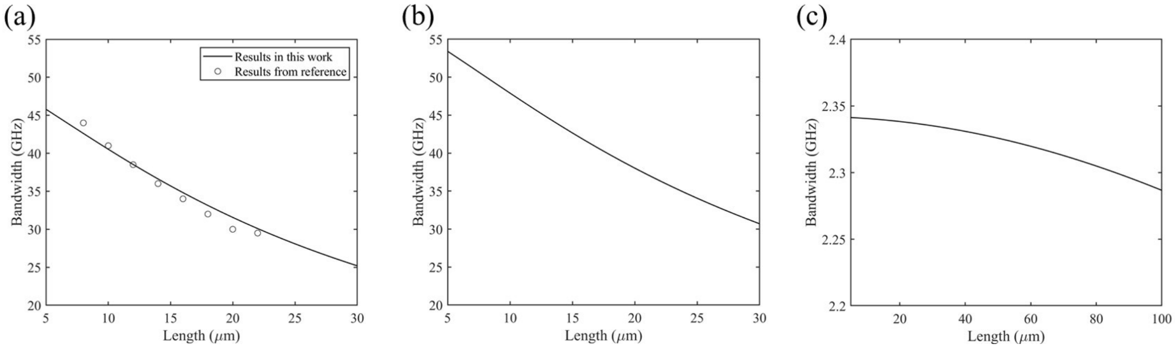

Figure 4.10. RF bandwidth for (a) Ge, (b) InGaAs and (c) CQD photodetectors of different lengths. Data in (a) is adapted from Ref. 12. Reprinted with permission from [82]. Copyright © 2021 Optical Society of America.

Finally, to calculate the RF bandwidth we utilize the equation below to include both transit time and RC limitation [88]:

$$f_{3\mathrm{dB}}=\frac{1}{\sqrt{\frac{1}{f_{\mathrm{tr}}^{2}}+\frac{1}{f_{\mathrm{RC}}^{2}}}}$$

(4.5)

From Equations 4.1-4.5, we obtain the RF bandwidth as a function of detector length, as displayed in Figure 4.10. Notably, the bandwidth simulation values for Ge photodetectors match well with the published simulation results [12]. Based on the results obtained above, we draw our main conclusions. With the premise that buffer layer will be optimized in the near future as the mature Ge-on-Si technology, the InGaAs photodetector surely possesses advantages over the Ge photodetector. Its dark current and thus the power consumption is much lower than the Ge photodetector. More importantly, to maintain a high responsivity close to 1.2 A/W, InGaAs photodetector's length can be as short as 10 μm, which corresponds to a RF bandwidth of > 45 GHz, while Ge photodetector have to have 30 μm long with a RF bandwidth of 25 GHz. In other words, the InGaAs photodetector has higher bandwidth & responsivity product than the Ge photodetector under the same detector design. As for the case of CQD photodetector, it exhibits high efficiency and ultralow dark current, rendering it well suited for applications where sensitive and low noise detection is required, such as in the science of quantum information. The bandwidth is, however, much lower than both Ge and InGaAs photodetectors due to the low carrier mobility. The low mobility results in a transit-time-limited bandwidth for all simulated lengths. Nevertheless, the speed suffices for medium speed applications, e.g. NIR image sensors [32]. Especially, considering its easy and low-cost processing, CQD photodetector can be potentially more favorable towards these applications than Ge and InGaAs photodetectors.

4.4 Summary

Three materials are compared for photodetection in Si photonics. Based on the simulation results obtained, InGaAs is the best material for ultrafast on-chip light detection provided that the InGaAs epi-layer on Si can be optimized. Comparing with mature Ge photodetector technology, InGaAs photodetector can potentially have higher efficiency, lower dark current and faster speed. CQD photodetector has the lowest dark current, raising extreme interests for applications in which ultralow noise is required. The RF speed is the slowest, but it suffices for certain applications. Considering its low cost and ease of fabrication, it could be more suitable than both Ge and InGaAs. As the CQD mobility continues to rise, the CQD on-Si photodetector will possibly be comparable to the counterparts fabricated from crystalline semiconductors.

5. Silicon surface passivation for colloidal quantum dot/silicon heterojunction photodiode

5.1 Background

CQD/Si rectifying junctions were first presented in two successive works in 2011 that pointed to the potential of these structures [89], [90]; unfortunately, neither exhibited appreciable charge extraction under illumination when exposed to incident light of wavelengths exceeding 1100 nm. In 2015, Sargent's group successfully demonstrated a CQD/Si junction that effectively extracted photogenerated charges under 1200 nm illumination [34]. Through judicious tailoring of the CQD/Si interface *via* a one-step methyl iodide (CH_3I) functionalization, passivation of interface defects and favorable band alignment between the two materials were simultaneously achieved and an external quantum efficiency (EQE) of 14% at the exciton peak was realized at short circuit condition and 33% at -7 V voltage bias. More recently, an alternative passivation strategy employing zinc oxide (ZnO) nanoparticles provided 18% EQE at 0 V bias [75]. In 2020, Ning's group demonstrated an inverted-structure heterojunction which possessed lower energy band offset that provided a better charge extraction [35]. The inverted structure using the same one-step CH_3I passivation produced a higher excitonic EQE of 21% at short circuit condition. However, the efficiency is still low, which we believe is due to incomplete and inefficient passivation of the Si surface.

To date, the general two-step chlorination/alkylation method has been widely employed in previous studies for efficient Si surface passivation and provides up to 100% of coverage on Si surface [91]–[93]. The resulting methylated Si surface slows surface recombination velocity down to < 30 cm/s [94], [95]. Comparing to other methods using insulating oxides[96]–[99] or bulky organic molecules [100]–[102], this method is also less prone to hinder charge transport in a heterojunction, thanks to methyl group's exceedingly small van der Waals diameter. To this end, this chapter will present a comparative study of the performance of CQD/Si heterojunctions using Si substrates functionalized based upon two complementary passivation strategies – one-step CH_3I passivation and two-step chlorination/methylation process. Through the study, we have demonstrated the importance of efficient Si surface passivation for achieving high-performance CQD/Si heterojunctions and therefore highly efficient CQD/Si photodetectors. Our CQD/Si photodetector achieve 31% of EQE at excitonic peak at -4V bias, nearly two-fold enhancement compared to the standard device (16%) passivated by CH_3I. The high efficiency leads to a detectivity of 8.8×10^{10} jones.

5.2 Methods

PbS CQD synthesis: PbS CQDs were synthesized according to the method in Section 2.2.

Synthesis of ZnO nanocrystals: ZnO nanocrystals were synthesized as previously reported. [45] Zinc acetate dihydrate (Zn(Ac)2·2H2O; 2.96 g; 13.5 mmoles) and methanol (125 mL; Fisher Scientific, Certified ACS Reagent) are combined in a three-neck flask. The mixture was stirred and heated at 60 ˚C using a heating mantle. Then potassium hydroxide (KOH; 1.518 g; 27 mmoles) dissolved in methanol (65 mL) was slowly injected into the three-neck flask and the solution was kept heating at 60 ˚C for 2.5 h. After cooldown, the ZnO nanocrystals were extracted by centrifuge (4000 rpm for 5 min) and washed by methanol (30 mL) followed by centrifuge. This process was repeated twice before dissolving ZnO nanocrystals in methanol/ chloroform (10 mL/ 10 mL).

Device fabrication: A PbS CQD layer was deposited onto the functionalized silicon substrate of choice *via* a layer-by-layer method under air-ambient conditions [103]. Briefly, an octane solution of PbS CQD (30 μL; 50 mg/mL) was placed on the Si substrate and was spun at 2500 rpm for 20 s. Subsequently, a methanol solution of tetrabutylammonium iodide (TBAI; 10 mg/mL) was placed on the whole substrate where it remained for ca. 30 s to promote ligand exchange followed by being spun at 2500 rpm to remove excess solution followed by acetonitrile rinsing twice. This layer-by-layer process was repeated 10 times (10 layers) to reach desired film thickness. Then two layers of ZnO were deposited by dropping methanol/chloroform solution of ZnO nanocrystal (100 μL) and spin-coated at 5000 rpm for 30 s. Finally, ITO (150 nm) was deposited *via* magnetron sputtering.

X-ray photoelectron spectroscopy measurements: The measurements were conducted with a Kratos Axis 165 Ultra X-ray photoelectron spectrometer, in which a 210 W monochromatic Al Kα source with an energy $\hbar\nu = 1486.6$ eV was used. Survey spectra measurements were performed with an analyzer pass energy of 160 eV and a step size of 0.3 eV. High-resolution spectra were collected with an analyzer pass energy of 20 eV and a step size of 0.1 eV. All spectra were calibrated based upon C 1s (284.4eV) and fitted using CasaXPS software. A Shirley background was subtracted from the spectra for peak fitting.

Device characterizations: I-V curves were measured using a Keithley 2400 source meter. A narrowband LED source (centered at 1300 nm; Luxmux ISB2) was used as light source for light I-V measurement. TPV and TPC measurements were conducted as described in the methods in Section 2.2.

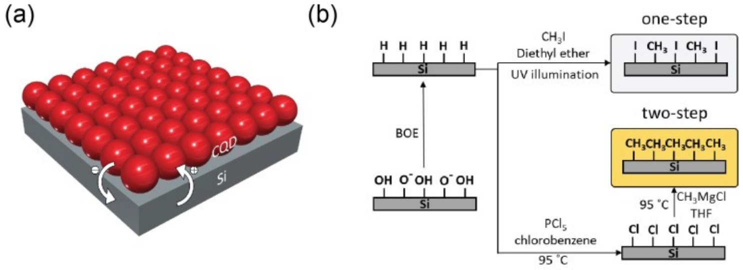

Figure 5.1 (a) Schematics showing charge transfers between Si:CQD heterojunction. (b) Passivation processes for CH_3I passivation (denoted as one-step) and two-step chlorination/methylation treatment (denoted as two-step). Reprinted with permission from [104]. Copyright © 2021, American Chemical Society.

5.3 Results and discussions

All Si substrates used in the presented study were cleaned and etched to remove the thin layer of surface native oxide. Surface passivation is crucial for reducing charge recombination at Si surface and promoting charge transport at the CQD/Si interface (Figure 5.1a). Two passivation strategies are investigated in this study, one-step CH_3I passivation (denoted as one-step) and two-step chlorination/methylation treatment (denoted as two-step), as illustrated in Figure 5.1b. The one-step treatment is served as the standard method which has been utilized in previous studies for interface treatment for a CQD/Si photodiode [34], [35]. UV illumination is used for C-I bond dissociation. Then both iodine and methyl radicals are absorbed by the Si surface. Whereas the two-step treatment involves the first chlorination step by phosphorus pentachloride (PCl_5) in a radical reaction followed by methylation with a Grignard reagent. Note that a direct methylation step without prior chlorination does not produce a Si surface that is structurally and chemically defined with a high degree of coverage.

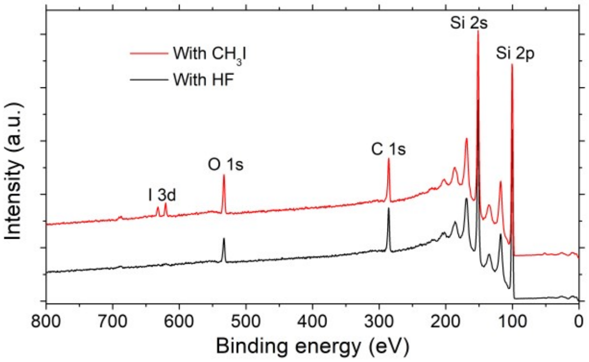

Figure 5.2. Survey XP spectra of CH_3I passivated Si surface and freshly etched Si displayed as comparison. Reprinted with permission from [104]. Copyright © 2021, American Chemical Society.

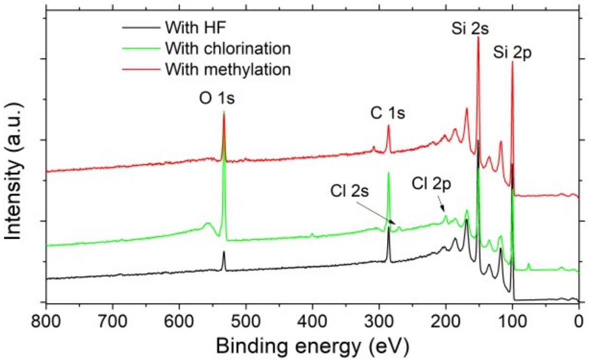

Figure 5.3. Survey XP spectra of Cl- and CH_3- terminated Si surface and freshly etched Si displayed as comparison. Cl 2s and 2p peaks appear only after chlorination step and disappear after methylation step, indicating complete removal of the bonds. Reprinted with permission from [104]. Copyright © 2021, American Chemical Society.

After the Si surface is chemically treated. We first conduct X-ray photoelectron spectroscopy (XPS) measurements. For one-step passivated Si surface, the I 3d signal in survey-scan XPS (Figure 5.2) clearly indicates the absorption of iodine on Si surface. For the two-step method, the survey spectra

(Figure 5.3) show the appearance of Cl-terminated Si only after chlorination step. It disappears after methylation step, indicating complete removal of Si-Cl bond with the Grignard. Figure 5.4 shows high-resolution XPS spectrum of C 1s region. While the spectrum for one-step-passivated Si surface (Figure 5.4a) shows negligible difference with the freshly etched Si surface, C 1s emission region is evidently broadened for Si surface treated with two-step method (Figure 5.4b), which can only be fitted by introducing a new fitted peak at 283.4 eV [105], [106]. This new peak to methylated Si is due to the emission Si-C covalent bond. Such peak does not exist for chlorinated Si, meaning Si-C bond is introduced only at the second methylation step.

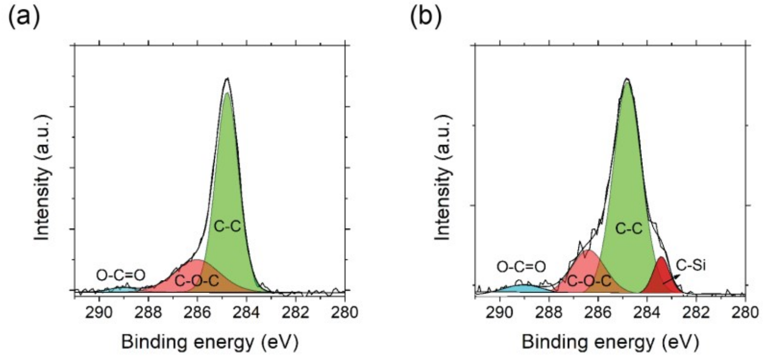

Figure 5.4. High-resolution XP spectra of C 1s region for: (a) One-step CH_3I passivated, (b) two-step treated Si surface and (c) chlorinated Si surface. Reprinted with permission from [104]. Copyright © 2021, American Chemical Society.

With the well-passivated Si surface, we then proceed to build CQD/Si heterojunction photodiodes. The PbS CQDs are synthesized *via* a hot-injection method according to previous reports [47] (also see the methods in Section 2.2). The absorption spectrum of the PbS CQD in Figure 5.5a shows an exciton peak at 1290 nm. Schematics of the photodiode structure is illustrated in Figure 5.5b. The CQD layer is spin-coated onto pretreated *p*-type Si surface *via* a layer-by-layer fashion [103] (see methods in Section 2.2). A layer of ZnO nanoparticles is deposited on top of CQD to block hole back-injection (Figure 5.5c). A layer of ITO is then sputtered as the top transparent contact. The dark current-voltage (I-V) curve is displayed in Figure 5.5d, which demonstrates a rectifying junction formed between CQD and Si.

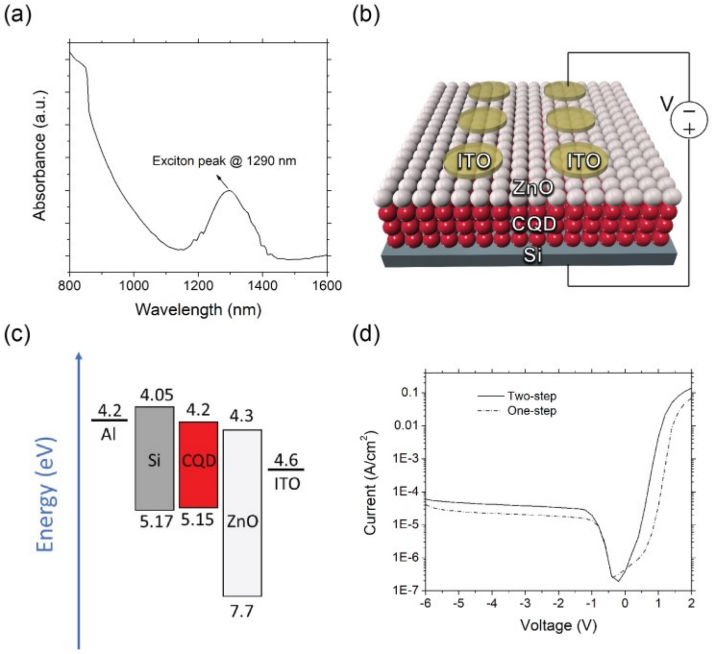

Figure 5.5. (a) Absorption spectrum of synthesized PbS CQD in octane solution. (b) NIR heterojunction photodiode architecture. (c) Band structure diagram. (d) Dark I-V curve of CQD/Si photodiode, showing a rectifying junction. Reprinted with permission from [104]. Copyright © 2021, American Chemical Society.

We then shine a narrowband light centered at 1300 nm using a light-emitting diode (LED) and measure I-V characteristics as shown in Figure 5.6. The figure shows that at reverse biased condition photodiode treated with two-step method extracts more photocarriers than the standard devices. Note that the spot size of light source is smaller than device active area.

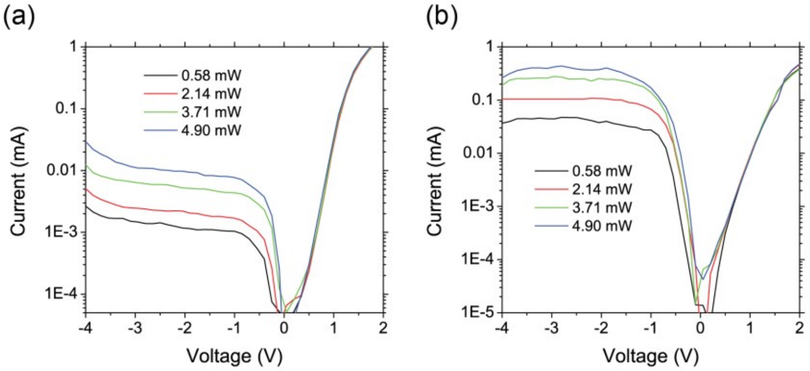

Figure 5.6. I-V characteristics under 1300-nm illumination for devices treated with (a) one-step method and (b) two-step method. Reprinted with permission from [104]. Copyright © 2021, American Chemical Society.

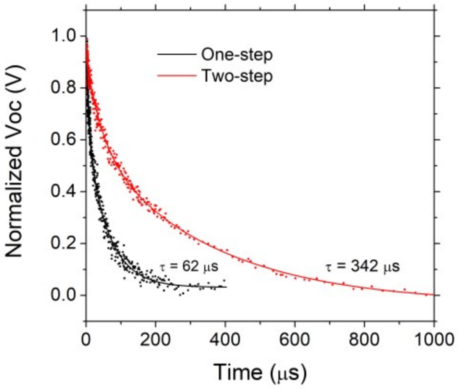

Figure 5.7. Transient photovoltage decay measurement of the CQD/Si photodiode. Reprinted with permission from [104]. Copyright © 2021, American Chemical Society.

TPV decay measurement is commonly used to analyze charge-carrier recombination in organic solar cells [107]–[110]. Lifetimes derived from TPV measurement are closely related to steady-state charge-carrier lifetimes [111], [112]. In Figures 5.7, TPV measurement shows that CQD/Si photodiode passivated by the two-step method exhibits much longer photovoltage decay lifetime comparing to one-step treated photodiode. This means photodiodes treated with two-step method feature longer charrier lifetime and thus lower defect concentration. Since the only difference is interface treatment, it indicates the two-step method passivates Si surface more effectively than the standard one-step method. This conclusion is cross-confirmed by TPC measurement as discussed below.

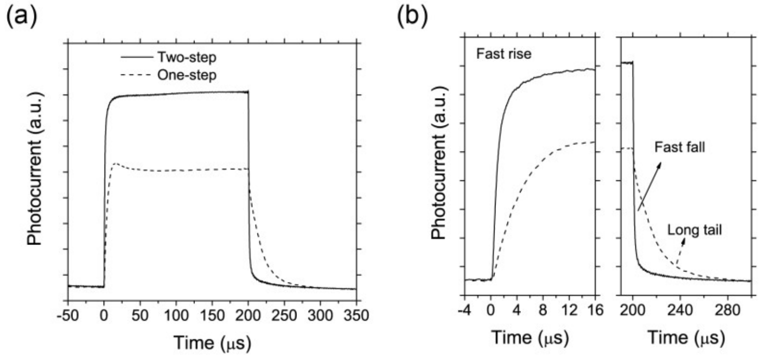

Figure 5.8 (a) TPC measurement showing rise and fall edges. Devices are bias at -2 V. (b) Zoom-in images showing fast rise and fall edges. Fall edge of standard device features much longer tail than two-step passivated device. Reprinted with permission from [104]. Copyright © 2021, American Chemical Society.

To characterize CQD/Si photodiode temporal response, TPC measurements are conducted and displayed in Figures 5.8, which present the photodiode response to illumination of a 200-μs white-light square pulse with no background light. Results show fast signal rises of 2.5 μs and 6.6 μs for two-step treated and standard devices, respectively, at -2 V bias. A slower rise time for standard device is associated with the trapping effect, in which the generated carrier charges after turn-on are quickly captured by the traps [113]–[115], making the photocurrent dynamic slower to reach the steady state. The effect is more significant when light is shut off. Subsequent to light-off, the captured charges are released by traps; yet the process is much slower than the quick buildup of trapped carriers [113]. The slow detrapping leads to a long-tail in fall-time edge as evident in the Figure (~ 40 μs). Thus, standard device possesses more interface traps than our proposed photodiode, consistent with the conclusion obtained from TPV measurement.

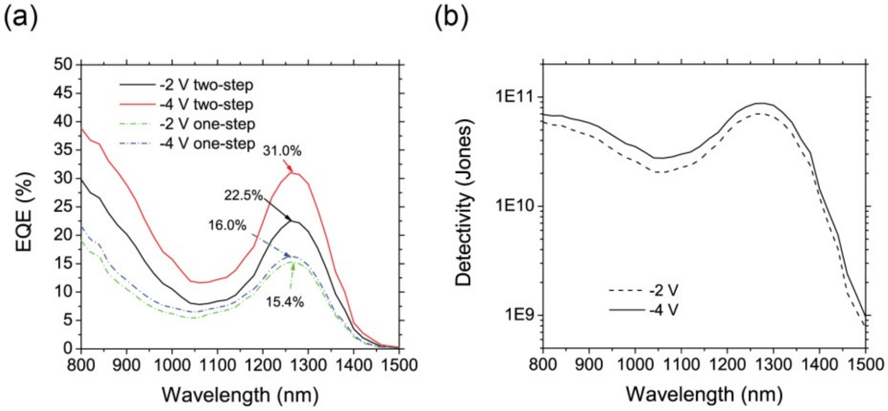

Figure 5.9. (a) EQE spectra showing CH_3I and two-step method treated CQD/Si photodiode at -2 and -4 V. (b) Detectivity spectra of CQD/Si photodiode under -2 and -4 V. Reprinted with permission from [104]. Copyright © 2021, American Chemical Society.

High-quality CQD/Si heterojunction also leads to high EQE values as displayed in Figure 5.9(a). Standard photodiode shows low EQE values due to insufficient interface passivation. The best device has only 15.4% at -2 V and a slight increase to 16% at -4 V at excitonic wavelength. In contrast, photodiode treated with two-step process exhibits higher EQE value. The best device features 25.2% at -2 V and a large enhancement to 31.0% at -4 V at exciton peak, nearly two-fold improvement comparing to standard device under same conditions. This improvement further validates the importance and effectiveness of efficient CQD/Si interface passivation. Figure 6(b) demonstrates the spectral detectivity data calculated *via* [34]:

$$D^{*} = R\sqrt{\frac{A}{2qI_{dark}}} = \frac{\mathrm{EQE}_{\lambda} q\lambda}{hc}\sqrt{\frac{A}{2qI_{dark}}} \tag{5.1}$$

The equation could also be deducted from Equations 1.3, 1.4, 2.12, where R is the responsivity, EQE_{λ} is spectral EQE values, λ is the wavelength, A is the area of active device (0.09 mm^2), q is the electron charge, h is the Planks constant, c is the speed of light, and I_{dark} is the dark current. A detectivity value of 8.8 × 10^{10} jones (1280 m) was obtained at -4 V bias. The device also demonstrates strong stability as it can maintain ~ 90% of its EQE value after 16 days (Figure 5.10). This can be attributed to superior air-stability of CQD/Si interface treated with two-step functionalization as discussed elsewhere [95], [116], [117].

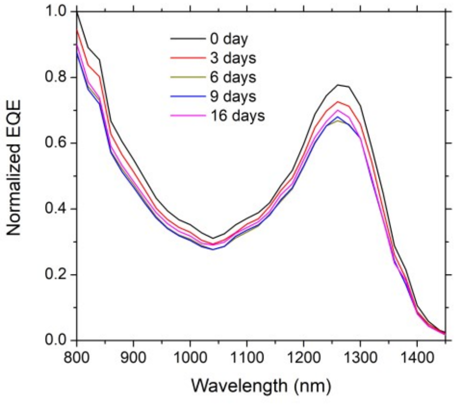

Figure 5.10. Device stability showing progressive degradation of the device in the air-ambient conditions. After day 9, device performance stabilizes and maintain 90% of EQE value at exciton peak at 1280 nm. Reprinted with permission from [104]. Copyright © 2021, American Chemical Society.

5.4 Summary

This chapter presented a high-quality CQD/Si heterojunction using a two-step chlorination/methylation treatment. TPV and TPC techniques validate that two-step method effectively reduces recombination rates and passivates interface traps. Finally, we have built a CQD/Si photodiode, which has a EQE value of 31% at 1280 nm at -4 V bias, comparing to only 16% for a standard CQD/Si photodiode. Less trap states also enhance response speed of the photodiode. Our device exhibits fast rise/fall times of 2.5/3.3 μs whereas the standard device has sluggish long tail of ~ 40 μs in the fall edge.

6. Colloidal quantum dot inks/silicon heterojunction photodiode

6.1 Backgrounds

As discussed in the previous chapter, two-step chlorination/methylation treatment method effectively passivate Si surface and CQD/Si interface was shown to exhibit lower trap-state densities and recombination rates compared to that passivated by one-step CH_3I, which was commonly employed in the previous CQD/Si heterojunction photodiodes. Yet all previously presented CQD/Si heterojunction photodiodes employed CQDs with ligands exchanged *via* a layer-by-layer solid-state protocol. Nevertheless, the CQD Inks passivated by lead halides obtained from a solution-phase ligand exchange yielded the best-performance photovoltaic devices to date, owing to the flattened energy landscape, lower defect concentration, improved carrier transport in the CQD Ink solids [118]–[122]. In addition, this straightforward and one-step spin-coating process reduces fabrication complexity and lowers material waste, making it an attractive alternative for scalable manufacturing. Herein, we integrate PbS CQD Inks on Si and constructed a broadband NIR CQD-Ink/Si heterojunction photodiode which oprates from 800 to up to 1500 nm. Well-passivated Si surfaces and high-quality CQD Ink films have afforded a low density of trap states. Built-in electric field is effectively enhanced by an insertion layer of *p*-type CQDs capped with EDT ligands in between Si and CQD Ink layer, leading to improved photocarrier extraction. Finally, an excitonic EQE of 44% at 1280 nm under 2 V reverse bias is obtained for the heterojunction photodiode. The photodiode also features high speed owing to the mechanism of fast charge-carrier separation under illumination, with rise and fall times lower than 4 μs.

6.2 Methods

Synthesis of PbS CQDs: Synthesis protocols are described in Section 2.2.

Synthesis of ZnO nanoparticles: ZnO nanoparticles were prepared as described in Section 5.2.

Si surface passivation: Si surface was passivated as described in Section 5.2.

Preparation of CQD inks: CQD Inks were prepared through a solution-phase exchange protocol. Lead halides consisting of lead iodide (0.23 mg; 0.5 mmol; Sigma-Aldrich) and lead bromide (0.037 mg; 0.11 mmol; Sigma-Aldrich), and ammonium acetate (0.015 mg; 0.21 mmol; Fisher Scientific) are combined and dissolved in 5 mL of dimethylformamide (DMF; Fisher Scientific) in a test tube as precursor solution. 5 mL of OA-capped CQDs in octane (10 mg/mL) were added to the precursor solution and vortexed vigorously for 2 min until CQDs completely transferred to DMF phase. The CQDs in DMF phase were purified three times by adding octane to remove residual OA ligands. CQDs were precipitated through the addition of 0.5 mL of toluene and centrifuged at 4200 rpm for 1 min, and dried under vacuum for 20 min. Finally, CQD Inks were prepared by dispersing CQD solids in a mixture of butylamine and DMF solution (v/v = 9:1) at a concentration of 200 mg/mL, and ready for film fabrication.

Device Fabrication: For a non-graded heterojunction photodiode, 70 μL of CQD Ink solution was placed on the Si substrate and was spun at 2500 rpm for 25 s. The samples were then annealed at 70 ˚C in a N_2-filled glovebox for 30 min. After the samples were taken out of the glovebox, 100 μL of methanol/chloroform solution of ZnO nanoparticles was dropped on the substrate and spun at 5000 rpm for 20 s and this repeated twice. Finally, ITO (120 nm) was deposited *via* magnetron sputtering. For the photodiode with graded structure, two layers of EDT-treated CQDs were deposited through a solid phase exchange process: 40 μL of OA-capped PbS CQD in octane solution (50 mg/mL) was dropped on Si substrate and spun at 2500 rpm for 25 s; subsequently, an acetonitrile solution of EDT (0.01 vol%; Sigma-Aldrich) was placed on the whole sample where it remained for 30 s for ligand exchange before being spun at 2500 rpm to remove excess solution, followed by two-time rinsing with acetonitrile.

Device characterizations: Device characterizations are conducted as described in Section 5.2.

6.3 Results and discussions

The PbS CQDs show an exitonic peak at ca. 1280 nm (Figure 6.1a). Si surface passivation is done by employing the two-step chlorination/methylation procedure as described in previous chapter. We proceeded to construct the CQD/Si heterojunction photodiodes as illustrated in Figure 6.1b. CQD Inks comprising PbS-I passivated by lead halides were directly deposited onto pre-functionalized Si surface, enabling single-step fabrication. Subsequently, an electron transfer/hole blocking layer of ZnO nanoparticles was deposited onto the PbS CQD layer. The device structure was then completed by sputtering a top transparent contact of ITO. Al is sputtered at the back side of the Si, serving as the bottom contact.

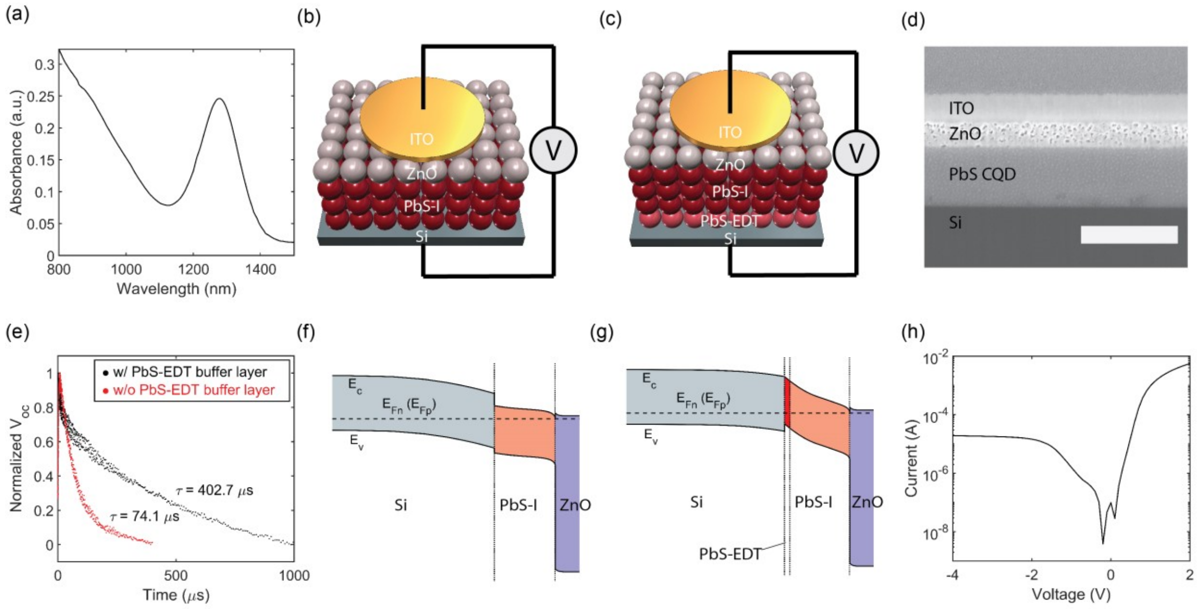

Figure 6.1. (a) Spectral absorption of an octane suspension of PbS CQDs. Illustrations showing the device structure of CQD/Si heterojunction photodiode (b) without and (c) with PbS-EDT buffer layer. (d) Scanning electron microscopy (SEM; Figure 1d) secondary electron imaging showing the cross-section of the photodiode stack; scale bar = 500 nm. (e) TPV measurement of the heterojunction photodiode. Simulated energy band diagrams for photodiode (f) without and (g) with PbS-EDT buffer layer. (h) Dark I-V characteristics for heterojunction photodiode with the PbS-EDT buffer layer. Reprinted with permission from [123]. Copyright © 2022 American Chemical Society.

The initial investigations involved photodiode based upon highly doped Si substrates (i.e., resistivity < 0.05 Ω-cm), because simulations suggest higher dopant concentration in the Si should provide higher quantum efficiency for a CQD/Si heterojunction photodiode [35]. To our surprise, and contrary to the previous report, data provided an excitonic EQE value of only ca. 5.0%. We attribute these observations to a high density of trap states at highly doped CQD-Ink/Si interface. To attempt to address the issue, we chose to insert a thin buffer layer (20 nm) of EDT capped PbS CQDs (PbS-EDT) at the interface of functionalized Si surface and CQD Ink layer (Figure 6.1c). Previous report suggests such a buffer layer effectively decreases interface recombination and facilitates charge collections [124]. SEM (Figure 6.1d) secondary electron imaging shows our procedure provides an intact layer structure within the final photodiode stack. The excitonic EQE values, obtained from the new photodiode structure containing the EDT capped PbS CQDs buffer layer, are considerably improved with the highest value up of 17%; still, EQE values obtained for our devices remain much lower than the highest values previously reported. We posit that this discrepancy may result from unsuccessful passivation on highly doped Si surface, as two-step surface treatment strategy employed here is originally designed for Si with low doping concentrations [95].

In this context, we turned our attention to low-doping concertation Si substrates (i.e., resistivity 1-10 Ω-cm). To validate the PbS-EDT buffer layer has reduced recombination rates at the CQD/Si interface, we performed TPV decay measurements for heterojunction photodiodes with both structure design (Figures 6.1b and c). Such measurements are commonly employed to investigate charge-carrier recombination and trapping/detrapping dynamics in photovoltaic and photodiode devices [108], [110], [125]. Lifetime values determined from the measurements are closely linked with steady-state charge-carrier lifetimes in devices [107], [111], [126]. Results shown in Figure 6.1e reveal that with a PbS-EDT buffer layer the lifetime increases from 74.1 μs to 402.7 μs, consistent with the suppression of interface recombination from the insertion of PbS-EDT buffer layer.

Table 6.1. SCAPS 1D modeling parameters.

	Si	PbS-EDT graded to PbS-I	ZnO
Thickness (μm)	500	0.33	0.12
Bandgap (eV)	1.12	0.97	3.200
Electron affinity (eV)	4.05	Graded from 4.05 to 4.3 (parabolic)	4.200
Relative dielectric permittivity	11.9	20	66.000

CB effective density of states (1/cm^3)	2.800E+19	1.000E+19	1.000E+19
VB effective density of states (1/cm^3)	1.040E+19	1.000E+19	1.000E+19
electron thermal velocity (cm/s)	2.300E+7	7.000E+3	1.000E+7
hole thermal velocity (cm/s)	1.650E+7	7.000E+3	1.000E+7
electron mobility (cm^2/Vs)	1.500E+3	Graded from 5.000E-3 to 5.000E-2	5.000E-2
hole mobility (cm^2/Vs)	4.500E+2	Graded from 5.000E-3 to 5.000E-2	5.000E-2
shallow uniform donor density N_D (1/cm^3)	1.000E+10	Graded from 1.000E+12 to 5.000E+15 (exponential)	1.000E+18
shallow uniform acceptor density N_A (1/cm^3)	1.350E+15	Graded from 1.000E+16 to 1.000E+12 (exponential)	2.000E+0

We also performed simulations by using a solar cell capacitance simulator (SCAPS) and parameters are listed in Table 6.1. Results in Figures 6.1f and g show the energy-band diagrams of both structures at 0 V bias. For devices without the PbS-EDT buffer layer (i.e., Figure 6.1f), photogenerated electrons and holes readily recombine at CQD/Si interface owing to the weak built-in electric field. In contrast, when the buffer-layer is introduced (i.e., Figure 6.1g) the built-in field in CQD layer is enhanced by more than seven folds, which significantly assists photocarrier separation, transport, and collection. Therefore, we chose to focus on photodiode design that includes a PbS-EDT buffer layer. Note that, a small extraction barrier exists at the CQD Ink/ZnO interface; this is because the small-bandgap PbS CQDs exhibit larger electron affinity than ZnO. To mitigate the barrier, strategies such as increasing the doping of ZnO layer can be adopted [127]. The dark current-voltage (I-V) curve is displayed in Figure 6.1h, which implies a rectifying junction formed between CQDs and Si.

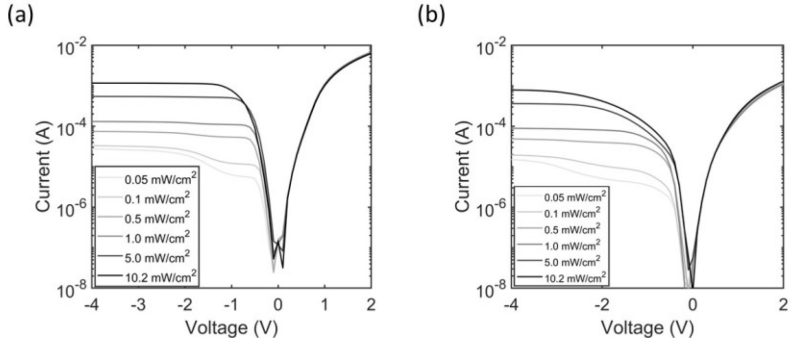

Figure 6.2. Light I-V characteristics under various levels of irradiance intensity for photodiode (a) with and (b) without buffer layer design. Reprinted with permission from [123]. Copyright © 2022 American Chemical Society.

For light I-V characteristics we shined a narrowband NIR light with a center wavelength of 1300 nm using a light-emitting diode (LED). Figure 6.2a shows the I-V characteristics for various levels of light intensities. Comparing with Figure 6.2b, it is evident that under reverse voltage bias heterojunction photodiode with buffer-layer design extracts photocarriers more effectively for illumination levels over several orders of magnitude. With this figure, one can plot the photocurrent (I_{ph}) as a function of source irradiance levels as displayed in Figure 6.3. For voltage bias ranges form -1 V to -4 V, the photocurrents scale with light intensity as $I_{ph} \sim P^k$, in which $k \approx 1.0$ is an empirical number which decreases as the trapping/detrapping dynamics dominate the photodiode. The k value close to 1 proves the high quality of near trap-free Ink film employed in this study.

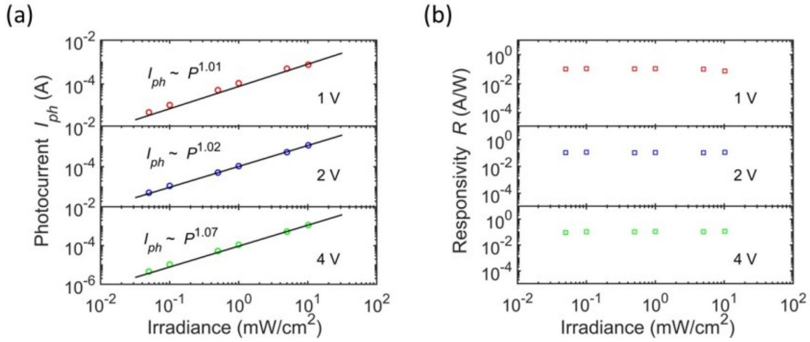

Figure 6.3. (a) Photocurrent and (b) responsivity values extracted from Figure 6.2a, as functions of irradiance intensity for different voltage biases. Reprinted with permission from [123]. Copyright © 2022 American Chemical Society.

We then calculated responsivity values as a function of illumination levels (Equation 1.1) from Figure 6.3a and results are displayed in Figure 6.3b. Numerous photodetector applications, including image sensors and optical power meters, require having constant responsivity values across wide range of irradiance levels for extracting the intensity of detection light based upon the generated photocurrent. This linearity is characterized by another figure-of-merit, linear dynamic range (LDR), within which the responsivity value remains constant:

$$\text{LDR} = 20 \times \log \frac{P_{max}}{P_{min}} \tag{6.1}$$

where P_{max} and P_{min} are upper and lower limits beyond which responsivity values start to deviate from linearity. As evident in Figure 6.3b, the responsivity stays constant in all measured irradiance intensity range. Thus, a LDR of 46 dB is obtained for the heterojunction photodiode.

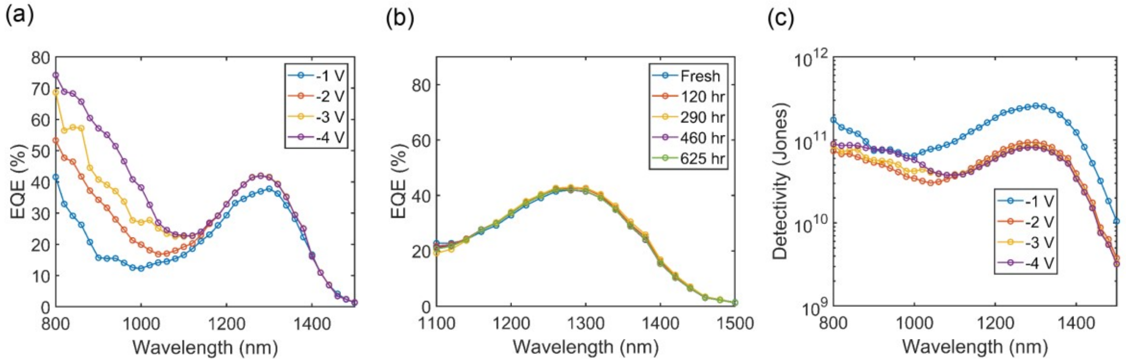

Figure 6.4 (a) EQE spectra. (b) Stability tests showing device stability after more than 625-h stored in air. (c) Detectivity spectra of the CQD/Si heterojunction photodiode. Reprinted with permission from [123]. Copyright © 2022 American Chemical Society.

High-quality Ink film and well-passivated CQD/Si heterojunction lead to high spectral EQE values and enhance the NIR sensitivity of Si up to 1500 nm, as shown in Figure 6.4a. From the figure, it is observed that with increasing reverse voltage bias EQE values at longer-wavelength region saturate. Notably, the heterojunction photodiode yields an EQE of 44% at 1280 nm under -2 V bias, which is higher than the previously reported highest value [35]. Note that one recent report demonstrated a photodiode based upon CQD/Si heterojunction with a gain > 300 [128]; nevertheless, the gain mechanism is based upon trap-assisted gain, and trapping/detrapping dynamics cause much slower temporal response, commonly at the order of milliseconds. Other CQD/Si heterojunction photodiodes that are based on hole-electron pair separation mechanism possess a much faster speed, usually at the order of microseconds. This will be further discussed later in temporal response characterizations. Another drawback of trap-assisted photodiode is their low LDR values, which is because the *k* value is smaller than 1, causing responsivity to vary with irradiance intensity. Nevertheless, the excitonic EQE value obtained here is the highest among CQD/Si heterojunction photodiode based upon photocarrier separation mechanism. Last but not least, our heterojunction photodiode exhibits superior stability without noticeable degradation in excitonic EQE value after more than 625-h (26 days) storage in ambient air (Figure 6.4b).

Figure 6.4c shows the spectral detectivity converted from spectral EQE values using the equation 5.1. Note that, we only consider the shot noise and neglect thermal noise; this is due to under reverse voltage bias, the shot noise is the dominating source [129], [130]. The heterojunction photodiode yields a specific detectivity of 2.6 × 10^{11} Jones at 1280 nm under -1 V, while it decreases with increasing reverse voltage bias as dark current level rises.

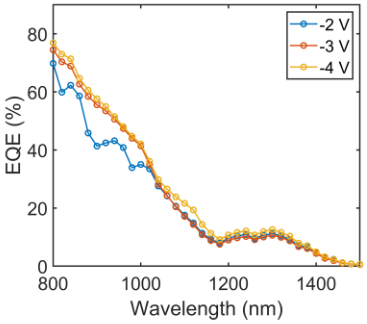

Figure 6.5. Spectral EQE of CQD/Si heterojunction photodiode without PbS-EDT buffer layer. Reprinted with permission from [123]. Copyright © 2022 American Chemical Society.

Figure 6.5 shows spectral EQE for a photodiode without buffer layer. Interestingly, photodiode without buffer layer yields high EQE at shorter wavelength (< 1100 nm) but drastically low value around 13% at longer wavelength. This could be explained as follow. PbS CQDs exhibit higher absorption at short wavelength (Figure 6.1a), and thus photons with larger energies are absorbed near CQD/ZnO interface where generated photocarriers are quickly separated by the built-in field of CQD/ZnO junction (see band diagram in Figure 6.1f). Whereas the absorption of lower-energy photons mostly happens at CQD/Si interface, and generated photocarriers fail to quickly separate owing to the low built-in field; thus holes/electrons are prone to be captured by CQD/Si interface traps, leading to low EQE values at longer wavelength shown in Figure 6.5. With the inserted PbS-EDT buffer layer, photocarriers generated in all CQD layers can be effectively collected thanks to the enhanced electric field and are less prone to be captured by the CQD/Si interface trap states, rendering high EQE values at all wavelengths displayed in Figure 6.4a.

Figure 6.6 shows the temporal responses of the heterojunction photodiode towards a chopped light signal, obtained from TPC measurements. Figure 6.6a displays a photocurrent response over the course of 50 light pulses which demonstrates the stability of our heterojunction photodiode operating under light signals in air. Figure 6.6b and 6.6c display the temporal dynamics towards single light pulse under various voltage biases and irradiance intensities. Results show a fastest rise and fall edges of 3.8 and 3.6 μs under -4 V, owing to the charge-separation mechanism in which photo-generated electrons and holes are separated and swiftly swept away by the electric field. The absence of ‘long tail’ in the fall edge, which is normally associated with the sluggish dynamics of carrier detrapping from trap states,[113], [131]–[133] for both voltage-dependent and intensity-dependent studies (Figure 6.6b and 6.6c) proves the low trap-state densities thanks to high-quality CQD/Si interface and PbS CQD Inks. To be noted that the temporal response is mainly limited by resistance-capacitance (RC) delay as the active area is large (0.20 cm^2). This is proven in Figure 6.6d, in which the device area is reduced down to 0.03 cm^2, and we obtained a faster photoresponse with rise and fall times of 1.9 and 1.2 μs. The microsecond response time obtained from our heterojunction photodiode is several orders of magnitudes faster than the millisecond response for the CQD/Si heterojunction photodiode based upon trap-assisted gain that has been discussed earlier in EQE characterizations [128]. In Table 6.2, we compared the main figure-of-merits of the demonstrated device with other Si heterojunction photodetectors. Comparing to other photodetectors, PbS CQD integrated photodetectors effectively extend the sensitivity of the Si heterojunction photodetector outside 1100 nm (cutoff absorption of Si) and show high detectivity in short-wave infrared (SWIR).

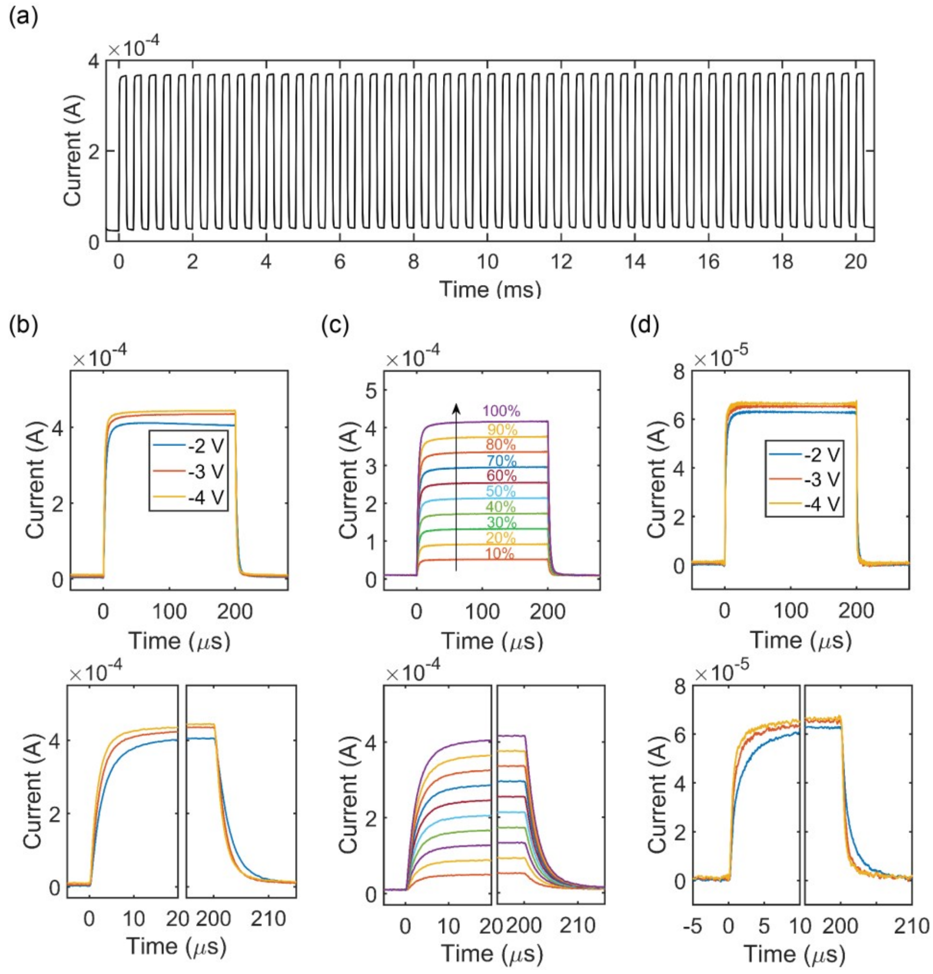

Figure 6.6 (a) Stable photoresponse towards chopped white light (50 pulses) at -4 V bias in air. Temporal responses of a single light pulse at the top for different (b) voltage biases, (c) illumination levels from 10% to 100% under -4 V, (d) a small-area device, and with their zoom-in images showing rise and fall edges at the bottom panels. Reprinted with permission from [123]. Copyright © 2022 American Chemical Society.

Table 6.2. Comparison of figure-of-merits between different reported Si heterojunction photodetectors.

Materials	Operating range [nm]	Surface passivation	Structure [a)]	Rise/fall time	Detectivity [jones]	Voltage bias	Ref.
Si-FDS010	200-1100	-	PD	1/1 ns	1.78×10^{12} @ 830 nm	V_r = -10 V	Commercial
Si/PbS-EDT/PbS Ink/ZnO	400-1500	Chlorination/ methylation	PD	1.9/1.2 μs @ 3 mm^2	3.2×10^{11} @ 1280 nm	V_r = -2 V	This work
Si/PbS-TBAI[b)]/ZnO	800-1500	Chlorination/ methylation	PD	2.5/3.3 μs @ 9 mm^2	8.8×10^{10} @ 1280 nm	V_r = -4 V	[104]
Si/PbS-EDT/ZnO	600-1800	Methyl iodine	PD	2.04/5.34 μs @ 18 mm^2	1.47×10^{11} @ 1540 nm	V_r = 0 V	[35]
Si/ZnO/PbS-TBAI/PbS-EDT	600-1800	ZnO	PD	47.6/0.8 μs @ 5 mm^2	4.1×10^{11} @ 1490 nm	V_r = -0.25 V	[75]
Si/PbS-TBAI/ZnO	400-1400	Methyl iodine	PD	-	1.5×10^{11} @ 1230 nm	V_r = -7 V	[34]

Si/PbS-EDT/PbS-TBAI	600-1600	Hydrologic acid	PT	ms scale	~2.0×10^{13} @ 1550 nm	V_{ce}= 1 V	[128]
Si/perovskite	405 - 1064	-	PD	0.52/2.44 µs @ 40 mm^2	5.9×10^{10} @ 1064 nm	V_r = -1 V	[60]
Si/SiO$_2$/graphene	300-1100	Native SiO$_2$	PD	0.32/0.75ms @ 10 mm^2	4.1×10^{13} @ 890 nm	V_r = 0 V	[134]
Si/graphene	400-900	Hydrologic acid	PD	1.2/3 ms @ 0.05 mm^2	2.1×10^{8} @ 730 nm	V_r = -2 V	[135]
Si/AlN/graphene	350-900	Hydrologic acid	PD	1.9/1.4 ms	1.13×10^{8} @ 850 nm	V_r = -10 V	[136]
a-Si/MoS$_2$	400-625	-	PT	0.3/0.3 ms	-	V_{DS} = 1 V	[137]
Si/PEDOT:PSS	350-950	Hydrologic acid	PT	28/40 µs @ 25 mm^2	1.5×10^{10} @ 656 nm	V_{DS} = 2 V	[138]
Si NW/PEDOT:PSS	300-1100	Chlorination/ methylation	PD	3.17/55.4 µs @ 0.3 cm^2	4.1×10^{11} @ 656 nm	V_r = 0 V	[139]
Si/MoS$_2$	300-1100	Hydrologic acid	PD	10/19 µs @ 0.01 mm^2	1.4×10^{12} @ 580 nm	V_r = -2 V	[140]
Si/MoSe$_2$/graphene	365-1310	Hydrologic acid	PD	0.27/0.35 µs @ 7 mm^2	7.13×10^{10} @ 650 nm	V_r = -5 V	[141]
Si/WS$_2$	785	-	PD	17.7/5.2 ms	1.17×10^{9} @ 785 nm	V_r = -3 V	[142]

Si/$SnS_{1-x}Se_x$	635-1200	Hydrologic acid	PD	4.7/3.9 ms @ 343 μm^2	1.0×10^{11} @ 635 nm	$V_r = 0$ V	[143]
Si NW/TiO_2/P3HT	300-1100	-	PD	84/153 ms @ 0.7 cm^2	1.38×10^{14} @ 920 nm	$V_r = 0$ V	[144]

[a] PD and PT stand for photodiode and phototransistor, respectively.

6.4 Summary

This chapter demonstrated the integration of PbS CQD Inks with c-Si and constructed a high-performance heterojunction photodiode. Thanks to the highly efficient Si surface passivation, high-quality PbS CQD Inks and the design with a CQD-EDT buffer layer, the heterojunction photodiode yields an excitonic EQE value up to 44% at -2 V, a detectivity value up to 2.58×10^{11} Jones at -1 V, and fast photoresponse of less than 4 μs without any sluggish tail. The fast photoresponse is attributed to the low trap-state densities, as proved in both TPV and TPC measurements. The device also exhibited superior stability over the course of 625-h exposure in air ambient. The approach proposed in this study opens the door for low-complexity and monolithic integration of CQD Ink devices on Si for potential applications such as on-chip NIR lasing and photodetection for Si photonics technology [61], [62], [145], [146].

7. Colloidal quantum dot CMOS image sensor for near-infrared imaging

7.1 Background

NIR CIS enables significant applications such medical imaging, night vision and self-driving cars. Mature commercial solution is using InGaAs material. Main process including high-temperature epitaxial growth of InGaAs on InP substrate, subsequently followed by InGaAs dicing and flip-chip bonding of InGaAs onto die circuits. However, this method is non-wafer scale and severely limits the throughput. Another drawback is that pixel size is limited by bond pitch distance during the flip-chip bonding process and thus it restricts CIS pixel resolution. For example, InGaAs-based NIR CIS provided by TELEDYNE (Tau® SWIR) has a pixel size of 15 μm and a resolution 640 × 512; this is in drastic comparison to Si-based visible CIS that has a pixel size as small as ~1 μm and a resolution of 3,264 × 2,448 pixels in an area just 1mm × 1mm in size.

On the other hand, thanks to the solution processability at room temperature, CQDs could be integrated with ROIC circuit in large area without bonding requirement; thus, CQD-based NIR CIS could be realized with smaller pixel size (higher resolution), drastically lower energy cost and manufacturing complexity. As we have mentioned in Section 1.4.4, several CQD NIR CIS have been demonstrated (Figures 1.12 and 1.13), which were realized by integrating CQD photodiode [31], [33] or phototransistor [32] onto ROIC circuits. This chapter is a simulation study and will investigate the feasibility of an alternative integration strategy which is integrating CQDs onto ROIC through CQD/Si heterojunctions as discussed in the previous two chapters.

7.2 Simulation methods

The simulations were conducted using Taurus Medici. It is a 2D device simulator which is able to model the electrical and optical characteristics of various semiconductor devices. The structure of one active pixel in the proposed CQD/Si heterojunction based NIR CIS is displayed in Figure 7.1. The architecture resembles the active pixel in a Si-based visible CIS with some extra layers.

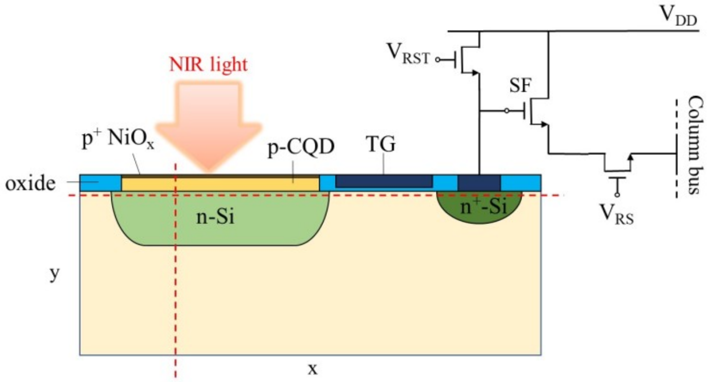

Figure 7.1. Schematics of an active pixel of a CQD-based NIR CIS.

A heterojunction is formed between a *p*-type CQD layer (doping concentration of 1×10^{16} cm^{-3}) and a n-well Si layer (doping concentration of 1×10^{16} cm^{-3}), which is buried in a *p*-type (doping concentration of 4×10^{15} cm^{-3}) Si substrate. A pinning layer of NiO_x (doping concentration of 5×10^{19} cm^{-3}) is deposited on top of CQD, which enhances the built-in field of CQD/Si heterojunction. The n-well structure is used to store the photocarriers generated from CQD layer under NIR illumination. Once transfer gate (TG) is biased (open), the photocarriers will transport to a floating diffusion (FD) made of n+ region. The voltage potential of the FD is monitored by a source follower (SF) transistor, and the information is subsequently transferred to column bus line through a row-select transistor (SEL). A reset transistor (RST) will send a reset signal once it is biased; in this case, both n-well and FD will be reset, and extra charges will be transferred out of the pixel.

7.3 Results and discussions

We first simulate the characteristics of NiO_x/CQD/Si heterojunction photodiode which is isolated from the active pixel. Figures 7.2a and b show the electrostatic potential of the structure in dark and under illumination along the vertical dashed red line shown in Figure 7.1. The diagram in Figure 7.2a shows a *p+*/*p*/*n*/*p* type heterojunction formed in the dark. The extra layer of NiO effectively enhances the built-in electric filed. Figure 7.2b clearly shows that the voltage potential in the n-well significantly decreases under NIR light illumination because of the accumulation of photo-electrons generated and transported from CQD layer. The voltage potential in NiO_x layer slightly increases due to the accumulation of holes in the layer.

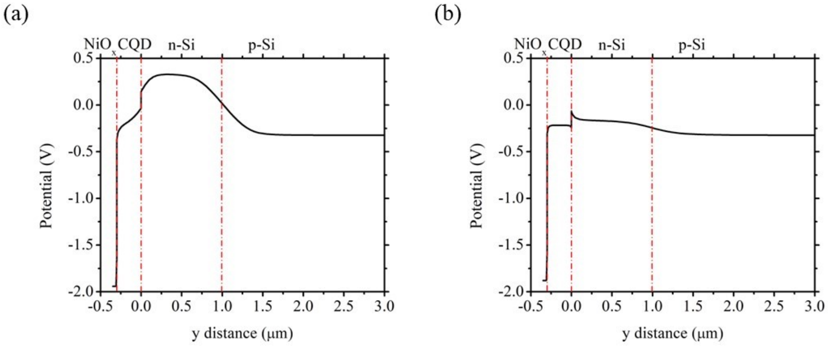

Figure 7.2. Electrostatic potential of NiO_x/CQD/Si heterojunction photodiode in (a) dark and (b) under illumination along the red dashed line shown in Figure 7.1.

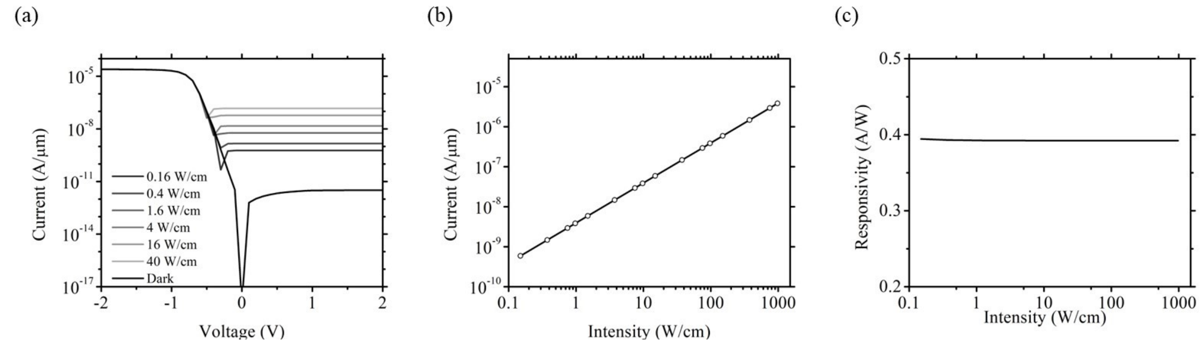

Figure 7.3. (a) I-V curves of NiO/CQD/Si heterojunction photodiode in the dark and various light intensities. (b) Photocurrent at various intensities. (c) Responsivity values as a function of intensity showing good linearity.

Figure 7.3a demonstrates the simulated photocurrent as a function of bias voltage for the photodiode under various light intensities. In dark, it is clearly observed that a rectifying junction is formed between *p*-type CQD and *n*-type Si layers with current density down to 3×10^{-12} A/μm at reverse bias. Photocurrent as a function of light intensity is depicted in Figure 7.3b. The values are fitted as $I_{ph} \sim P^k$, in which k close to 1, thanks to the low trap density of CQD layer (discussed in section 6.3). Responsivity values are calculated from Equation 1.1 and plotted in Figure 7.3c as a function of intensity. The values remain stable for all intensity, indicating superior linearity which is crucial for the CIS.

We then proceeded to simulate the active pixel in Figure 7.4, which shows the voltage potential at along horizontal direction at y = 10 nm in the dark and under illumination. In both cases, when the TG is not biased, the n-p junction formed between n-well and channel beneath the gate renders a potential barrier preventing electrons from traveling through. Once TG is biased, an inversion layer is formed beneath the gate and drops the potential barrier. Under illumination, photo-generated carriers are temporarily stored in n-well if TG is closed (voltage potential decreases in n-well) and are readily transferred from n-well to FD once TG is open.

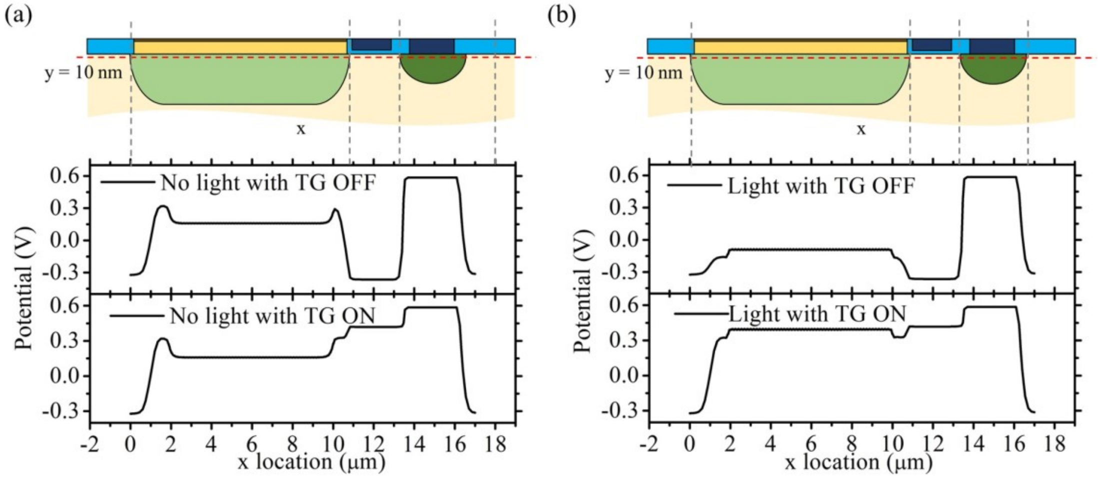

Figure 7.4. Electrostatic potential of the active pixel along the horizontal red dashed line in Figure 7.1 (y = 10 nm) in (a) dark and (b) under illumination.

Finally, we simulate the timing sequence diagram for the active pixel as shown in Figure 7.5. RST, TG and RS transistors are voltage biased (opened) periodically to transfer the signal from a selected active pixel, and a single period can be divided into three stages, that are reset, integration and read. Finally, the Out signals are read through RS and column bus. Within on period (1×10^{-4} s), it is clear from the figure that the Out signals differ in the dark (Figure 7.5a) and under (Figure 7.5b) illumination at "read" stage: Out remains high signal level in the dark while it is low level under NIR light. The demonstration here proves that CQD-based NIR CIS can generate signals under NIR light using similar device structure as the conventional Si-based visible CIS.

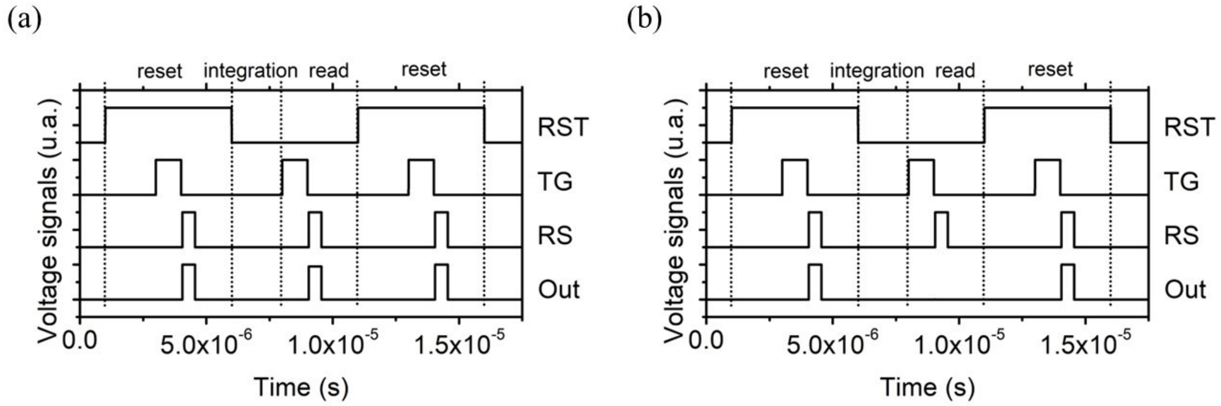

Figure 7.5. Timing sequence diagram of the active pixel (a) in the dark and (b) under illumination.

7.4 Summary

The solution processability of CQDs promises large-area and monolithic integration on Si-ROICs; this enables low-cost CQD-based NIR CIS with high resolution. This chapter presented a simulation study on CQD-based CIS, in which CQDs were integrated by forming a CQD/Si heterojunction. Results show that CIS is sensitive to NIR light thanks to CQD film, and signal carriers are successfully transferred through the ROICs. The investigation in this chapter provides alternative integration method of CQDs with Si ROICs for achieving CQD-based NIR CIS.

8. Conclusions

8.1 Summary of accomplishments and contributions

The investigations conducted in this thesis explore fast and efficient NIR light detection realized by CQD-based photodetectors. The heart of the thesis is centred around the integration of CQD with Si and achieving on-Si CQD-based NIR photodetection.

We have demonstrated a fast CQD photodiode that exhibits fast rise and fall times of 0.3 μs even with a low mobility CQD material. This was done by employing a physical model that predicts Si photodiode temporal response. We applied the model to CQD photodiode and synergized the carrier transport and RC effect; this has afforded a fast temporal response.

We proposed a POSFET structure for integration on Si. The structure replaces the poly Si gate in a conventional CMOS transistor with a CQD photodiode. The photovoltage generated from the photodiode modulates the channel conductivity in the transistor, the same as the voltage modulation from poly Si gate in the CMOS transistor. The integration is CMOS compatible and highly scalable. Simulations and proof-of-concept experiments were employed to prove the feasibility of the method.

Forming a heterojunction between CQD and Si is another straightforward integration method. The performance of heterojunction devices heavily depends on the junction quality. In this regard, we have proposed using two-step chlorination/methylation method for Si surface passivation. The method shows improved passivation efficiency compared to the conventional one-step methyl-iodine passivation and greatly supress Si surface trap densities. Moreover, CQD/Si heterojunction photodiode based upon the two-step method shows near double EQE enhancement over the one based on one-step method.

Considering CQD inks exhibit extremely low trap density and have yielded best performance optoelectronic devices to date, we demonstrated CQD ink/Si heterojunction photodiode. Direct contact of CQD ink with Si yielded low EQE efficiency due to weak built-in field. By inserting a buffer layer of PbS-EDT layer in between, not only built-in field has been improved by seven folds, but interface carrier recombination is also reduced. Such improvements have afforded a CQD/Si heterojunction photodiode that has high EQE combined with fast temporal response.

One of the practical significances of CQD-based NIR photodetection for building a low-cost NIR CIS. The final work in this thesis proposed to employ CQD/Si heterojunction for realizing CQD-based NIR CIS. Simulations were utilized to validate the feasibility of proposed device. Results showed that signals in the dark/light from the CQD/Si photodiode can be read out through the conventional Si-based ROICs.

The works demonstrated in this thesis provided solutions for achieving efficient, fast, and low-cost NIR light detection; the works also pointed out to the significance of on-Si integration, as such integration is critical for realizing much broader practical applications for CQD. One is CQD-based NIR CIS that already has been discussed here, the other is on-chip NIR photodetection that will be discussed in the next section.

8.2 Future works

Part of the future works will be centred around realizing experimental proof of POSFET and NIR CIS. I will expect this to be sophisticated since the Si circuit has to be customized. Commercial Si circuits are normally packaged before delivery, and hence it is hard to achieve direct integration. To this end, we will be closely collaborating with semiconductor foundries or any other fabrication facility within Canada and try to fabricate Si circuits with exposed area for the following CQD integration. For example, for the case of NIR CIS, with the collaboration we might be able to fabricate Si die/wafer with exposed n-well areas; upon receive them, we will utilize in-lab resources to finish up the fabrication.

The rest of the future works focus on the experimental demonstration of CQD integration with Si waveguides in the Si photonics platform, which was investigated in theory in Chapter 4. Si photonics has been regarded as one of the most promising strategies for Lidar devices. Since it is compatible with CMOS technology, such devices could be fabricated with low-cost and in compact sizes; this is in drastic contrast to the Lidar technology nowadays based upon mechanical laser scanning which is bulky and costly. Further, since Si photonics utilizes coherent light, such Lidar devices are much more immune to outside uncoherent noises. Si photonics Lidar devices using longer wavelengths (e.g., 1550 nm) is proven to be eye-safe and important; however, achieving low-cost and sensitive on-chip photodetection in this wavelength range was found to be challenging as discussed in Chapter 4. CQD integrated with Si waveguide could possibly address the issue. To this end, we will design and fabricate the Si photonics chip using the NanoFAB facility in the University of Alberta. In the end, we will package the chip and send the chips to other groups equipped with setups and experiences in investigating Si photonics-based Lidar technology.

Reference

[1] D. Ahn *et al.*, “High performance, waveguide integrated Ge photodetectors,” *Opt. Express*, vol. 15, no. 7, p. 3916, 2007.

[2] L. Colace, G. Masini, G. Assanto, H.-C. Luan, K. Wada, and L. C. Kimerling, “Efficient high-speed near-infrared Ge photodetectors integrated on Si substrates,” *Appl. Phys. Lett.*, vol. 76, no. 10, pp. 1231–1233, Mar. 2000.

[3] T. Yin *et al.*, “31 GHz Ge n-i-p waveguide photodetectors on Silicon-on-Insulator substrate,” *Opt. Express*, vol. 15, no. 21, p. 13965, 2007.

[4] J. Michel, J. Liu, and L. C. Kimerling, “High-performance Ge-on-Si photodetectors,” *Nat. Photonics*, vol. 4, no. 8, pp. 527–534, Aug. 2010.

[5] J. Wang and S. Lee, “Ge-photodetectors for Si-based optoelectronic integration,” *Sensors*, vol. 11, no. 1. pp. 696–718, 2011.

[6] J. Zhang *et al.*, “Transfer-printing-based integration of a III-V-on-silicon distributed feedback laser,” *Opt. Express*, vol. 26, no. 7, p. 8821, Apr. 2018.

[7] S. Dhoore, S. Uvin, D. Van Thourhout, G. Morthier, and G. Roelkens, “Novel adiabatic tapered couplers for active III–V/SOI devices fabricated through transfer printing,” *Opt. Express*, vol. 24, no. 12, p. 12976, Jun. 2016.

[8] K. Ohira *et al.*, “On-chip optical interconnection by using integrated III-V laser diode and photodetector with silicon waveguide,” *Opt. Express*, vol. 18, no. 15, p. 15440, Jul. 2010.

[9] A. Beling *et al.*, “InP-based waveguide photodiodes heterogeneously integrated on silicon-on-insulator for photonic microwave generation,” *Opt. Express*, vol. 21, no. 22, p.

25901, Nov. 2013.

[10] K. Sun *et al.*, “Low dark current III–V on silicon photodiodes by heteroepitaxy,” *Opt. Express*, vol. 26, no. 10, p. 13605, May 2018.

[11] Y. Yuan *et al.*, “III-V on silicon avalanche photodiodes by heteroepitaxy,” *Opt. Lett.*, vol. 44, no. 14, p. 3538, Jul. 2019.

[12] M. M. P. Fard, G. Cowan, and O. Liboiron-Ladouceur, “Responsivity optimization of a high-speed germanium-on-silicon photodetector,” *Opt. Express*, vol. 24, no. 24, p. 27738, Nov. 2016.

[13] G. Konstantatos and E. H. Sargent, “Nanostructured materials for photon detection,” *Nat. Nanotechnol.*, vol. 5, no. 6, pp. 391–400, Jun. 2010.

[14] F. P. García de Arquer, A. Armin, P. Meredith, and E. H. Sargent, “Solution-processed semiconductors for next-generation photodetectors,” *Nat. Rev. Mater.*, vol. 2, no. 3, p. 16100, Mar. 2017.

[15] M. Li *et al.*, “Sensitive NO 2 gas sensors employing spray-coated colloidal quantum dots,” *Thin Solid Films*, vol. 618, pp. 271–276, Nov. 2016.

[16] H. Aqoma and S.-Y. Jang, “Solid-state-ligand-exchange free quantum dot ink-based solar cells with an efficiency of 10.9%,” *Energy Environ. Sci.*, vol. 11, no. 6, pp. 1603–1609, 2018.

[17] I. J. Kramer *et al.*, “Efficient Spray-Coated Colloidal Quantum Dot Solar Cells,” *Adv. Mater.*, vol. 27, no. 1, pp. 116–121, Jan. 2015.

[18] R. Sliz *et al.*, “Stable Colloidal Quantum Dot Inks Enable Inkjet-Printed High-Sensitivity Infrared Photodetectors,” *ACS Nano*, vol. 13, no. 10, pp. 11988–11995, Oct. 2019.

[19] K. Xu, W. Zhou, and Z. Ning, "Integrated Structure and Device Engineering for High Performance and Scalable Quantum Dot Infrared Photodetectors," *Small*, vol. 16, no. 47, p. 2003397, Nov. 2020.

[20] G. Konstantatos *et al.*, "Ultrasensitive solution-cast quantum dot photodetectors," *Nature*, vol. 442, no. 7099, pp. 180–183, Jul. 2006.

[21] J. He *et al.*, "Synergetic Effect of Silver Nanocrystals Applied in PbS Colloidal Quantum Dots for High-Performance Infrared Photodetectors," *ACS Photonics*, vol. 1, no. 10, pp. 936–943, Oct. 2014.

[22] J. P. Clifford, G. Konstantatos, K. W. Johnston, S. Hoogland, L. Levina, and E. H. Sargent, "Fast, sensitive and spectrally tuneable colloidal-quantum-dot photodetectors," *Nat. Nanotechnol.*, vol. 4, no. 1, pp. 40–44, Jan. 2009.

[23] B. N. Pal, I. Robel, A. Mohite, R. Laocharoensuk, D. J. Werder, and V. I. Klimov, "High-Sensitivity p-n Junction Photodiodes Based on PbS Nanocrystal Quantum Dots," *Adv. Funct. Mater.*, vol. 22, no. 8, pp. 1741–1748, Apr. 2012.

[24] J. R. Manders *et al.*, "Low-Noise Multispectral Photodetectors Made from All Solution-Processed Inorganic Semiconductors," *Adv. Funct. Mater.*, vol. 24, no. 45, pp. 7205–7210, Sep. 2014.

[25] D. Jarzab, K. Szendrei, M. Yarema, S. Pichler, W. Heiss, and M. A. Loi, "Charge-Separation Dynamics in Inorganic-Organic Ternary Blends for Efficient Infrared Photodiodes," *Adv. Funct. Mater.*, vol. 21, no. 11, pp. 1988–1992, Jun. 2011.

[26] L. Shen, Y. Zhang, Y. Bai, X. Zheng, Q. Wang, and J. Huang, "A filterless, visible-blind, narrow-band, and near-infrared photodetector with a gain," *Nanoscale*, vol. 8, no. 26, pp.

12990–12997, 2016.

[27] R. Dong *et al.*, “An Ultraviolet-to-NIR Broad Spectral Nanocomposite Photodetector with Gain,” *Adv. Opt. Mater.*, vol. 2, no. 6, pp. 549–554, Jun. 2014.

[28] J. W. Lee, D. Y. Kim, and F. So, “Unraveling the Gain Mechanism in High Performance Solution-Processed PbS Infrared PIN Photodiodes,” *Adv. Funct. Mater.*, vol. 25, no. 8, pp. 1233–1238, Feb. 2015.

[29] G. Konstantatos *et al.*, “Hybrid graphene–quantum dot phototransistors with ultrahigh gain,” *Nat. Nanotechnol.*, vol. 7, no. 6, pp. 363–368, Jun. 2012.

[30] I. Nikitskiy *et al.*, “Integrating an electrically active colloidal quantum dot photodiode with a graphene phototransistor,” *Nat. Commun.*, vol. 7, no. 1, p. 11954, Sep. 2016.

[31] T. Rauch *et al.*, “Near-infrared imaging with quantum-dot-sensitized organic photodiodes,” *Nat. Photonics*, vol. 3, no. 6, pp. 332–336, Jun. 2009.

[32] S. Goossens *et al.*, “Broadband image sensor array based on graphene–CMOS integration,” *Nat. Photonics*, vol. 11, no. 6, pp. 366–371, Jun. 2017.

[33] J. Liu *et al.*, “A near-infrared colloidal quantum dot imager with monolithically integrated readout circuitry,” *Nat. Electron.*, vol. 5, no. 7, pp. 443–451, Jun. 2022.

[34] S. Masala *et al.*, “The Silicon:Colloidal Quantum Dot Heterojunction,” *Adv. Mater.*, vol. 27, no. 45, pp. 7445–7450, Dec. 2015.

[35] K. Xu *et al.*, “Inverted Si:PbS Colloidal Quantum Dot Heterojunction-Based Infrared Photodetector,” *ACS Appl. Mater. Interfaces*, vol. 12, no. 13, pp. 15414–15421, Apr. 2020.

[36] V. Adinolfi and E. H. Sargent, “Photovoltage field-effect transistors,” *Nature*, vol. 542, no. 7641, pp. 324–327, Feb. 2017.

[37] D. Kufer, I. Nikitskiy, T. Lasanta, G. Navickaite, F. H. L. Koppens, and G. Konstantatos, “Hybrid 2D-0D MoS 2 -PbS Quantum Dot Photodetectors,” *Adv. Mater.*, vol. 27, no. 1, pp. 176–180, Jan. 2015.

[38] S. Pak *et al.*, “Consecutive Junction-Induced Efficient Charge Separation Mechanisms for High-Performance MoS 2 /Quantum Dot Phototransistors,” *ACS Appl. Mater. Interfaces*, vol. 10, no. 44, pp. 38264–38271, Nov. 2018.

[39] D. Kufer, T. Lasanta, M. Bernechea, F. H. L. Koppens, and G. Konstantatos, “Interface Engineering in Hybrid Quantum Dot–2D Phototransistors,” *ACS Photonics*, vol. 3, no. 7, pp. 1324–1330, Jul. 2016.

[40] O. Özdemir, I. Ramiro, S. Gupta, and G. Konstantatos, “High Sensitivity Hybrid PbS CQD-TMDC Photodetectors up to 2 μm,” *ACS Photonics*, vol. 6, no. 10, pp. 2381–2386, Oct. 2019.

[41] A.-Y. Lee *et al.*, “Hybrid Black Phosphorus/Zero-Dimensional Quantum Dot Phototransistors: Tunable Photodoping and Enhanced Photoresponsivity,” *ACS Appl. Mater. Interfaces*, vol. 10, no. 18, pp. 16033–16040, May 2018.

[42] L. Ye, H. Li, Z. Chen, and J. Xu, “Near-Infrared Photodetector Based on MoS 2 /Black Phosphorus Heterojunction,” *ACS Photonics*, vol. 3, no. 4, pp. 692–699, Apr. 2016.

[43] D. Kufer and G. Konstantatos, “Photo-FETs: Phototransistors Enabled by 2D and 0D Nanomaterials,” *ACS Photonics*, vol. 3, no. 12, pp. 2197–2210, Dec. 2016.

[44] L. Meng, T. Zeng, Y. Jin, Q. Xu, and X. Wang, “Surface-Modified Substrates for

Quantum Dot Inks in Printed Electronics," *ACS Omega*, vol. 4, no. 2, pp. 4161–4168, Feb. 2019.

[45] C.-H. M. Chuang, P. R. Brown, V. Bulović, and M. G. Bawendi, "Improved performance and stability in quantum dot solar cells through band alignment engineering," *Nat. Mater.*, vol. 13, no. 8, pp. 796–801, Aug. 2014.

[46] L. Meng, Q. Xu, S. Fan, C. R. Dick, and X. Wang, "Field-effect enhanced triboelectric colloidal quantum dot flexible sensor," *Appl. Phys. Lett.*, vol. 111, no. 18, p. 183103, Oct. 2017.

[47] Q. Xu, L. Meng, K. Sinha, F. I. Chowdhury, J. Hu, and X. Wang, "Ultrafast Colloidal Quantum Dot Infrared Photodiode," *ACS Photonics*, vol. 7, no. 5, pp. 1297–1303, May 2020.

[48] A. O. Goushcha and B. Tabbert, "On response time of semiconductor photodiodes," *Opt. Eng.*, vol. 56, no. 09, p. 1, Sep. 2017.

[49] E. Georgitzikis *et al.*, "Optimization of Charge Carrier Extraction in Colloidal Quantum Dots Short-Wave Infrared Photodiodes through Optical Engineering," *Adv. Funct. Mater.*, vol. 28, no. 42, p. 1804502, Oct. 2018.

[50] V. Malgras *et al.*, "Trap-Assisted Transport and Non-Uniform Charge Distribution in Sulfur-Rich PbS Colloidal Quantum Dot-based Solar Cells with Selective Contacts," *ACS Appl. Mater. Interfaces*, vol. 7, no. 48, pp. 26455–26460, Dec. 2015.

[51] G. Juška, M. Viliūnas, K. Arlauskas, N. Nekrašas, N. Wyrsch, and L. Feitknecht, "Hole drift mobility in μc-Si:H," *J. Appl. Phys.*, vol. 89, no. 9, pp. 4971–4974, May 2001.

[52] J. Tang *et al.*, "Colloidal-quantum-dot photovoltaics using atomic-ligand passivation,"

Nat. Mater., vol. 10, no. 10, pp. 765–771, Oct. 2011.

[53] Y. Tang *et al.*, “A Colloidal-Quantum-Dot Infrared Photodiode with High Photoconductive Gain,” *Small*, vol. 14, no. 48, p. 1803158, Nov. 2018.

[54] X. Wang *et al.*, “Amorphous ZnO/PbS Quantum Dots Heterojunction for Efficient Responsivity Broadband Photodetectors,” *ACS Appl. Mater. Interfaces*, vol. 12, no. 7, pp. 8403–8410, Feb. 2020.

[55] J.-Y. Zhang, J.-L. Xu, T. Chen, X. Gao, and S.-D. Wang, “Toward Broadband Imaging: Surface-Engineered PbS Quantum Dot/Perovskite Composite Integrated Ultrasensitive Photodetectors,” *ACS Appl. Mater. Interfaces*, vol. 11, no. 47, pp. 44430–44437, Nov. 2019.

[56] A. Chu *et al.*, “Near Unity Absorption in Nanocrystal Based Short Wave Infrared Photodetectors Using Guided Mode Resonators,” *ACS Photonics*, vol. 6, no. 10, pp. 2553–2561, Oct. 2019.

[57] N. Huo and G. Konstantatos, “Ultrasensitive all-2D MoS2 phototransistors enabled by an out-of-plane MoS2 PN homojunction,” *Nat. Commun.*, vol. 8, no. 1, p. 572, Dec. 2017.

[58] Z. Ren *et al.*, “Bilayer PbS Quantum Dots for High-Performance Photodetectors,” *Adv. Mater.*, vol. 29, no. 33, p. 1702055, Sep. 2017.

[59] V. Adinolfi, I. J. Kramer, A. J. Labelle, B. R. Sutherland, S. Hoogland, and E. H. Sargent, “Photojunction Field-Effect Transistor Based on a Colloidal Quantum Dot Absorber Channel Layer,” *ACS Nano*, vol. 9, no. 1, pp. 356–362, Jan. 2015.

[60] X. Geng *et al.*, “Ultrafast Photodetector by Integrating Perovskite Directly on Silicon Wafer,” *ACS Nano*, vol. 14, no. 3, pp. 2860–2868, Mar. 2020.

[61] Q. Xu, L. Meng, T. Zeng, K. Sinha, C. Dick, and X. Wang, “On-chip colloidal quantum dot devices with a CMOS compatible architecture for near-infrared light sensing,” *Opt. Lett.*, vol. 44, no. 2, p. 463, Jan. 2019.

[62] D. Thomson *et al.*, “Roadmap on silicon photonics,” *J. Opt.*, vol. 18, no. 7, p. 073003, Jul. 2016.

[63] J. J. Ackert *et al.*, “High-speed detection at two micrometres with monolithic silicon photodiodes,” *Nat. Photonics*, vol. 9, no. 6, pp. 393–396, Jun. 2015.

[64] P. Runge *et al.*, “Waveguide Integrated Balanced Photodetectors for Coherent Receivers,” *IEEE J. Sel. Top. Quantum Electron.*, vol. 24, no. 2, pp. 1–7, Mar. 2018.

[65] W. Xie *et al.*, “Heterogeneous silicon photonics sensing for autonomous cars [Invited],” *Opt. Express*, vol. 27, no. 3, p. 3642, Feb. 2019.

[66] C. V. Poulton *et al.*, “Coherent solid-state LIDAR with silicon photonic optical phased arrays,” *Opt. Lett.*, vol. 42, no. 20, p. 4091, Oct. 2017.

[67] J. G. Wangüemert-Pérez *et al.*, “Subwavelength structures for silicon photonics biosensing,” *Opt. Laser Technol.*, vol. 109, pp. 437–448, Jan. 2019.

[68] Y. Chen, H. Lin, J. Hu, and M. Li, “Heterogeneously integrated silicon photonics for the mid-infrared and spectroscopic sensing,” *ACS Nano*, vol. 8, no. 7, pp. 6955–6961, 2014.

[69] Jungwoo Oh *et al.*, “Interdigitated Ge p-i-n photodetectors fabricated on a Si substrate using graded SiGe buffer layers,” *IEEE J. Quantum Electron.*, vol. 38, no. 9, pp. 1238–1241, Sep. 2002.

[70] L. Vivien *et al.*, “42 GHz pin Germanium photodetector integrated in a silicon-on-insulator waveguide,” *Opt. Express*, vol. 17, no. 8, p. 6252, Apr. 2009.

[71] C. T. DeRose *et al.*, “Ultra compact 45 GHz CMOS compatible Germanium waveguide photodiode with low dark current,” *Opt. Express*, vol. 19, no. 25, p. 24897, Dec. 2011.

[72] H. Roehle *et al.*, “Next generation 15 µm terahertz antennas: mesa-structuring of InGaAs/InAlAs photoconductive layers,” *Opt. Express*, vol. 18, no. 3, p. 2296, Feb. 2010.

[73] P.-H. Richter *et al.*, “Ultrafast THz Conductivity Dynamics of a Novel Fe-Doped InGaAs Quantum Photoconductor,” *IEEE Trans. Terahertz Sci. Technol.*, vol. 10, no. 2, pp. 167–175, Mar. 2020.

[74] B. Globisch *et al.*, “Iron doped InGaAs: Competitive THz emitters and detectors fabricated from the same photoconductor,” *J. Appl. Phys.*, vol. 121, no. 5, p. 053102, Feb. 2017.

[75] X. Xiao *et al.*, “High quality silicon: Colloidal quantum dot heterojunction based infrared photodetector,” *Appl. Phys. Lett.*, vol. 116, no. 10, p. 101102, Mar. 2020.

[76] J. Cui and Z. Zhou, “High-performance Ge-on-Si photodetector with optimized DBR location,” *Opt. Lett.*, 2017.

[77] H. Zhou and Y. Sun, “Size reduction of Ge-on-Si photodetectors via a photonic bandgap,” *Appl. Opt.*, vol. 57, no. 12, p. 2962, Apr. 2018.

[78] A. Novack *et al.*, “Germanium photodetector with 60 GHz bandwidth using inductive gain peaking,” *Opt. Express*, vol. 21, no. 23, p. 28387, Nov. 2013.

[79] M. I. Nugraha *et al.*, “Rapid Photonic Processing of High-Electron-Mobility PbS Colloidal Quantum Dot Transistors,” *ACS Appl. Mater. Interfaces*, vol. 12, no. 28, pp. 31591–31600, Jul. 2020.

[80] D. Zhitomirsky *et al.*, “Engineering colloidal quantum dot solids within and beyond the

mobility-invariant regime," *Nat. Commun.*, vol. 5, no. 1, p. 3803, Sep. 2014.

[81] W. Setyawan, R. M. Gaume, S. Lam, R. S. Feigelson, and S. Curtarolo, "High-Throughput Combinatorial Database of Electronic Band Structures for Inorganic Scintillator Materials," *ACS Comb. Sci.*, vol. 13, no. 4, pp. 382–390, Jul. 2011.

[82] Q. Xu, J. Hu, and X. Wang, "On-chip Ge, InGaAs, and colloidal quantum dot photodetectors: comparisons for application in silicon photonics," *J. Opt. Soc. Am. B*, vol. 38, no. 1, 2021.

[83] M. Balbi, V. Sorianello, L. Colace, and G. Assanto, "Analysis of temperature dependence of Ge-on-Si p–i–n photodetectors," *Phys. E Low-dimensional Syst. Nanostructures*, vol. 41, no. 6, pp. 1086–1089, May 2009.

[84] L. Colace, M. Balbi, V. Sorianello, and G. Assanto, "Temperature-Dependence of Ge on Si p–i–n Photodetectors," *J. Light. Technol.*, vol. 26, no. 14, pp. 2211–2214, Jul. 2008.

[85] M. Piels and J. E. Bowers, "Photodetectors for silicon photonic integrated circuits," in *Photodetectors*, Elsevier, 2016, pp. 3–20.

[86] I. Ramiro, B. Kundu, M. Dalmases, O. Özdemir, M. Pedrosa, and G. Konstantatos, "Size- and Temperature-Dependent Intraband Optical Properties of Heavily n-Doped PbS Colloidal Quantum Dot Solid-State Films," *ACS Nano*, vol. 14, no. 6, pp. 7161–7169, Jun. 2020.

[87] J. Liu *et al.*, "Tensile strained Ge p-i-n photodetectors on Si platform for C and L band telecommunications," *Appl. Phys. Lett.*, vol. 87, no. 1, p. 011110, Jul. 2005.

[88] M. Oehme, J. Werner, E. Kasper, M. Jutzi, and M. Berroth, "High bandwidth Ge p-i-n photodetector integrated on Si," *Appl. Phys. Lett.*, vol. 89, no. 7, p. 071117, Aug. 2006.

[89] T. Song, F. Zhang, X. Lei, Y. Xu, S. Lee, and B. Sun, “Core-shell structured photovoltaic devices based on PbS quantum dots and silicon nanopillar arrays,” *Nanoscale*, 2012.

[90] C. Y. Huang *et al.*, “Efficient light harvesting and carrier transport in PbS quantum dots/silicon nanotips heterojunctions,” *J. Phys. D. Appl. Phys.*, 2011.

[91] H. Yu *et al.*, “Low-Temperature STM Images of Methyl-Terminated Si(111) Surfaces,” *J. Phys. Chem. B*, vol. 109, no. 2, pp. 671–674, Jan. 2005.

[92] H. Yu, L. J. Webb, J. R. Heath, and N. S. Lewis, “Scanning tunneling spectroscopy of methyl- and ethyl-terminated Si(111) surfaces,” *Appl. Phys. Lett.*, vol. 88, no. 25, p. 252111, Jun. 2006.

[93] K. T. Wong and N. S. Lewis, “What a Difference a Bond Makes: The Structural, Chemical, and Physical Properties of Methyl-Terminated Si(111) Surfaces,” *Acc. Chem. Res.*, vol. 47, no. 10, pp. 3037–3044, Oct. 2014.

[94] W. J. Royea, A. Juang, and N. S. Lewis, “Preparation of air-stable, low recombination velocity Si(111) surfaces through alkyl termination,” *Appl. Phys. Lett.*, 2000.

[95] E. J. Nemanick *et al.*, “Chemical and Electrical Passivation of Single-Crystal Silicon(100) Surfaces through a Two-Step Chlorination/Alkylation Process,” *J. Phys. Chem. B*, vol. 110, no. 30, pp. 14770–14778, Aug. 2006.

[96] L. E. Black, B. W. H. van de Loo, B. Macco, J. Melskens, W. J. H. Berghuis, and W. M. M. Kessels, “Explorative studies of novel silicon surface passivation materials: Considerations and lessons learned,” *Sol. Energy Mater. Sol. Cells*, vol. 188, pp. 182–189, Dec. 2018.

[97] G. Dingemans, M. C. M. van de Sanden, and W. M. M. Kessels, “Influence of the

Deposition Temperature on the c-Si Surface Passivation by Al[sub 2]O[sub 3] Films Synthesized by ALD and PECVD," *Electrochem. Solid-State Lett.*, vol. 13, no. 3, p. H76, 2010.

[98] B. Liao, B. Hoex, A. G. Aberle, D. Chi, and C. S. Bhatia, "Excellent c-Si surface passivation by low-temperature atomic layer deposited titanium oxide," *Appl. Phys. Lett.*, vol. 104, no. 25, p. 253903, Jun. 2014.

[99] J. Schmidt *et al.*, "Advances in the Surface Passivation of Silicon Solar Cells," *Energy Procedia*, vol. 15, pp. 30–39, 2012.

[100] B. Chhabra, C. Weiland, R. L. Opila, and C. B. Honsberg, "Surface characterization of quinhydrone-methanol and iodine-methanol passivated silicon substrates using X-ray photoelectron spectroscopy," *Phys. status solidi*, vol. 208, no. 1, pp. 86–90, Jan. 2011.

[101] J. Chen *et al.*, "Silicon surface passivation by polystyrenesulfonate thin films," *Appl. Phys. Lett.*, vol. 110, no. 8, p. 083904, Feb. 2017.

[102] N. S. Lewis, K. E. Plass, X. Liu, and B. S. Brunschwig, "Passivation and secondary functionalization of allyl-terminated Si(111) surfaces," *Chem. Mater.*, vol. 20, no. 6, pp. 2228–2233, Mar. 2008.

[103] L. Meng *et al.*, "Unusual Surface Ligand Doping-Induced p-Type Quantum Dot Solids and Their Application in Solar Cells," *ACS Appl. Mater. Interfaces*, vol. 12, no. 48, pp. 53942–53949, Dec. 2020.

[104] Q. Xu, I. T. Cheong, L. Meng, J. G. C. Veinot, and X. Wang, "Silicon Surface Passivation for Silicon-Colloidal Quantum Dot Heterojunction Photodetectors," *ACS Nano*, vol. 15, no. 11, pp. 18429–18436, Nov. 2021.

[105] A. Gupta, J. P. Bruce, K. McEleney, M. S. Freund, and D. R. Oliver, “Monohydride signature as a key predictor of successful Si(110) surface functionalization,” *RSC Adv.*, vol. 6, no. 91, pp. 88239–88243, 2016.

[106] F. Zhang, D. Liu, Y. Zhang, H. Wei, T. Song, and B. Sun, “Methyl/allyl monolayer on silicon: Efficient surface passivation for silicon-conjugated polymer hybrid solar cell,” *ACS Appl. Mater. Interfaces*, vol. 5, no. 11, pp. 4678–4684, Jun. 2013.

[107] R. Hamilton, C. G. Shuttle, B. O’Regan, T. C. Hammant, J. Nelson, and J. R. Durrant, “Recombination in Annealed and Nonannealed Polythiophene/Fullerene Solar Cells: Transient Photovoltage Studies versus Numerical Modeling,” *J. Phys. Chem. Lett.*, vol. 1, no. 9, pp. 1432–1436, May 2010.

[108] T. Kirchartz and J. Nelson, “Meaning of reaction orders in polymer:fullerene solar cells,” *Phys. Rev. B*, vol. 86, no. 16, p. 165201, Oct. 2012.

[109] D. Credgington, Y. Kim, J. Labram, T. D. Anthopoulos, and J. R. Durrant, “Analysis of Recombination Losses in a Pentacene/C 60 Organic Bilayer Solar Cell,” *J. Phys. Chem. Lett.*, vol. 2, no. 21, pp. 2759–2763, Nov. 2011.

[110] C. G. Shuttle *et al.*, “Experimental determination of the rate law for charge carrier decay in a polythiophene: Fullerene solar cell,” *Appl. Phys. Lett.*, vol. 92, no. 9, p. 093311, Mar. 2008.

[111] B. C. O’Regan, J. R. Durrant, P. M. Sommeling, and N. J. Bakker, “Influence of the TiCl 4 Treatment on Nanocrystalline TiO 2 Films in Dye-Sensitized Solar Cells. 2. Charge Density, Band Edge Shifts, and Quantification of Recombination Losses at Short Circuit,” *J. Phys. Chem. C*, vol. 111, no. 37, pp. 14001–14010, Sep. 2007.

[112] T. M. Clarke, C. Lungenschmied, J. Peet, N. Drolet, and A. J. Mozer, “A comparison of five experimental techniques to measure charge carrier lifetime in polymer/fullerene solar cells,” *Adv. Energy Mater.*, 2015.

[113] C. R. McNeill, I. Hwang, and N. C. Greenham, “Photocurrent transients in all-polymer solar cells: Trapping and detrapping effects,” *J. Appl. Phys.*, vol. 106, no. 2, p. 024507, Jul. 2009.

[114] R. A. Street, “Localized state distribution and its effect on recombination in organic solar cells,” *Phys. Rev. B - Condens. Matter Mater. Phys.*, 2011.

[115] Z. Li, F. Gao, N. C. Greenham, and C. R. McNeill, “Comparison of the Operation of Polymer/Fullerene, Polymer/Polymer, and Polymer/Nanocrystal Solar Cells: A Transient Photocurrent and Photovoltage Study,” *Adv. Funct. Mater.*, vol. 21, no. 8, pp. 1419–1431, Apr. 2011.

[116] F. Zhang, B. Sun, T. Song, X. Zhu, and S. Lee, “Air Stable, Efficient Hybrid Photovoltaic Devices Based on Poly(3-hexylthiophene) and Silicon Nanostructures,” *Chem. Mater.*, vol. 23, no. 8, pp. 2084–2090, Apr. 2011.

[117] M. Y. Bashouti, Y. Paska, S. R. Puniredd, T. Stelzner, S. Christiansen, and H. Haick, “Silicon nanowires terminated with methyl functionalities exhibit stronger Si–C bonds than equivalent 2D surfaces,” *Phys. Chem. Chem. Phys.*, vol. 11, no. 20, p. 3845, 2009.

[118] M. Yuan *et al.*, “Phase-Transfer Exchange Lead Chalcogenide Colloidal Quantum Dots: Ink Preparation, Film Assembly, and Solar Cell Construction,” *Small*, vol. 18, no. 2, p. 2102340, Jan. 2022.

[119] M. Liu *et al.*, “Hybrid organic–inorganic inks flatten the energy landscape in colloidal

quantum dot solids," *Nat. Mater.*, vol. 16, no. 2, pp. 258–263, Feb. 2017.

[120] M.-J. Choi *et al.*, "Cascade surface modification of colloidal quantum dot inks enables efficient bulk homojunction photovoltaics," *Nat. Commun.*, vol. 11, no. 1, p. 103, Dec. 2020.

[121] Y. Wang *et al.*, "Room-temperature direct synthesis of semi-conductive PbS nanocrystal inks for optoelectronic applications," *Nat. Commun.*, vol. 10, no. 1, p. 5136, Dec. 2019.

[122] M. Biondi *et al.*, "Facet-Oriented Coupling Enables Fast and Sensitive Colloidal Quantum Dot Photodetectors," *Adv. Mater.*, vol. 33, no. 33, p. 2101056, Aug. 2021.

[123] Q. Xu, I. T. Cheong, H. Song, V. Van, J. G. C. Veinot, and X. Wang, "Heterogeneous Integration of Colloidal Quantum Dot Inks on Silicon Enables Highly Efficient and Stable Infrared Photodetectors," *ACS Photonics*, vol. 9, no. 8, pp. 2792–2801, Aug. 2022.

[124] R. Wang *et al.*, "Highly Efficient Inverted Structural Quantum Dot Solar Cells," *Adv. Mater.*, vol. 30, no. 7, p. 1704882, Feb. 2018.

[125] O. J. Sandberg, K. Tvingstedt, P. Meredith, and A. Armin, "Theoretical Perspective on Transient Photovoltage and Charge Extraction Techniques," *J. Phys. Chem. C*, vol. 123, no. 23, pp. 14261–14271, Jun. 2019.

[126] M. Azzouzi *et al.*, "Overcoming the Limitations of Transient Photovoltage Measurements for Studying Recombination in Organic Solar Cells," *Sol. RRL*, vol. 4, no. 5, p. 1900581, May 2020.

[127] J. Choi *et al.*, "Activated Electron-Transport Layers for Infrared Quantum Dot Optoelectronics," *Adv. Mater.*, vol. 30, no. 29, p. 1801720, Jul. 2018.

[128] W. Zhou *et al.*, "Silicon: quantum dot photovoltage triodes," *Nat. Commun.*, vol. 12, no.

1, p. 6696, Dec. 2021.

[129] Y. Chen *et al.*, “Unipolar barrier photodetectors based on van der Waals heterostructures,” *Nat. Electron.*, vol. 4, no. 5, pp. 357–363, May 2021.

[130] J. Bullock *et al.*, “Polarization-resolved black phosphorus/molybdenum disulfide mid-wave infrared photodiodes with high detectivity at room temperature,” *Nat. Photonics*, vol. 12, no. 10, pp. 601–607, Oct. 2018.

[131] Z. Li and C. R. McNeill, “Transient photocurrent measurements of PCDTBT:PC 70 BM and PCPDTBT:PC 70 BM Solar Cells: Evidence for charge trapping in efficient polymer/fullerene blends,” *J. Appl. Phys.*, vol. 109, no. 7, p. 074513, Apr. 2011.

[132] R. C. I. MacKenzie, C. G. Shuttle, M. L. Chabinyc, and J. Nelson, “Extracting Microscopic Device Parameters from Transient Photocurrent Measurements of P3HT:PCBM Solar Cells,” *Adv. Energy Mater.*, vol. 2, no. 6, pp. 662–669, Jun. 2012.

[133] P. R. F. Barnes, A. Y. Anderson, J. R. Durrant, and B. C. O’Regan, “Simulation and measurement of complete dye sensitised solar cells: including the influence of trapping, electrolyte, oxidised dyes and light intensity on steady state and transient device behaviour,” *Phys. Chem. Chem. Phys.*, vol. 13, no. 13, p. 5798, 2011.

[134] X. Li *et al.*, “High Detectivity Graphene-Silicon Heterojunction Photodetector,” *Small*, vol. 12, no. 5, pp. 595–601, Feb. 2016.

[135] X. An, F. Liu, Y. J. Jung, and S. Kar, “Tunable Graphene–Silicon Heterojunctions for Ultrasensitive Photodetection,” *Nano Lett.*, vol. 13, no. 3, pp. 909–916, Mar. 2013.

[136] J. Yin *et al.*, “Engineered tunneling layer with enhanced impact ionization for detection improvement in graphene/silicon heterojunction photodetectors,” *Light Sci. Appl.*, vol. 10,

no. 1, p. 113, Dec. 2021.

[137] M. R. Esmaeili-Rad and S. Salahuddin, “High performance molybdenum disulfide amorphous silicon heterojunction photodetector,” *Sci. Rep.*, vol. 3, no. 1, p. 2345, Dec. 2013.

[138] A. Noroozi, A. Mosaddegh, and Y. Abdi, “High-sensitivity and broadband PEDOT:PSS–silicon heterojunction photodetector,” *Mater. Sci. Eng. B*, vol. 271, p. 115260, Sep. 2021.

[139] Z. Liang, P. Zeng, P. Liu, C. Zhao, W. Xie, and W. Mai, “Interface Engineering To Boost Photoresponse Performance of Self-Powered, Broad-Bandwidth PEDOT:PSS/Si Heterojunction Photodetector,” *ACS Appl. Mater. Interfaces*, vol. 8, no. 29, pp. 19158–19167, Jul. 2016.

[140] V. Dhyani and S. Das, “High-Speed Scalable Silicon-MoS2 P-N Heterojunction Photodetectors,” *Sci. Rep.*, vol. 7, no. 1, p. 44243, May 2017.

[141] J. Mao *et al.*, “Ultrafast, Broadband Photodetector Based on MoSe 2 /Silicon Heterojunction with Vertically Standing Layered Structure Using Graphene as Transparent Electrode,” *Adv. Sci.*, vol. 3, no. 11, p. 1600018, Nov. 2016.

[142] H. Ahmad, H. Rashid, M. F. Ismail, and K. Thambiratnam, “Fabrication and characterization of tungsten disulphide/silicon heterojunction photodetector for near infrared illumination,” *Optik (Stuttg).*, vol. 185, pp. 819–826, May 2019.

[143] W. Gao *et al.*, “Self-Powered SnS 1– x Se x Alloy/Silicon Heterojunction Photodetectors with High Sensitivity in a Wide Spectral Range,” *ACS Appl. Mater. Interfaces*, vol. 11, no. 43, pp. 40222–40231, Oct. 2019.

[144] L. Chen, W. Tian, C. Sun, F. Cao, and L. Li, “Structural Engineering of Si/TiO 2 /P3HT

Heterojunction Photodetectors for a Tunable Response Range," *ACS Appl. Mater. Interfaces*, vol. 11, no. 3, pp. 3241–3250, Jan. 2019.

[145] W. Xie *et al.*, "On-Chip Integrated Quantum-Dot-Silicon-Nitride Microdisk Lasers," *Adv. Mater.*, vol. 29, no. 16, p. 1604866, Apr. 2017.

[146] Y.-S. Park, J. Roh, B. T. Diroll, R. D. Schaller, and V. I. Klimov, "Colloidal quantum dot lasers," *Nat. Rev. Mater.*, vol. 6, no. 5, pp. 382–401, May 2021.